Susceptibility, Diffusion and Relaxation Contrast in NMR Microscopy at High Resolution

A thesis presented in partial fulfilment of the requirements

for the degree of Master of Science in Physics

at Massey University

Lucy Catherine Forde

1994

To my mother, Margot,
who set me on the road to science

Abstract

An integrated approach to the functional NMR imaging of plant tissue at moderately-high transverse resolution (23 μm) was undertaken. Attention was paid to all the possible commonly-known influences, such as sources of nuclear spin relaxation or of artefacts, relevant to the final image intensity of the different tissues.

While it was not clear at the outset which influences might prove to be significant, two phenomena in particular, susceptibility inhomogeneity and correlated diffusion effects, were selected for detailed investigation using simple model systems constructed from small glass tubes and rods combined with aqueous solutions, before continuing on to more complex plant samples. Simulated images compared well with the experimental results in these studies.

Preliminary images of a stem of an intact *Stachys sylvatica* L. plant showed that the apparent T_2 relaxation time is much less (an order of magnitude) than the T_1 relaxation time in all tissues. A range of diagnostic pulse sequences was then carried out on this and similar stems in order to reveal the signatures for different models of T_2 relaxation which might explain this fact (assuming that the water protons imaged fall within the extreme-narrowed region of Bloembergen, Purcell and Pound theory). It was found that measures were necessary to avoid the complicating factor of attenuation due to diffusion in the applied read gradient, specifically the use of Carr-Purcell-Meiboom-Gill (CPMG) refocusing pulses. Susceptibility inhomogeneity seemed important in sensitive gradient echo images, but further experiments at different B_0 strengths revealed that it (and chemical shift exchange) does not contribute significantly to the spin echo image contrast. The Brownstein-Tarr model of relaxation at boundaries and surfaces (without local field offsets) was also considered as a possibility, but was ruled out for at least some of the tissues (those which display a CPMG pulse-spacing dependence). Another alternative explanation is short-range dipole interactions between water protons and protons of more slowly-moving molecules, which should be abundant in the particular cells which escape the other hypotheses, but it is difficult to confirm this within the scope of the pulse sequences used here. More progress might be possible with proper multicomponent T_2 analysis and improved knowledge of subcellular structure of our particular tissues.

Acknowledgements

Firstly, I would like to thank my supervisor, Professor Paul Callaghan, for extensive theoretical and practical support during this project, and for a belief in the value of these experiments.

I would also like to thank the following people for their involvement in this work.

Dr Yang Xia, a fellow student in the early stages of this study, for instruction on the advantages, pitfalls and handling of the plant *Stachys sylvatica* as a specimen for NMR imaging.

Karen Tyrrell, for experimental assistance when I was far from home.

The Department of Plant Biology, for providing glasshouse space for the cultivation of plant specimens, and in particular Dr Izabela Konczak-Islam, for painstaking effort taken over the microtoming of my plant stems.

Dr Al Rowland and Dr George Ionas, for their kind services contributing to the photomicroscopy in this thesis, and their respective departments, the Department of Plant Biology and the Department of Microbiology and Genetics, for supplying the necessary facilities.

Walter Köckenberger (University of Bayreuth), Dr Iain Taylor (University of British Columbia) and Dr Jim Pope (University of New South Wales), for expert advice on matters botanical and otherwise while they were visitors to this laboratory.

The Ministry of Research, Science and Technology, for financial assistance in the form of a generous scholarship in 1991 and 1992.

The New Zealand Lotteries Board and the Foundation for Research, Science and Technology, for grants supporting the Nuclear Magnetic Resonance laboratory at Massey University.

Finally, I sincerely thank my friends in the NMR research group and in the Department of Physics and Biophysics as a whole, for valuable moral support throughout.

Contents

Chapter 1
Introduction

Nuclear Magnetic Resonance (NMR) imaging has widely been recognised as an invaluable tool for the non-invasive exploration of materials and organisms at the macroscopic and microscopic level *(1,2)*. The most commonly encountered applications are in medicine *(3)*, where patients are routinely scanned for soft-tissue abnormalities signalling tumours and a variety of other conditions. The size of instrument appropriate to accommodate human bodies or limbs precludes an in-plane resolution of much less than a millimetre. However the technique may be extended to a resolution on the order of a few microns with a corresponding reduction in the size of the sample to be inspected.

One must not make the mistake of equating NMR and optical images, because they do not depict the same characteristics and indeed rarely resemble each other closely. Instead of relying on reflection of incident light from the required object, NMR measures the radio frequency responses of target nuclei, receiving an equally strong contribution from nuclei in the interior of the object as from those at the surface. Thus we may examine the interior hidden from our eyes without significant disturbance to the specimen. Although somewhat unfamiliar in interpretation to a brain accustomed to processing optical data, the NMR image is of course no less valid a representation. Ideally the picture element (pixel) intensities should imitate the concentration of target nuclei in the specimen volume elements (voxels), but many other parameters may modify the intensity observed, and these may be used to indicate various properties of interest. It is this range of parameters and nuclei-specific concentration which material scientists and biologists utilise, especially where the lack of physical penetration and consequent detrimental effects is crucial, as in medicine.

There is a wealth of literature devoted to the use of NMR imaging in medical applications, which are wide-ranging, and may be non-invasive or instead undertaken in the laboratory. For example, in the former case the technique may be utilised to directly observe tumours, transplants and spinal cord injury or to follow metabolite levels in the brain *(4,5)*, to discriminate between skin, muscle, marrow and cartilage tissue in a finger by separate examination of fat and water components *(6)*, and to possibly enable early detection of osteoarthritis in the knee joint through changes in calcification and the cartilage matrix. In the latter case it is possible to study cancer processes using tumour spheroids or by inspection of inflammation and necrosis using the histology of excised tumours, to monitor the osmotic pressure in blood *(7,8)* and so on. Parallel research may be carried out on animal subjects, often (but not always) with a view to the advance of

medical aims. Examples include studies of muscle characteristics in barnacles and rats *(9-12)*, brain anatomy in rats and dogs *(13,14)*, metabolism in 16 different rat tissues *(15)* and, more remarkably, *in vivo* imaging of a healthy beating rat heart viewed at chosen points in the beat cycle *(6)*. In this way defects like holes in the heart may soon be diagnosed safely in humans.

NMR imaging is actually ideal for a great many biological applications beyond medicine, due to the ease of detection of the hydrogen nuclei (protons) in water, and the roughly 75% water content of most biological tissue. It is capable of rapid histology without artefacts from fixation, dehydration, embedding, sectioning or staining which can plague the ability of conventional histology to reflect the true state of tissues *in vivo*. An added advantage is the capacity for three-dimensional imaging to aid visualisation of whole structures, their positions with respect to others and any links between them. Yet more dimensions may be added if measurement of the concentration of a specified chemical component is desired. These variations in technique together can be put to good use by industries such as horticulture, food and forestry.

Non-destructive quality evaluation of fruit and vegetables is possible, for example observing bruising in apples, worm damage in asian pear, seeds in grapes, dry regions in oranges and hollow heart in potatoes *(16-18)*. The spread of botrytis (grey mould fungus) mycelium across a single raspberry drupelet and a whole strawberry fruit has been monitored in the hope of breeding resistant cultivars *(19)*. Sugar content and other ripening processes have been followed in grape, raspberry and barley seeds *(20-22)* enabling optimum storage conditions to be determined *(18,23)*. Other postharvest processes are also studied, from the senescence of mushrooms to the moisture transfer and shrinkage in an ear of corn during dessication *(24)*. The effects of chilling and freezing (e.g. cell wall rupture) are seen in vegetables such as zucchini *(17,25,26)*, and water distribution during the steeping of corn kernels in water is elucidated *(27)*. Simple morphological studies can be useful *(28-30)*, especially where vascular architecture is complex as for the spiral arrangement of drupelets and vascular traces in a raspberry receptacle, or where there are changes with development and maturation *(31)*. It is possible to follow the differentiation of separate tissues which arise from different ontological origins.

Other fully-processed foods are complex and interesting systems, often containing dispersions of lipid and water, or liquid and air. Knowledge of the structure and collapse of food foams, as found in whipped cream or egg white or in beer, helps in the design of required foam stability in each food product *(32)*. Air spaces in cheeses such as gruyere

are easily seen, as well as components in composite foods like chocolate bars, without even removing the wrappers *(17)*. Cocoa butter, the main matrix of chocolate, occurs in more than one crystalline form, and these may be studied if the chocolate is melted and cooled at different rates to generate the various polymorphic states *(33)*.

It is evident that NMR imaging is here to stay in the commercial world, pervading a fairly wide cross-section of industries, but it is also employed in more basic research as a tool for greater understanding of non-commercial species. The contrast afforded by NMR, apart from chemical and nuclear specificity, mainly arises from the NMR relaxation rates present in the sample which modulate the intensity observed. These are sensitive to molecular dynamics such as diffusion and binding state *(25,26,34-39)* and therefore tend to reflect morphology more effectively than the molecular density alone. In particular relaxation times T_1 and T_2 are often discussed in this context, and will be explained in more detail later, but for the moment it is enough to know that T_2 measurement is the method most commonly used to probe the chemical dynamics of a sample or to distinguish between variations in anatomy. Relaxation times could be likened to inherent proton 'stains'.

Thus the function of the assorted organs of plants can be investigated *in vivo*. The stems of plants have a range of very specialised cell types, combining to form the tissues which perform the vital processes of support and of transport of water and nutrients. An improvement of these processes can always be used to improve the yield of commercial crops. The stems of geraniums, runner beans, celery, cucumbers, horsetails, ferns and mosses have undergone examination *(30,34,35,40-44)*, sampling a variety of morphologies. Other studies of plant parts have looked at disease or growth of roots *(45,46)*, leaves *(47)*, seed pods *(5)*, germinating seeds *(41,48)*, bark *(49)* and flower buds *(50,51)*. The buds were from fruiting species such as apple and blackcurrant, and were subjected to chilling to simulate the outcome of an unexpected frost. Root function was probed under varied conditions of water stress and recovery, or different soil types, using the uptake of water doped with a paramagnetic ion such as Mn^{2+} which decreases T_1 *(41,52-54)*. Even such large specimens as trees do not escape attention, and the problems of incompatible graft unions in apple *(55)* and blight in citrus *(46)* have been considered as well as the normal growth rings, heartwood and knots found in aspen and spruce wood *(56)*. At the other extreme of plant life the development of the fascinating alga *Acetabularia mediterranea* is investigated through T_1 changes which are thought to relate to the changing concentrations of microtubules inside *(57)*. The entire alga consists of a single giant wall-less cell which is several millimetres in size and an elaborate fluted-

umbrella shape. Without the support of walls the organism must necessarily regulate shape and expansion via intracellular microtubules.

Clearly the understanding of plant physiology may be enhanced with these methods, and the facility of velocity and diffusion measurement is a particularly valuable aspect of NMR for this. Plant water relations have always proven tricky to analyse with confidence, and in the past studies have relied on the movement of a tracer molecule introduced often by invasive means. Now transpiration can be monitored directly in combination with changes in environmental parameters such as humidity and sunlight, for example during the course of a day, and this has been carried out for the case of greenhouse cucumbers *(30)*. Taken a step further velocity measurement may be combined with imaging giving a map showing spatially-resolved velocity, and this has been done using plants from different parts of the evolutionary tree, a moss, horsetail and a flowering plant, in order to compare the vascular structures which conduct water *(44)*. Transpiration may be studied using less direct methods as well, by examining water content and relaxation times in roots and stems for slow and active transpiration conditions *(34,58)*. Of course velocity mapping touches other fields too, promising to have a fruitful future in angiography (visualisation of the circulatory system) for heart disease and stroke problems in humans *(4)*. Diffusion coefficient mapping also has a part to play here, as diffusion is seen to drop in areas of the brain damaged by occlusion of an artery, and the mapping allows rapid estimation of the nature and seriousness of damage in stroke victims. Returning to plants, diffusion mapping in wheat grains helps distinguish between the major structural features, and the addition of velocity detection gives insight into the circulation inside the grain which loads nutrients from the plant's photosynthetic sinks into the endosperm *(59,60)*.

Closer analysis of relaxation times sometimes reveals further information in the form of multiple relaxation components *(11,54,61)*, arising from the separate populations of water within a heterogeneous sample which experience different environments. Examples of such populations might be intra- and extracellular water, that inside organelles like chloroplasts and mitochondria or water associated closely with phospholipid membranes, proteins, polysaccharides or other macromolecules. In this way the relative population sizes present in these sites may be estimated and observed during experimental treatments, although it is not always possible to be certain of the correspondence between a relaxation fraction and a cellular location *(10,12,48,62)*. Each plant species and part appears to exhibit its own characteristic 'fingerprint' of relaxation components. In ivy bark two components were found, relating to extracellular water in the cell wall and to the bulk inside the cell *(49)*. Plant tissue, unlike animal tissue,

typically contains air between the cells with just a little water hydrating the wall biopolymers outside the cell. In apple fruit there were three components, relating to the extracellular, cytoplasmic and vacuolar water *(63)*. Some plant cell types contain only a small amount of cytoplasm and instead a large and very dilute vacuole occupies most of the volume, separated from the cytoplasm by a membrane called the tonoplast. It is easy to see that the dynamics of the vacuolar contents will most closely resemble those of free water, while the dynamics of the hydration water will be much more restricted. In imaging, some hydration or 'bound' water will be so immobile as to be rendered effectively invisible, possessing a T_2 value below the minimum needed to enable detection during finite imaging times.

Unless there are impermeable barriers, molecules are exchanged between the populations to a certain extent, and this leads to a partial blending of the relaxation components *(4,61,64-72)*. In apple species this exchange was observed and from it the permeability coefficients of both the cell membrane and tonoplast were calculated. Studies on the exchange between cell interior (lumen) water and the cell surface layer water in western red cedar wood show that lumen T_2 scales with surface-to-volume ratio and hence with cell diameter *(73,74)*. This method was able to distinguish between earlywood tracheids, formed first in the annual growth season and seen just outside the growth rings, and latewood tracheids which are generated at the cooler end of the season and have on average only a third of the lumen diameter found in earlywood. Other investigations of compartmentation at the tissue, cellular or intracellular level include size determination of erythrocytes in blood and separation of the cornea into its cell and collagen stroma constituents *(7,8,75-77)*.

Thus through sophisticated relaxation analysis we are able to partly explore the interior of cells which usually cannot be seen directly in NMR imaging. The resolution of NMR imaging is limited by the need for an adequate signal-to-noise ratio (related to the number of nuclei in each voxel) and is inferior to light microscopy. Only the upper end of the range of biological cell sizes may be identified individually in an image *(40,41,78,79)*. To make matters worse, diffusion effects (namely signal loss) become very unfavourable when the pixel size is small enough so that molecules may diffuse the order of the pixel during imaging times, and this can hinder efforts to image close to the fundamental resolution. In such adverse conditions only molecules with sufficiently slowed or restricted diffusion will be seen. Hence optimal resolution is at times elusive due to its special complications.

One way to accentuate the borders between cells or tissues is to use the gradient echo form of imaging as opposed to the spin echo *(19,22,27)*. These forms will be outlined in Chapter 2 but it is sufficient here to say that the gradient echo is very sensitive to stray magnetic fields induced in a sample by an external applied magnetic field, whereas the spin echo is more successful at refocusing the same effects, provided the extra fields are stationary. The origin of the induced fields is the range of magnetic susceptibilities found in a heterogeneous sample. The magnetic susceptibility of a material determines the size of any induced field, and the boundary between two differing susceptibilities will generate a whole distribution of fields in the vicinity of the discontinuity. Biological tissue would be expected to have many such boundaries, but the extent of the effect on imaging varies. These susceptibility effects might be considered a nuisance in some instances and a useful tool in others. Certainly the gradient echo sequence is used when maximum contrast between tissues is desirable.

Recently a very special application of susceptibility was discovered in the field of human psychology and neurology. Neural activity results in a mild local enhancement of oxygen consumption, which is overcompensated by a larger increase in regional blood volume, and after a few seconds a transient hyperoxemia arises. Thus the amount of paramagnetic deoxyhaemoglobin increases and this tissue oxygenation is detectable by an accompanying shift in susceptibility. If rapid acquisition techniques are used then brain activation may be monitored during the application of various stimuli involving the visual *(80-84)*, motorsensory *(85)*, language processing and other systems. A comparison of consecutive gradient and spin echo images *(86-88)* yields what appears to be a map of neural activity in the brain, directly visualising the cerebral compartments responsible for the thought or movement being studied. This capability opens the way for a whole host of psychological investigations (termed functional brain imaging) which are considered safe for the volunteers concerned.

Although the spin echo sequence of imaging is not influenced by strictly static field variation on top of the normal imaging gradients, the migration of molecules from one position to another in these variations will lessen its refocusing ability and hence additional relaxation will result. In this way susceptibility effects may also shorten T_2 itself although this depends on the rate of diffusion as well as the magnitude of the variations *(8,9,14,39,54,78,89,90)*. With such a diversity of relaxation mechanisms, as mentioned earlier, existing on top of the susceptibility effects, it can be an intricate task indeed to unravel the mechanisms which are at work in any new sample *(4,15,26,28,34,61,63,75,91)*.

The versatility of NMR imaging and its consequent role in so many branches of science makes continual improvement of understanding in this area worthwhile. The purpose of this thesis is to take an integrated approach to the imaging of plant tissue at fairly high resolution, looking closely at all the possible relevant influences (i.e. sources of relaxation and artefacts) which vie for dominance in determining the final image intensity, while keeping an open mind as to which of them will prove significant. The exhaustive NMR study of biology outlined above demonstrates more than anything the multiplicity of phenomena which occur for different biological specimens, and it is wise not to disregard any mechanisms available in the interpretation of the resulting image contrast. At the same time we hope to further the understanding of susceptibility effects in particular, as these are often alluded to but seldom pursued thoroughly.

A system providing a variety of challenges was necessary for this work, and plant stems seemed suitable in that they contain a range of very different cell types with wide-ranging functions. There is also the facility to demonstrate the measurement of very delicate biological flow *in situ*, which will actually pinpoint the active transport locations rather than assuming that all the cells differentiated for this purpose are so. The use of simple model systems will be utilised to increase awareness of two of the phenomena involved, susceptibility and diffusion and their correlation, before venturing on to truly complex examples. This route may enable us to build upon recent research by others into plant tissue contrast in NMR microscopy.

Chapter 2
The Theory of NMR Imaging

The theory of NMR *(92,93)* and its consequent imaging is now well-accepted and well understood, and has been covered extensively in a recent text by Callaghan *(94)* as well as nicely summarised previously in the theses of former students from the Massey University NMR laboratory *(95-97)*. Here a brief version of this theory is presented, largely following the sequence set by these texts but without straying too much into areas surplus to the interpretation of later results.

2.1 Nuclear Magnetism

Atomic nuclei possess a magnetic dipole moment $\boldsymbol{\mu}$ which is proportional to their inherent angular momentum $\mathbf{I}$, and the constant of proportionality γ is known appropriately as the gyromagnetic ratio. The angular momentum is measured in units of $\hbar$ (Planck's constant/2π), and for a single nucleus the value observed will belong to a discrete set of possibilities according to the nature of quantum mechanics. Thus it is derived from the angular momentum quantum number I as

$$|\mathbf{I}| = \sqrt{I(I+1)}\hbar. \tag{2.1}$$

I, also known as the spin quantum number or 'spin', is an integer or half-integer value which describes the nucleus in its stable ground state. We will be concentrating on the hydrogen nucleus which is spin-$\frac{1}{2}$.

The magnetic dipole $\boldsymbol{\mu}$ allows the nucleus to interact with a magnetic field $\mathbf{B}_0$, resulting in an interaction energy of $-\boldsymbol{\mu}\cdot\mathbf{B}_0$. A quantum mechanical description is given by the Hamiltonian (or energy) operator, which for the case of B_0 along the z-axis is

$$H = -\gamma\hbar B_0 I_z \tag{2.2}$$

where I_z is the operator for angular momentum component along the z-axis. This magnetic interaction is known as a 'Zeeman' interaction. The eigenvalues of I_z vary in integer steps between $-I$ and I, giving $\pm\frac{1}{2}\hbar$ for the spin-$\frac{1}{2}$ nucleus, and the separation ΔE between these two energy levels or eigenstates produced by the Zeeman Hamiltonian is $\gamma\hbar B_0$.

If H is constant with time then the evolution of the spin state, derived from the Schrödinger Equation, is given by the evolution operator

$$U(t) = \exp(-iHt/\hbar), \tag{2.3}$$

which simply represents a rotation. For our Hamiltonian $U(t) = \exp(i\gamma B_0 I_z t)$, and this corresponds to a clockwise rotation of the state about the z-axis by angle $\gamma B_0 t$. More generally, in the presence of B_0 all states precess about z at an angular frequency known as the Larmor frequency

$$\omega_0 = \gamma B_0. \tag{2.4}$$

2.2 Macroscopic Magnetisation and the Semi-Classical Description

The description so far of the nuclear interaction with a magnetic field has concerned a single nucleus in isolation, yet in practice experiments are never carried out on single nuclei. Instead we must deal with macroscopic samples which are vast collections or ensembles of spins, and the different nuclei may occupy different states $|\Psi\rangle$. Therefore the observable quantities will actually be ensemble averages. An arbitrary spin quantum state $|\Psi\rangle$ of a nucleus is a linear combination of the finite set of basis states $|m\rangle$, each multiplied by a complex amplitude a_m incorporating phase and magnitude information. For the single nucleus in such an admixed state the interpretation would be that a measurement of I_z has the probability $|a_m|^2$ of returning the result m. But what is the result of a measurement on a large number of nuclei? The outcome is a mean of the individual eigenvalue results weighted by the normalised probabilities, again $|a_m|^2$. In the proton case we have the two eigenstates of I_z labelled by their eigenvalues, $|\frac{1}{2}\rangle$ and $|-\frac{1}{2}\rangle$, and the expression for an arbitrary state becomes $|\Psi\rangle = a_{\frac{1}{2}}|\frac{1}{2}\rangle + a_{-\frac{1}{2}}|-\frac{1}{2}\rangle$. The so-called ensemble-averaged 'expectation' value $\overline{\langle\Psi|I_z|\Psi\rangle}$ is given by

$$\overline{\langle\Psi|I_z|\Psi\rangle} = 1/2(\ \overline{|a_{\frac{1}{2}}|^2}\ -\ \overline{|a_{-\frac{1}{2}}|^2}\ ), \tag{2.5}$$

and this equation shows that the expectation value is determined by the difference in population between the upper and lower energy levels. This difference is known as the 'polarisation' of the ensemble, and in thermal equilibrium it can be calculated from the Boltzmann Distribution

$$\overline{|a_m|^2} = \frac{\exp(-E(m)/k_B T)}{\sum_m \exp(-E(m)/k_B T)} \tag{2.6}$$

where $E(m)$ is the energy of the eigenstate $|m\rangle$, here $-\hbar\gamma B_0/2$ and $\hbar\gamma B_0/2$ for $m=\frac{1}{2}$ and $m=-\frac{1}{2}$ respectively. Thus

$$\overline{|a_{\pm\frac{1}{2}}|^2} = \frac{\exp(\pm\hbar\gamma B_0/2k_B T)}{\exp(-\hbar\gamma B_0/2k_B T) + \exp(\hbar\gamma B_0/2k_B T)} \tag{2.7}$$

and since the energy difference $\hbar\gamma B_0$ in a laboratory magnet is typically over five orders of magnitude smaller than the Boltzmann energy $k_B T$ at room temperature

$$\overline{|a_{\pm\frac{1}{2}}|^2} \approx \frac{1}{2}(1 \pm \hbar\gamma B_0/2k_B T). \tag{2.8}$$

The semi-classical interpretation of the slightly higher population in the lower energy state $|\frac{1}{2}\rangle$ is that a net angular momentum z-component (or longitudinal magnetisation M_z) exists in the same axis and sense as the external field B_0.

Having established that a magnetic field will give rise to a small magnetisation along its axis, what will we find for the case of the x-component of angular momentum I_x? Once again the ensemble-averaged expectation value is

$$\overline{\langle\Psi|I_x|\Psi\rangle} = \frac{1}{2}(\overline{a^*_{\frac{1}{2}}a_{-\frac{1}{2}}} + \overline{a_{\frac{1}{2}}a^*_{-\frac{1}{2}}}), \tag{2.9}$$

which is markedly different from z-component case and reflects the degree of phase coherence between the two states. Semi-classically, we would expect no phase coherence in thermal equilibrium, so that both terms will be zero and there will be no transverse magnetisation under the influence of the longitudinally-oriented B_0 alone. We shall see that it is necessary to stimulate phase coherence and thus transverse magnetisation in order to provide the signal for an NMR experiment.

When dealing with ensemble behaviour another operator, the 'density' operator ρ, is often utilised to describe a range of observables of interest. It is defined by

$$\rho = p_\Psi |\Psi\rangle\langle\Psi| \tag{2.10}$$

where the ensemble is seen to consist of a number of 'subensembles' or sets of nuclei in identical states $|\Psi\rangle$, each with probability p_Ψ. The advantage of the density operator lies

in its facility for determining expectation values for any operator A through the simple expression

$$\overline{\langle \Psi | A | \Psi \rangle} = \mathrm{Tr}(A\rho) \tag{2.11}$$

where $A\rho$ will be a matrix and $\mathrm{Tr}(A\rho)$ is the sum of its diagonal components. Our spin-$\frac{1}{2}$ proton will have a 2x2 density matrix due to its two eigenstates. Thus

$$\rho = \begin{bmatrix} \frac{1}{2} + \overline{\langle I_z \rangle} & \overline{\langle I_x - iI_y \rangle} \\ \overline{\langle I_x + iI_y \rangle} & \frac{1}{2} - \overline{\langle I_z \rangle} \end{bmatrix}, \tag{2.12}$$

with $\overline{\langle I_z \rangle}$ as the shorthand form of the expectation value $\overline{\langle \Psi | I_z | \Psi \rangle}$. Only three numbers are necessary to define all elements of ρ for any state of the ensemble, here $\overline{\langle I_x \rangle}$, $\overline{\langle I_y \rangle}$ and $\overline{\langle I_z \rangle}$ or, macroscopically, the components of the magnetisation vector

$$\mathrm{M} = N\gamma\hbar \left[\overline{\langle I_y \rangle}\, \mathbf{i} + \overline{\langle I_y \rangle}\, \mathbf{j} + \overline{\langle I_z \rangle}\, \mathbf{k} \right]. \tag{2.13}$$

N is the number density or the number of spins per unit volume. In this way **M** effectively contains all necessary information regarding the state of the ensemble of spin-$\frac{1}{2}$ nuclei, providing the nuclei behave independently. Since any Hamiltonian induces precessional motion in such an ensemble, we can always describe the motion of the ensemble as a precession of the spin magnetisation vector **M**. This is further confirmed by equating the torque experienced by the magnetic moments due to the magnetic field **B** with the rate of change of angular momentum

$$\frac{d\mathbf{M}}{dt} = \gamma \mathbf{M} \times \mathbf{B}, \tag{2.14}$$

as the solution to this is precession of **M** about **B** at $\omega = \gamma B$ as expected.

2.3 Resonant Excitation

The nuclear magnetic resonance phenomenon requires 'excitation' of the spins by a 'resonant' oscillating magnetic field transverse to the main field $\mathbf{B}_0$. Here the Hamiltonian gains a time-dependent term in the laboratory frame.

$$H = -\gamma B_0 I_z - 2\gamma B_1 \cos \omega t \, I_x, \tag{2.15}$$

where B_1 and ω are the amplitude and angular frequency of the new field (noting that the factor of $\hbar$ in Hamiltonians, although assumed, is often not explicitly written). To explain further, we must represent the small linearly-polarised oscillatory field B_1 by the superposition of two circularly-polarised oscillatory fields which rotate in opposite senses in the transverse plane. If our frame of reference is allowed to rotate so that the component rotating in the same sense as the precessing spins is stationary, the apparent rate of spin precession will appear to be reduced by ω, and this is interpreted as a reduction in the longitudinal field by ω/γ. In fact for $\omega = \omega_0$ ('at resonance') the longitudinal field vanishes altogether, and in this way the relatively small oscillating field is able to have a strong interaction with the spins. The new Hamiltonian in the rotating frame

$$H_{\text{rot}} = -\gamma(B_0 - \omega/\gamma)I_z - \gamma B_1 I_x \tag{2.16}$$

is now time independent and so it is possible to use the simple evolution operator U, which indicates precessional motion. Conversely, in a frame of reference which rotates with the other oscillatory field component the effective longitudinal field will increase over and above B_0 (to $2B_0$ for $\omega = \omega_0$), and B_1 will have a negligible effect because $B_1 << B_0$ typically. Hence we can ignore this second component and continue to use the first rotating frame of reference, where the only effective field is along the rotating x-axis (for $\omega = \omega_0$). The spins will therefore precess about the x-axis instead and in this way transverse magnetisation is achieved. Quantum mechanically, precession about this axis may be thought of as an ongoing interconversion of the spins between the $|\frac{1}{2}\rangle$ and $|-\frac{1}{2}\rangle$ states at a rate γB_1, hence the term 'excitation'. If $\omega \neq \omega_0$ then there will be both longitudinal and transverse field components present in the rotating frame and the spins will precess around $\mathbf{B}_{\text{eff}}$, the vector sum of these.

Returning to our semi-classical description, the addition of the resonant circularly-polarised oscillatory field, $\mathbf{B}_1(t) = B_1 \cos \omega_0 t\, \mathbf{i} - B_1 \sin \omega_0 t\, \mathbf{j}$, into eqn (2.14) gives

$$\begin{aligned}
\frac{dM_x}{dt} &= \gamma(M_y B_0 + M_z B_1 \sin \omega_0 t) \\
\frac{dM_y}{dt} &= \gamma(-M_x B_0 + M_z B_1 \cos \omega_0 t) \\
\frac{dM_z}{dt} &= \gamma(-M_x B_1 \sin \omega_0 t - M_y B_1 \cos \omega_0 t),
\end{aligned} \tag{2.17}$$

and with our initial condition $\mathbf{M}(t) = M_0\mathbf{k}$ (longitudinal magnetisation only) the solution is

$$M_x = M_0 \sin \omega_1 t \ \sin \omega_0 t$$

$$M_y = M_0 \sin \omega_1 t \cos \omega_0 t$$

$$M_z = M_0 \cos \omega_1 t \qquad (2.18)$$

where $\omega_1 = \gamma B_1$. These equations show clearly the simultaneous precession of the magnetisation vector about B_0 (at ω_0) and about B_1 (at ω_1) in the laboratory frame, or simply the latter in our convenient rotating frame of reference.

Large laboratory magnets are typically on the order of 1 to 10 T in magnitude, producing precession frequencies (f_0) of a few hundred megahertz, in the radio-frequency (rf) region of the electromagnetic spectrum, while B_1 values are usually only a few hundred microtesla giving an f_1 of about 10 kHz. The size and pulse duration (t) of B_1 can be tailored to give whichever angle of **M** (with respect to $\mathbf{B}_0$) is required, given by $\omega_1 t$, and the rf pulse is named according to its axis and tip angle. For example a '90_x' pulse tips the magnetisation vector 90 degrees about the x-axis (in the rotating frame!) fully into the transverse plane. It is customary to define the rotating x-axis as that in phase with **M** (and perpendicular to $\mathbf{B}_0$) after the first rf pulse used, and to determine the axes of subsequent pulses by their phase relative to that first pulse, i.e. a 90_y or 180_y pulse is 90° or $\pi/2$ rad out of phase (rotating in the transverse plane) with the first pulse. A great variety of NMR studies may be performed simply by combining carefully-designed sequences of rf pulses to manipulate the magnetisation vector at will, probing the environments of the nuclei of interest. When magnetic field gradients are also incorporated into these sequences it is possible to add the capacity for spatial resolution, or imaging, to the available repertoire, and this topic will be developed further in Section 2.6.

The most significant influence in the nuclear environment is usually its own atomic (or molecular) electron cloud. Magnetic shielding results when the electronic orbitals are perturbed by the applied field, and this may displace the Larmor frequency from that which would be expected if there were no electrons present. This displacement is termed the 'chemical shift' and is characteristic for each molecule and free atom, acting as a molecular fingerprint. In imaging the chemical shift phenomenon may be a nuisance if the sample contains more than one significant population species. For example, when both water and lipids are present, an image from the lipid protons will be spatially shifted from those of the water and so ghost images will arise. However this problem may be overcome by exciting only the one species of proton through selective excitation

(explained later in Section 2.7 along with slice selection), and in some instances it can be very useful to be able to image the spatial density of a particular molecule of interest while ignoring others.

2.4 Relaxation

While transverse magnetisation is obtainable through excitation, this is only a temporary condition and the magnetisation vector will eventually return (or relax) to its equilibrium position in alignment with the polarising field. This phenomenon is therefore called 'longitudinal relaxation', or 'spin-lattice relaxation' to reflect the energy exchange between the spin system and the surrounding medium or lattice. The longitudinal component of **M** following a 90° excitation pulse evolves as

$$M_z(t) = M_0 \, (1 - \exp(-t/T_1)) \tag{2.19}$$

where M_0 is the equilibrium value of the longitudinal magnetisation and T_1 (the 'longitudinal relaxation time') will serve as a time constant to describe this process. However even before the transverse magnetisation has been destroyed by spin-lattice relaxation, the phase coherence of the spins will have decayed as the spins dephased under the influence of dipolar interactions between adjacent nuclei (which give rise to a range of resonant frequencies). This dephasing as the spins come to equilibrium between themselves is known as 'spin-spin' or 'transverse' relaxation, and in this way the transverse components of **M** after excitation evolve as

$$M_{x,y}(t) = M_{x,y}(0) \exp(-t/T_2) \tag{2.20}$$

where $M_{x,y}(0)$ is the value of $M_{x,y}$ immediately after the 90° pulse and T_2 is again the relevant time constant. If relaxation is incorporated into eqn (2.17) we get a more realistic set of governing equations for the time evolution of the magnetisation, known as the Bloch equations *(98)*

$$\begin{aligned}
\frac{dM_x}{dt} &= \gamma(M_y B_0 + M_z B_1 \sin \omega_0 t) - \frac{M_x}{T_2} \\
\frac{dM_y}{dt} &= \gamma(-M_x B_0 + M_z B_1 \cos \omega_0 t) - \frac{M_y}{T_2} \\
\frac{dM_z}{dt} &= \gamma(-M_x B_1 \sin \omega_0 t - M_y B_1 \cos \omega_0 t) - \frac{(M_z - M_0)}{T_1} .
\end{aligned} \tag{2.21}$$

These simple relationships are very successful in describing phenomena where the interaction terms causing transverse relaxation are relatively weak, as is the case for spins in liquid state molecules where the molecules are rapidly tumbling. However it is not accurate for the solid state or other slowly moving molecules such as large macromolecules, and there is also no description of how relaxation times depend on the magnitude and fluctuation rates of spin interactions. Although in almost all cases in this work we will be studying protons in liquid water, some of these may be exchanging with protons in more restricted situations, and in any case it is useful to relate observed relaxation with various causative factors, so we should consider the wider picture of relaxation.

In dielectric materials, the fluctuating local dipolar interactions occurring as the molecules and their constituent spins undergo thermal motion must have the appropriate frequency components to stimulate transitions between the energy levels, namely ω_0 or $2\omega_0$, in order to bring about spin-lattice relaxation. In other words where a resonant perturbation of the Zeeman system was necessary for excitation, the same is required for de-excitation, although it need not be supplied in the form of an external rf field. In contrast T_2 processes are also sensitive to components at or near zero frequency (static fields), and the result of this extra sensitivity is that $T_2 \leq T_1$ always. For the simplest 'rapid motion' case the relaxation behaviour was originally described by Bloembergen, Purcell and Pound (the BPP theory)*(99)*, and this is illustrated in Fig 2.1. The existence of two distinct motional regimes within the theory is clear in the graph, separated by a minimum in T_1 where the correlation time of the interaction fluctuation, τ_c, is of the order of the Larmor period. Where $\tau_c^{-1} >> \omega_0$, as in small molecules in liquid state, 'extreme narrowing' conditions exist (referring to the narrow range of frequencies present about ω_0) and T_1 and T_2 are equal and long (on the order of seconds). For highly viscous liquids, concentrated flexible polymers or semi-rigid polymers (i.e. $\tau_c^{-1} << \omega_0$) T_1 again becomes long while T_2 becomes much shorter. The exponential model of transverse relaxation applies to both regimes covered by BPP theory, which are collectively described as being 'motionally narrowed'.

This is not true for solids, where the spectral density becomes more concentrated near zero frequency instead of being evenly spread. This predominance of low frequency components leads to a very short T_2 and a very long T_1. Since T_2 determines the duration of phase coherence (after excitation), in solids this coherence may disappear after only a few microseconds, placing constraints upon the type of experiments possible. The T_1 value, which is always longer than T_2, is not quite so crucial because it only

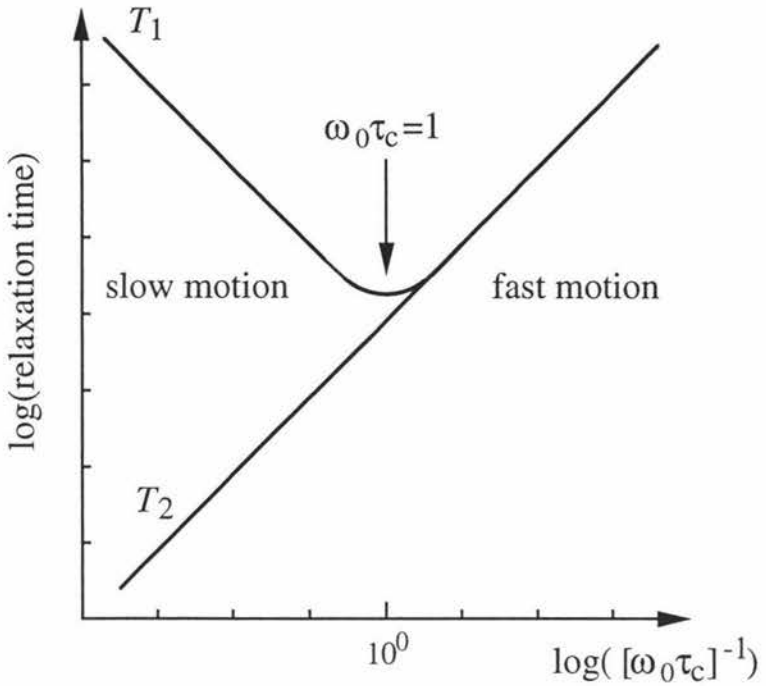

Figure 2.1. T_1 and T_2 relaxation times for the motionally-narrowed regime covered by Bloembergen, Purcell and Pound theory. The relaxation times are plotted as a function of rotational correlation time τ_c for a fixed Larmor frequency ω_0. The T_1 minimum divides the range of τ_c^{-1} values into two regimes which are slow and fast in comparison with ω_0.

determines the time needed for the sample to equilibrate after an experiment and therefore the minimum repetition time between experiments. An ideal sample has the same value for T_1 and T_2, long enough to enable the desired spin manipulation but not so long as to require long repetition, and overall run, times.

Ignoring the limits imposed for solids, it should be remembered that relaxation rates can reflect molecular environments, and provided that T_2 is sufficiently long for imaging they may be utilised to generate revealing image contrast as discussed in Chapter 1.

2.5 Detection

The last essential ingredient for any NMR experiment is detection of the carefully-manipulated magnetisation vector behaviour. The detector is in the form of a coil around the sample, oriented transverse to $\mathbf{B}_0$, so that any magnetisation precessing in the transverse plane will induce a weak emf in the coil oscillating at that same precession frequency. In fact the same rf coil can usually be used for both excitation of the spins and detection of the resulting signal.

The emf received is mixed with a reference oscillator signal, a process called heterodyning. The final signal will oscillate according to the difference in reference and received frequency, giving a dc output if the reference is set to the Larmor frequency. Phase sensitivity is achieved by separately mixing the emf with two heterodyne references which are 90° out of phase. In effect we are observing both orthogonal transverse components of the magnetisation, similar to M_x and M_y. Referring to the first of these as 'in-phase' and to the second as 'quadrature phase', complex notation is the obvious tool to describe the detection process, and the components become known as 'real' and 'imaginary'. If the real part represents the rotating frame x-direction and the imaginary the y-direction, then in complex numbers the transverse magnetisation $M_\perp$ following a 90° rf pulse applied to a relaxed system is

$$M_\perp(t) = M_0 \exp(i\omega_0 t) \exp(-t/T_2). \tag{2.22}$$

The heterodyne signal $S(t)$ where the reference frequency is offset by $\Delta\omega$ from the resonant frequency is

$$S(t) = S_0 \exp(i\phi) \exp(i\Delta\omega t) \exp(-t/T_2) \tag{2.23}$$

where S_0 is the amplitude immediately after the pulse and ϕ represents the absolute phase of the receiver (arbitrary). This time-domain function is known as the 'free induction decay' (FID) because it is a decaying oscillatory emf induced by free precession of the magnetisation. If $\phi = 0$ (and this may be adjusted afterwards in data processing) then the Fourier transform of the FID will give a Lorentzian peak in the real spectrum at $\Delta\omega$. The width of the peak will be determined by T_2 because of the (inverse) relationship between time of decay in the time domain and frequency spread in the frequency domain. This relationship leads us to refer to spin-spin relaxation often by the alternate name of 'broadening'. The exact expression for the spectral linewidth is $(1/\pi T_2)$.

So far we have only considered 'homogeneous' broadening, which is common to each spin packet or isochromat in the sample and arises from the random motion of the spins. Any extra dephasing caused by local differences in the Hamiltonian between isochromats, for example from a non-uniform external magnetic field, is appropriately termed 'inhomogeneous' broadening. If inhomogeneous broadening is present then the apparent transverse relaxation time constant is called T_2^*, and it will be shorter than the simple T_2 value because the decay rate will be faster. Certain pulse tricks, to be introduced in Section 2.8, can be used to reduce inhomogeneous broadening but there is no such opportunity for homogeneous broadening.

2.6 Magnetic Field Gradients and Imaging

In NMR spectroscopy much effort is put into ensuring an extremely uniform applied magnetic field for the spin ensemble so that fine differences in nuclear environment may be reflected in the resonant spectrum. By contrast NMR imaging seeks to use a deliberately varied field to reveal spatial heterogeneity within the sample. Normally the magnetic field profile is designed to vary linearly across the sample, although the extent of variation is many orders of magnitude smaller than the underlying polarising field. Because of this fact the Larmor frequency is only affected by extra field components which are parallel with $\mathbf{B}_0$, and any others only serve to tilt the net field direction very slightly. Thus the new local Larmor frequency

$$\omega(\mathbf{r}) = \gamma B_0 + \gamma \mathbf{G}\cdot\mathbf{r} \tag{2.24}$$

has an extra term for spatial encoding containing **G**, defined as the **grad** of the extra field component which is parallel to B_0, and this simple relationship of Larmor frequency to spatial coordinates **r** is pivotal to imaging. Obviously a Fourier transform will be necessary to convert the time domain signal we observe into a spectrum and eventually into an 'image' in one or more dimensions reflecting the density of spins. For example, if **G** were purely in the x-direction then the spectral data could be regarded as a projection of the spin density onto the x-axis.

To explain further, we can imagine a sample of local spin density function $\rho(\mathbf{r})$ to consist of a large number of small volume elements $\mathrm{d}V$, and the number of spins in each element will be $\rho(\mathbf{r})\,\mathrm{d}V$. From eqns (2.23) and (2.24) the signal from an element will be

$$\mathrm{d}S\,(\mathbf{r},t) = \rho(\mathbf{r})\,\mathrm{d}V \exp\,(\mathrm{i}\omega(\mathbf{r})t)$$

$$= \rho(\mathbf{r})\,\mathrm{d}V \exp\,(\mathrm{i}(\gamma B_0 + \gamma\mathbf{G}\cdot\mathbf{r})t) \tag{2.25}$$

if we neglect relaxation. Normal spin-spin relaxation will be present but it is usually valid to assume that it will be much slower than the dephasing caused by the application of our field gradient. One may also dispense with the γB_0 term because of the nature of heterodyne mixing during detection (provided the reference oscillation is on-resonance). Finally the complete signal amplitude will be an integration over all elements

$$S(t) = \iiint \rho(\mathbf{r})\,\exp(\mathrm{i}\gamma\mathbf{G}\cdot\mathbf{r}t)\,\mathrm{d}\mathbf{r} \tag{2.26}$$

which indeed closely resembles a Fourier transform. Put in another way, we know that there is a correspondence between 'real' space and frequency, but what space corresponds to time (since we conduct our experiments in the time domain)? The solution is a reciprocal space known as '**k**-space' *(2,3)*, defined by

$$\mathbf{k} = (2\pi)^{-1}\gamma\mathbf{G}t. \tag{2.27}$$

Substituting this new idea into eqn (2.26), and showing the logical inverse transform as well, one obtains the Fourier pair of equations

$$S(\mathbf{k}) = \iiint \rho(\mathbf{r})\ \exp(i2\pi\mathbf{k}\cdot\mathbf{r})\ d\mathbf{r} \tag{2.28}$$

$$\rho(\mathbf{r}) = \iiint S(\mathbf{k})\ \exp(-i2\pi\mathbf{k}\cdot\mathbf{r})\ d\mathbf{r}. \tag{2.29}$$

The signal $S(\mathbf{k})$ and spin density $\rho(\mathbf{r})$ are said to be mutually conjugate. Of course we cannot totally ignore the relaxation and other contrast effects put aside earlier for convenience, and the signal will be proportional to these as well as to $\rho(\mathbf{r})$. The choice of imaging pulse sequence determines the extent of each effect.

It was easy to see how one might obtain the density profile along one axis, but how can the technique be stretched to achieve a three-dimensional representation? One standard method is to acquire signal from one plane or layer of the sample only and thus effectively convert the problem into a two-dimensional one. This can be done by exciting only this desired 'slice' of spins with a special 90° rf pulse, and the process is known as 'selective excitation', although this term also covers the method of excitation of nuclei falling within a certain chemical shift range.

2.7 Selective Excitation

Two things are crucial to slice selection, namely the presence of a field gradient during excitation and the bandwidth of the excitation pulse. If the pulse has a bandwidth of 1 kHz, say, then it will disturb spins which have a precession frequency within a range of 1 kHz roughly centred around its own frequency. The range of frequencies present in the sample is greatly increased if a field gradient is applied at the same time, so that for the same pulse bandwidth fewer spins are excited and they will be centred around the 'origin' of the field gradient, where the resonant frequencies are again equal to that of the pulse. Already we have the basic tools for slice selection, but how do we select the size of the rf bandwidth to use?

Selective excitation is based on the principle that the bandwidth of such a pulse is inversely proportional to the pulse duration, much as the signal linewidth is inversely related to the time of decay. Therefore we would use a pulse duration of 1 ms if we were aiming for a bandwidth of 1 kHz, and if a very narrow slice of spins were required then we would use a long pulse duration. Conversely, in order to excite the entire sample a very short pulse would be used. Although the duration is instrumental in attaining the correct tip angle ($\gamma B_1 t$), it is simple to increase or reduce the pulse amplitude B_1 to compensate accordingly. By convention the short, intense and therefore broadband excitation pulses are called 'hard' pulses while the longer, weaker, narrowband pulses are called 'soft'.

The bandwidth is not the only feature of the rf pulse affecting slice selection. The 'shape' of the pulse (amplitude modulation), is very influential in ensuring that a regular rectangular slice of nuclei is excited uniformly and that the nuclei outside this are left largely undisturbed. A simple pulse with a rectangular profile (or constant magnitude) in the time domain yields a 'sinc' function ($\frac{\sin x}{x}$) in the spectrum by Fourier transform, leading to an ill-defined slice with significant side lobes beyond the main excited cross-section. However, the reciprocal nature of the Fourier transform suggests an obvious solution, namely the use of a sinc-shaped pulse in the time domain to achieve a near rectangular slice. Although this assumes that the nuclear spins have a linear response, not strictly true outside small tip angles, this approach is indeed successful *(100)* and widely used for slice selection. The resultant tip angle may be calculated by integration under the sinc profile.

For chemical shift selective excitation, carried out without a field gradient, the aim is usually to select an entire spectral peak corresponding to a molecular component of the sample while excluding other peaks. If the peaks are distinct and well-separated this task is straightforward, and a simple extended duration soft pulse would probably suffice, but where it is necessary to be more precise a gaussian-shaped rf pulse is favoured. This yields another gaussian after a Fourier transform, eliminating the side lobes and approximating the natural peak shape.

2.8 Fourier Imaging in Two Dimensions and the Use of Echoes

Having established an effective method of limiting our experiment to two dimensions (an average over a slice), we must unambiguously encode for these remaining directions. If the slice direction is designated as z in Cartesian coordinates, eqn (2.28) simplifies to

$$S(k_x, k_y) = \iint \rho(x,y) \exp(i2\pi[k_x x + k_y y])\, dx\, dy. \qquad (2.30)$$

Now we can imagine **k**-space to be a plane with x-and y-axes just as we might for real space, and in reality we will be sampling a finite number of points or grid on that **k**-space plane. The way in which the sampling points are distributed on the plane is known as a 'raster', and although we have chosen one based on Cartesian coordinates it is just as valid to choose polar coordinates. In fact the polar raster was the first to be developed in the early days of NMR imaging, but there are certain advantages and weaknesses associated with either type. The Cartesian variant is known as Fourier imaging (FI) and relies upon two separate evolution periods, t_x and t_y, which feature in the expressions $k_x = (2\pi)^{-1}\gamma G_x t_x$ and $k_y = (2\pi)^{-1}\gamma G_y t_y$ according to the previous definition of **k**.

Firstly, when an FID is acquired in the presence of a magnetic field gradient we are obtaining points along a line in **k**-space. We will specify this line to be in the x-direction (k_x). In this case the gradient is known as the 'read gradient'. Secondly, the line being sampled must be moved up and down the corresponding y-axis (k_y) if we are to sample all of the points in available **k**-space. The way in which the intercept of the sampled line can be changed is by applying the gradient G_y, orthogonal to the read gradient, for a period before the sampling takes place. In effect this so-called 'phase gradient' is causing a phase shift which varies linearly with position along the y-axis, as opposed to the read gradient which causes a frequency shift varying along the x-axis.

Because G_y and G_x are applied one at a time and do not overlap, the spins are allowed to evolve along the positive y-axis to the allotted intercept during the phase period t_y before the signal is sampled along the positive x-axis (at that intercept) during the read period t_x. Thus the whole quadrant may be sampled, as shown in Fig 2.2, and if the phase gradient is reversed then the fourth quadrant may be sampled likewise. However we cannot reverse time to sample the second and third quadrant. Instead we can move the time 'origin', where $t_x = k_x = 0$, forward using a spin echo in order to sample before and after the origin (effectively negative and positive time).

Dephasing of spins in a magnetic field gradient following a 90° rf pulse (due to the spread of Larmor frequencies), or in fact any form of inhomogeneous broadening, may be reversed by a second 180° rf pulse at time τ, restoring phase coherence in a 'spin echo' after an identical rephasing period at 2τ. The echo is usually symmetrical about time 2τ, and observed from the point of maximum signal (centre of echo) forward it should

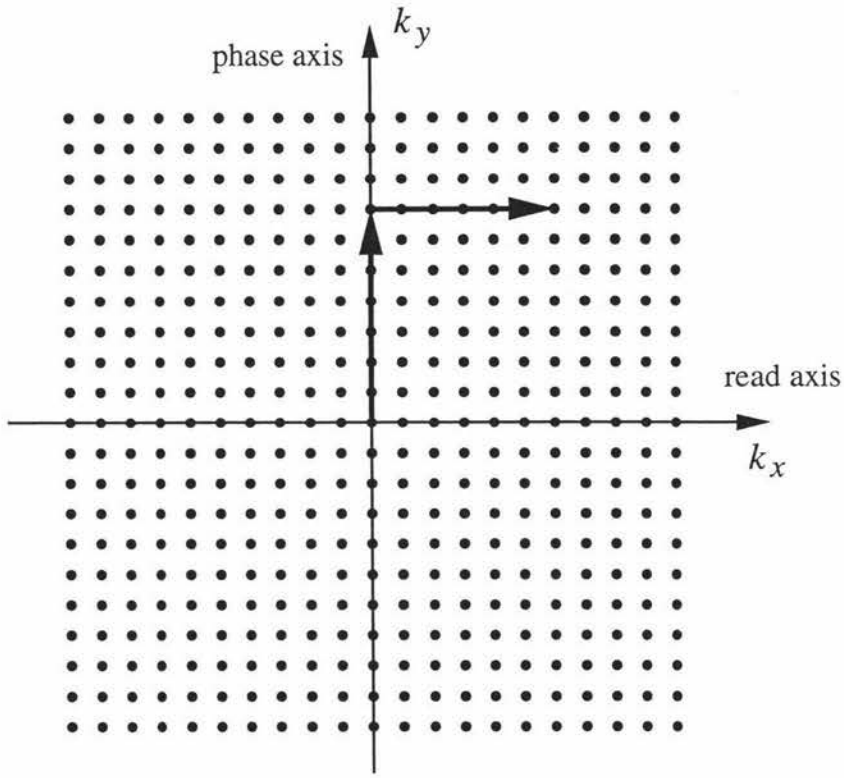

Figure 2.2. The **k**-space sampling scheme for two-dimensional Fourier imaging. The phase and read gradients are applied sequentially, causing evolution firstly in the k_y direction and secondly in the positive k_x direction. In this way a Cartesian raster is used to cover the first quadrant of **k**-space. The fourth quadrant may be sampled using negative phase gradients, and the second and third by the use of echoes. There are N points across the raster, where N is the number of image pixels.

resemble the original FID during the first dephasing, apart from any true T_2 relaxation which will have reduced the ampitude in the meantime. We assume here that the dephasing due to the gradient is much more rapid than the inevitable spin-spin relaxation so that the decay envelope will allow for a significant echo at time 2τ. The phase difference between the two rf pulses is important, and if the first is always taken to be 90_x then a subsequent 180_y will generate a 'positive' echo, while a similar 180_x would generate a 'negative' one (where the magnetisation vector is antiparallel to the one immediately after the 90_x).

An rf pulse is not the only way to form an echo in the presence of a gradient. The reversal of the gradient leading to the dephasing will again restore the phase coherence after an identical period of evolution, giving a 'gradient' echo. It might seem that the gradient echo is also a spin echo because the spins are indeed rephased, but historically the term 'spin echo' was given exclusively to an echo brought about by a refocusing rf pulse. The gradient echo will not refocus any other Zeeman-like phase shifts such as from B_0 inhomogeneity, susceptibility-related field offsets (discussed in Chapter 3),

chemical shift or any other suitable interactions, as the spin echo does. For this reason the decay envelope limiting the echo amplitude is governed by T_2^* rather than T_2. However this may be desirable, rather than simply a disadvantage, if we wish to observe the relaxation behaviour itself, and for both types of echo the lengthening and shortening of the parameter τ allows a spatial measure of transverse relaxation for either T_2 or T_2^* depending on the sequence used (known as T_2 and T_2^* 'maps').

In this way we can map the four quadrants of **k**-space, although strictly-speaking it is possible to do Fourier imaging without echoes (more common when using a polar raster where there is no need of phase evolution). It is usually easiest to avoid dispersion spectra in the imaginary domain, possibly leading to broadening and distortion, by the sampling of both positive and 'negative' time using echoes. The point to begin sampling is then no longer so crucial as it is at the start of an FID. Furthermore the necessary phase period before acquisition of an FID leads to T_2^* relaxation, and this may be orders of magnitude faster than mere spin-spin relaxation. If T_2 is so short that the long minimum delay before an echo is a problem, then it is possible to move the centre of the echo forward somewhat in the acquisition period artificially, as long as the echo is not truncated too much on the leading side. Because the area (amplitude times duration) under the first dephasing gradient (the precursor read gradient) must be the same as that under the first half of the read gradient to get a central echo, a reduction in the size or duration of the precursor will move the echo forward in time.

The value of k_y for each sampling may be chosen by adjusting the phase period t_y between acquisitions, but it is more common to keep t_y constant and instead vary the phase gradient magnitude. If the phase period is varied, any phase shifts arising from field inhomogeneity or spin-spin relaxation during t_y will vary too, risking artefacts from uneven reduction of signal over the range of k_y. Thus the second method, known as 'spin warp' imaging is generally favoured.

It is clear from eqn (2.30) that the outcome of all this of **k**-space sampling, $S(k_x, k_y)$, is the two-dimensional Fourier transform of the spin density $\rho(x,y)$. Therefore to reconstruct $\rho(x,y)$ we must logically perform an inverse Fourier transform on $S(k_x, k_y)$.

2.9 The Versatile Pulse Sequence

The basic spin echo pulse sequence used in this work is shown in Fig 2.3. The 180_y pulse is chosen for the slice selection while a simple hard pulse is used for excitation. The hatching of the phase gradient shows that it is incremented through from the negative to the positive limit. Practically the gradient magnitudes and durations are calculated from the desired experimental parameters such as slice thickness, field of view, number of pixels N (image elements) and acquisition bandwidth Δf (the range of Larmor frequencies corresponding to the read gradient). When setting these there is always a compromise between the ideal parameters and the available signal-to-noise ratio, also remembering that the resulting echo time T_E, between the 90° pulse and the echo centre, will determine the signal loss due to transverse relaxation. Where T is the reciprocal of the acquisition bandwidth, the read gradient duration is NT and the read precursor $NT/2$ if they are the same magnitude. By inspection the read gradient magnitude is given by $2\pi\gamma\Delta f/\text{FOV}$ or $2\pi\gamma\Delta f/N\Delta x$ where FOV is the field of view and Δx is the pixel width. The signal-to noise-ratio will decrease as the bandwidth goes up, and as the pixel size and slice thickness go down.

The repetition time T_R is taken to be the distance between successive excitation pulses, and a T_R value insufficient to allow the spins to equilibrate fully will lead to a reduced magnetisation vector available for the next experiment. If T_1 is not equal at all parts of the image then T_1 contrast will result, and in fact we can calculate a map of T_1 if we run a range of experiments at different repetition times. As mentioned the same can be done for T_2 if we vary the echo time by adding an arbitrary delay before and after the 180_y pulse. A drawback of this method is that molecular diffusion during the extra delay may mean that the eventual signal is not only reduced by T_2 relaxation, but also by dephasing due to the migration of nuclei in the gradient. The whole basis for an echo was the assumption that spins experience the same local Larmor frequency during the successive dephasing and rephasing parts of the cycle, yet diffusion can disrupt this. The extent of the disruption is determined by the rate of diffusion compared to the size of the pixel, and will be discussed more fully in Chapter 3, but it is fairly obvious that as the resolution is increased (the pixel is decreased) it is likely to become more significant. An alternative to get around this problem somewhat is to keep the main imaging sequence constant and to lengthen the echo by adding the arbitrary delay after the excitation pulse but before the read precursor and phase gradient. Diffusion is no longer a problem without the presence of a gradient, and the transverse magnetisation may be conserved during the extra delay by a series of refocussing 180° pulses close together, so that any

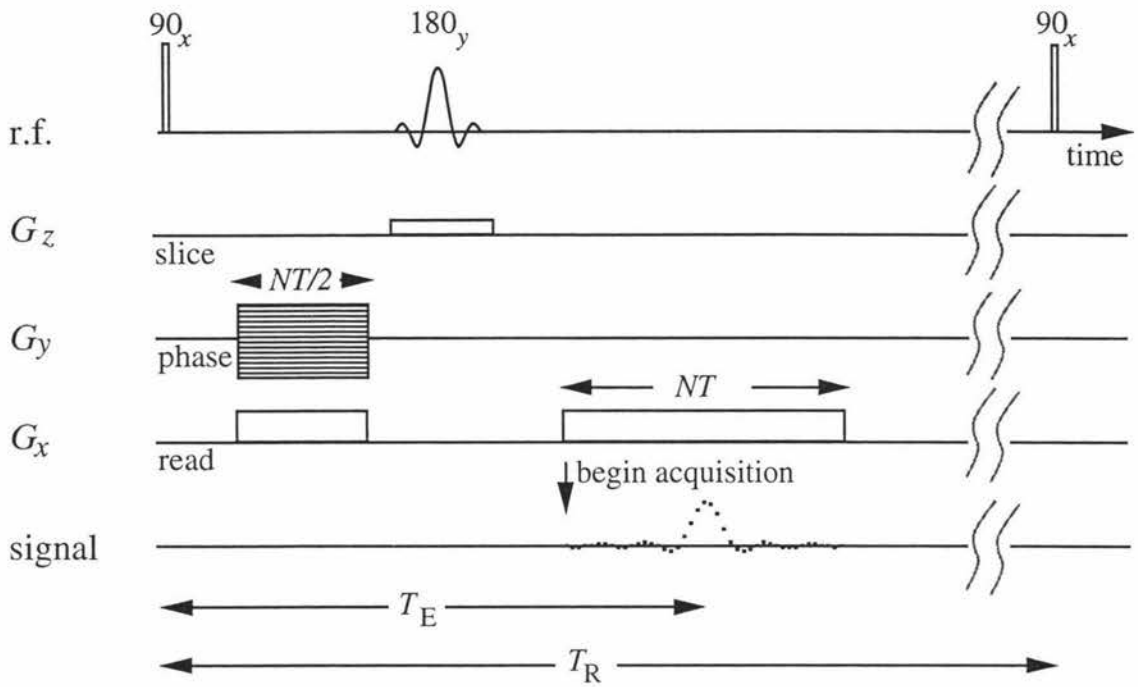

Figure 2.3. The spin warp pulse sequence. T_E and T_R are the echo and repetition times respectively. N is the number of pixels and T the acquisition dwell time (the reciprocal of the acquisition bandwidth). The phase and read precursor gradients may be applied for a time shorter than $NT/2$ if the gradient sizes are proportionately increased.

reduction in signal over the delay can be attributed to spin-spin relaxation. Carr and Purcell first suggested the idea that a train of 180° pulses could be used for successive recovery of phase coherence *(101)*, and later Meiboom and Gill modified the idea by finding that 180_y pulses were more effective in avoiding cumulative effects of small turn angle errors than 180_x pulses *(102)*. Consequently any resultant pulse sequence using such echo trains is usually known as a Carr-Purcell-Meiboom-Gill sequence, and Fig 2.4 shows the one used in our work.

The excitation pulse in the the gradient echo sequence (Fig 2.5) must be slice selective as it is the only rf pulse in the sequence. Notice that dephasing caused by the slice gradient is also rephased in a gradient reversal in order to avoid attenuation during the interval before the start of acquisition. Another variation on the simple spin echo is the addition of chemical shift selection (Fig 2.6) by substituting the hard 90_x with a soft gaussian selective pulse.

This collection of pulse sequences provides a range of tools to probe molecular information other than spin density. In many fields such as biological imaging this is fortunate because the range of spin densities would not distinguish so well between many

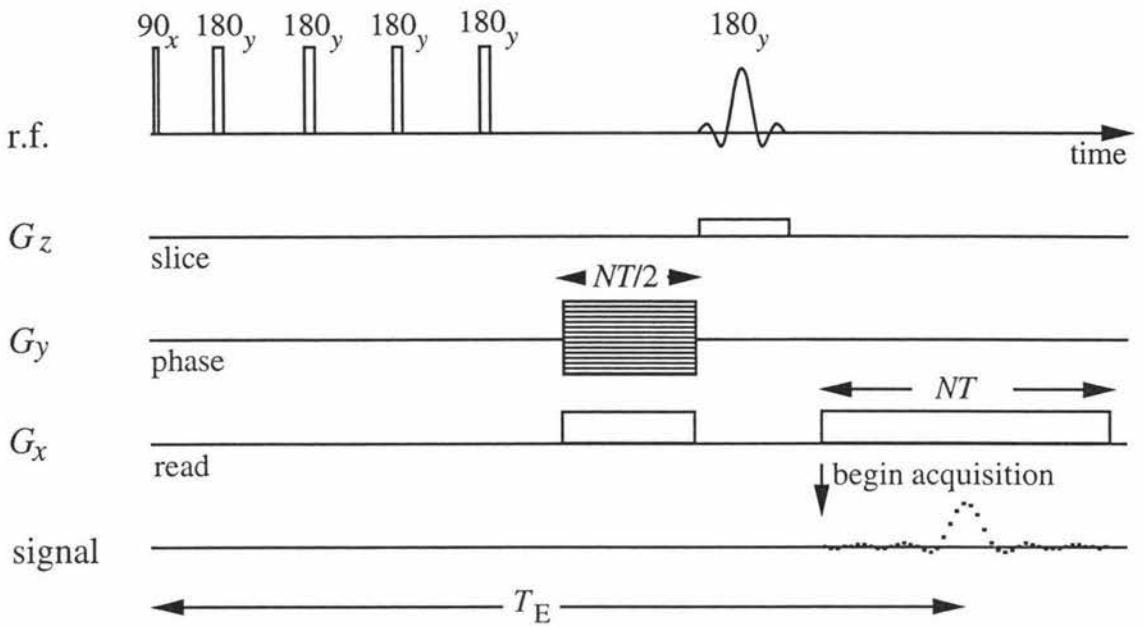

Figure 2.4. The Carr-Purcell-Meiboom-Gill pulse sequence. The number of refocusing 180_y rf pulses may be set to whatever is required.

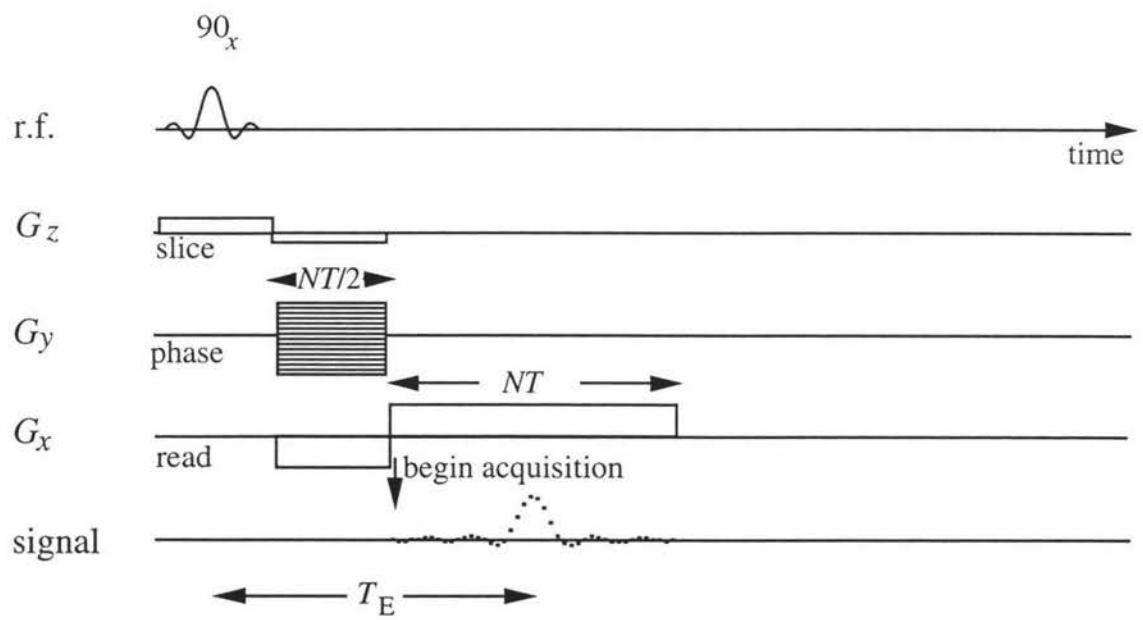

Figure 2.5. The gradient echo pulse sequence. This sequence may be useful when a short echo time is required.

different tissues or materials. The last feature of the molecule to be dealt with is translational motion, random or otherwise. Once again phase encoding is utilised, except now the phase shift occurs in the interval between two short gradient pulses (magnitude g, duration δ and separation Δ) and is proportional to the distance Z moved by each molecule along the gradient direction in that period *(103)*. A new reciprocal

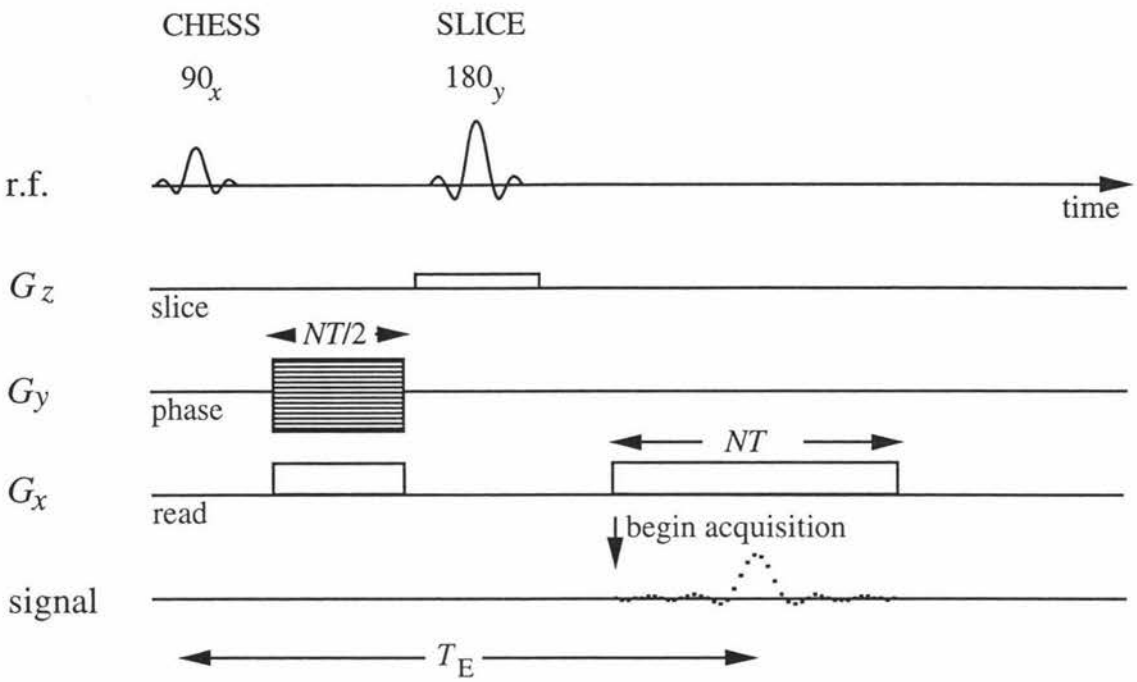

Figure 2.6. The chemical shift selective spin echo pulse sequence. The CHESS soft excitation pulse allows molecular specificity.

space vector **q**, given by $(2\pi)^{-1}\gamma\mathbf{g}\delta$, is introduced in addition to **k** to cope with the extra encoding dimension *(104)*. As usual we will be observing whole ensembles of molecules in each voxel (volume element) rather than individual spins, and so we are ultimately measuring a displacement probability distribution $\overline{P_S}(Z,\Delta)$ known as an 'average propagator' *(105)*. Noting that we will only measure displacement in one direction at a time and therefore that the only non-zero component of **q** (of magnitude q) will be in this direction (usually chosen as the z-axis), our former **k**-dependent equation for the signal, eqn (2.28), becomes

$$S(\mathbf{k},q) = \iiint \rho(\mathbf{r}) \left\{ \int \overline{P_S}(Z,\Delta) \exp(i2\pi qZ)\, dZ \right\} \exp(i2\pi\mathbf{k}\cdot\mathbf{r})\, d\mathbf{r}. \qquad (2.31)$$

The displacement Z will be the projection of the total displacement onto this axis accordingly. The phase spreading due to random diffusive motion of the spins will cause attenuation of the echo, as mentioned before in the context of long echo times in the simple spin echo pulse sequence. By contrast 'ordered' motion or bulk flow will result in a phase shift of the echo consistent within an isochromat. Double inverse Fourier transformation of $S(\mathbf{k},q)$, with respect to both **k** and q, will clearly yield the average propagator weighted by the normal spin density function $\rho(\mathbf{r})\,\overline{P_S}(Z,\Delta)$. It is straightforward to use a spin density image obtained with q=0 to normalise this result and reconstruct $\overline{P_S}(Z,\Delta)$ for each pixel.

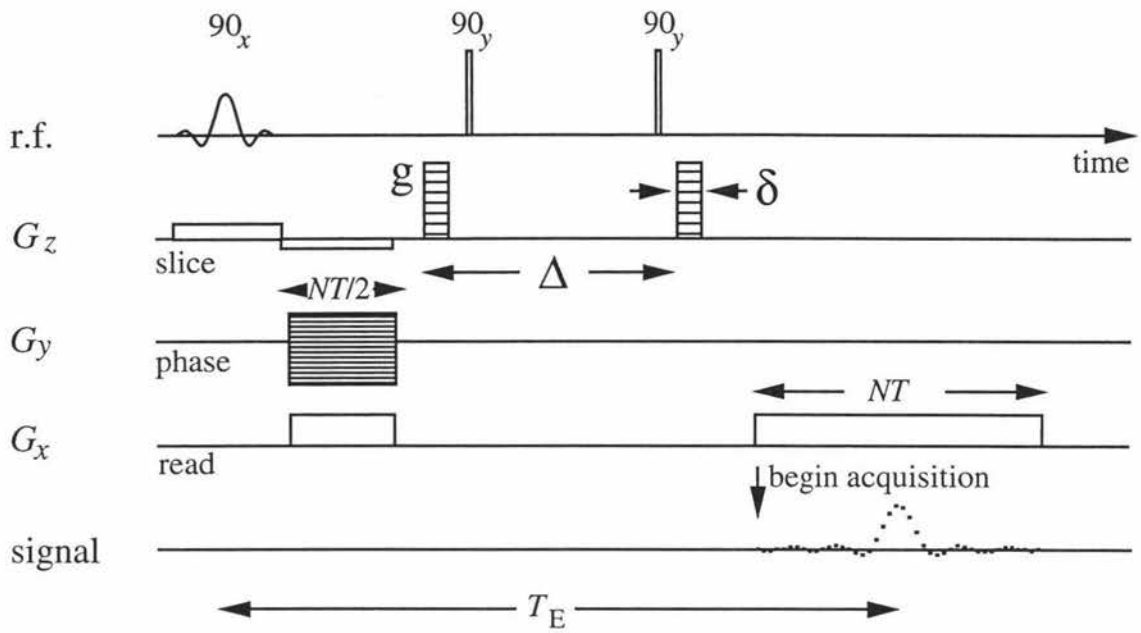

Figure 2.7. The q-space or 'dynamic' imaging pulse sequence, used to measure flow and diffusion. In this case the 180_y hard pulse has been split into two 90_y pulses to enable Δ to be very large. This works by storing the transverse magnetisation along the z-axis between the two hard 90_y pulses, and thus only T_1 relaxation is suffered during that time.

Normal slice selection reduces the problem to three dimensions, and the q-gradient is incremented (from zero to a maximum) between acquisitions just as is done with the phase gradient *(97)*. Therefore the experiment run time will be that of the equivalent two-dimensional imaging experiment multiplied by the number of q-steps. A complex image pair will be processed from each q-step, and then it is possible to Fourier transform each pixel along the q-direction to get $\overline{P_s}(Z,\Delta)$. A map of the molecular self-diffusion coefficient D may be calculated either from the width of $\overline{P_s}(Z,\Delta)$, which is described by the expression $(2D\Delta)^{1/2}$, or from analysis of the image attenuation as a function of increasing q. Generally the latter method is found to be more accurate. The flow displacement $v\Delta$ can be used to calculate a map of local flow velocity $v(\mathbf{r})$. Fig 2.7 shows the pulse sequence to be used for 'dynamic' imaging in Chapter 5.

Chapter 3
The Theory of Susceptibility and Diffusion Effects in NMR Imaging

3.1 Introduction

The resolution available in NMR microscopy is dependent upon a number of factors which limit the sensitivity, such as the polarising field strength B_0 and the T_2 of the sample, but ultimately it is limited by the decrease of the intrinsic signal-to-noise ratio as voxel dimensions are reduced *(106)*. In practice the fundamental resolution deemed possible, taking account of all relevant factors, is never realised and this failure may be attributed to the very inhomogeneities in the material we are hoping to image. The combined influence of magnetic susceptibility variation and molecular diffusion cannot be ignored, especially at high resolution. These factors have been dealt with extensively in the literature*(94,107,108)*, and what follows is intended to summarise the relevant theory, and then provide (in Chapter 4) more comprehensive experimental illustration supporting the concepts.

If we take the simplified model for an atom as essentially consisting of electrons moving around a nucleus, all atoms will contain currents giving rise to magnetic effects. Hence under the influence of an external magnetic field the atoms in a material will experience magnetic polarisation, and there will be an effective bulk magnetic moment in the direction of the field. The material behaves as if it were a magnetic dipole, and can exert a macroscopic influence on distant spins. For paramagnetic or diamagnetic materials there is no permanent magnetic moment, and this is only induced in the presence of a magnetic field. The magnetisation induced in diamagnetic materials reduces the effective field, whereas in paramagnetic substances it is increased. Most biological or organic samples are diamagnetic, as are the ones encountered in this work. The parameter determining the strength of the effect is the magnetic susceptibility χ_m.

For a sample of constant diamagnetic susceptibility χ_m, the magnetic field $\mathbf{B}$ will be altered from the free-space field $\mathbf{B}_0$ by the offset $\chi_m\mathbf{B}_0$. Unfortunately when χ_m varies, this simple equation for the now spatially-dependent $\mathbf{B}(\mathbf{r})$ no longer holds. Interfaces between regions of differing susceptibility will introduce perturbations to the local field, as Maxwell's equations must be satisfied. Consequently the classical boundary conditions across the interface must be obeyed, namely the normal component of $\mathbf{B}$ and also the tangential component of $\mathbf{H}$, the magnetic intensity, must both be continuous. In this way field offsets $\Delta\mathbf{B}_0(\mathbf{r})$ will arise, as taken from the average field $\chi_m^{av}\mathbf{B}_0$ in the

sample, and will cause image distortions dependent on the shape of the boundaries and the reconstruction method used in processing the image.

Such image distortion will inevitably degrade resolution. But in addition diffusional motion of spins across regions of fluctuating field strength, due either to applied imaging field gradients, field offsets $\Delta\mathbf{B}_0(\mathbf{r})$ resulting from susceptibility variation, or indeed to polarising field inhomogeneity, will cause magnetisation dephasing and hence signal attenuation. Furthermore the diffusion rate may itself vary across the sample, in the form of restricted diffusion at local barriers or simply in the molecular self-diffusion coefficient D for the different species present. Hence diffusional signal losses (mentioned briefly in Section 2.9) may be modulated through both susceptibility-related gradients and variable diffusion rates.

In order to clarify the interrelated artefacts resulting from susceptibility discontinuities we will deal with the distortion and attenuation effects separately, using both theoretical simulation and experiment, before considering the final outcome of the two effects in partnership. Although it is easy to see the disadvantages of resolution loss, one should not lose sight of the fact that extra sources of contrast may provide useful signatures for abrupt susceptibility discontinuity of particular or nonspecific geometry.

3.2 Image Distortion Artefacts From Susceptibility Inhomogeneity

For the meantime we shall neglect diffusional effects and concentrate purely on distortional features. Any imperfections in the polarising field and subsequent shimming will not be treated here, except to say that they will contribute further to deviations in the expected magnetic field and gradient profile. Local field offsets $\Delta\mathbf{B}_0(\mathbf{r})$ will be superposed with the usual elements of NMR imaging, i.e. a large uniform $\mathbf{B}_0$ field modulated by smaller linear pulsed field gradients for spatial encoding. Once again only components of the offsets or gradients parallel to $\mathbf{B}_0$ will be effective in altering the Larmor frequency from γB_0 because $\mathbf{B}_0$ is so much larger in magnitude. Thus if $\mathbf{G}$ is the **grad** of the linear pulsed gradient component parallel to $\mathbf{B}_0$ as before and likewise $\Delta B_0(\mathbf{r})$ is the component of $\Delta\mathbf{B}_0(\mathbf{r})$ parallel to $\mathbf{B}_0$, then the local precession frequency is a simple modification of eqn (2.24)

$$\omega(\mathbf{r}) = \gamma B_0 + \gamma\mathbf{G}\cdot\mathbf{r} + \gamma\Delta B_0(\mathbf{r}). \tag{3.1}$$

Following on from eqn (2.26) the imaging time domain signal in the heterodyne detection frame, acquired under the influence of $\mathbf{G}$ applied for time t, becomes

$$S(t) = \iiint \rho(\mathbf{r}) \exp(i\gamma[\mathbf{G}\cdot\mathbf{r}+\Delta B_0(\mathbf{r})]t)\, d\mathbf{r}. \quad (3.2)$$

Returning to the **k**-space formalism established in eqn (2.27), eqn (3.2) and its inverse form a familiar Fourier pair.

$$S(\mathbf{k}) = \iiint \rho(\mathbf{r}) \exp(i2\pi\mathbf{k}\cdot\mathbf{r}) \exp(i\gamma\Delta B_0(\mathbf{r})t)\, d\mathbf{r} \quad (3.3)$$

$$\rho_I(\mathbf{r}) = \iiint S(\mathbf{k}) \exp(-i2\pi\mathbf{k}\cdot\mathbf{r})\, d\mathbf{r} \quad (3.4)$$

However now the reconstructed image $\rho_I(\mathbf{r})$ is no longer a true representation of the real spin density $\rho(\mathbf{r})$. We shall consider only the case of two-dimensional Fourier imaging, although the polar raster case of Projection Reconstruction imaging has also been handled fully in the same literature*(107)*. The outcome of susceptibility effects during slice selection will also be neglected because our slice selection gradient is sufficient in size to avoid slice distortion. To review spin warp imaging (shown already in Fig 2.3), the frequency encoding gradient (or 'read' gradient) magnitude G_x is held constant as time t_x evolves, whilst the phase gradient magnitude G_y is instead incremented between scans and the equivalent phase encoding time t_y is kept constant for all scans. The relevant **k**-space expression (corresponding to eqn (2.30)) becomes

$$S(k_x,k_y) = \iint \rho(x,y) \exp(i2\pi k_x[x+\Delta B_0(x,y)/G_x]) \exp(i2\pi k_y y) \exp(i\gamma\Delta B_0(x,y)t_y)\, dx\, dy \quad (3.5)$$

For the case of the phase encoding direction, immediately after G_y has been switched off each element of the object possesses a phase shift $\exp(i\gamma\Delta B_0(x,y)t_y)$ dependent on position. However a spin echo, used at all times in this study, will result in the refocusing of phase shifts at the echo centre, allowing us to restrict our consideration of distortion artefacts to the read direction only.

By contrast, the frequency encoding direction exhibits a much more dramatic perturbation. We know that the contribution of elements in the object to the final image is calculated by obtaining the inverse transformation of $S(k_x,k_y)$, but even by inspection it is evident that an original element at (x_0,y_0) will contribute to a single element in the reconstructed image which is displaced from the starting position along the x-axis by $(\Delta B_0(x_0,y_0)/G_x)$.

At this point we may observe that positional displacement arising from such susceptibility inhomogeneity scales as $\chi_m(x,y)B_0/G_x$, and therefore will worsen as B_0

goes up unless the read gradient G_x is proportionally increased. From another viewpoint, for a specific B_0, as G_x or indeed the acquisition bandwidth Δf is reduced, the distortion will become more pronounced. Obviously the condition for avoiding distortion is that when the shift $\Delta B_0(x,y)/G_x$ is less than the pixel size Δx_{pixel}, or alternatively when the field offset is less than the range in applied frequency encoding field (read gradient) over Δx_{pixel}. These properties have far-reaching consequences in NMR microscopy, where the necessity to optimise the signal-to-noise ratio in order to push back the boundaries of resolution has traditionally suggested the utilisation of ever larger B_0 fields and small T_2-optimal bandwidths. In light of this it is perhaps not surprising that the best true resolution reported to date was obtained in an electromagnet of a mere 2.1 T polarising field.

In order to visualise how such positional artefacts might affect an image it is necessary to resort to a specific sample geometry. A simple example for which it is possible to reach an analytical solution is a long cylinder embedded in a medium of differing χ_m. In the biological context of later chapters, a cylinder forms a passable though limited analogy for the vascular vessels found in plants, provided the cross walls are sufficiently vertically removed from one another to satisfy the requirement for a long cylinder. $\mathbf{B}_0$ may be oriented either along the long axis of the cylinder or in the transverse direction, giving entirely different results.

Fig 3.1 shows the orientation of axes used for solution of $\Delta B_0(x,y)$ in such a sample geometry, where the image slice is again in the x-y plane and $r^2 = x^2 + y^2$. χ_{m2} is assigned to the central cylinder of radius a, and the surrounding medium has a diamagnetic susceptibility of χ_{m1}. By solving Laplace's equation for the magnetic scalar potential under the classical boundary equations mentioned above in Section 3.1, the local field offset (the difference caused by the embedded cylinder) may be found *(109)* for the cases of $\mathbf{B}_0$ normal to the slice plane inside

$$\Delta B_0(x,y) \approx (\chi_{m2}-\chi_{m1})B_0 \tag{3.6}$$

and outside the cylinder

$$\Delta B_0(x,y) = 0, \tag{3.7}$$

as well as transverse $\mathbf{B}_0$ inside

$$\Delta B_0(x,y) \approx \frac{\chi_{m2}-\chi_{m1}}{2} B_0 \tag{3.8}$$

and outside the cylinder

$$\Delta B_0(x,y) \approx \frac{\chi_{m2}-\chi_{m1}}{2} \frac{a^2}{r^2}\left[\frac{2y^2}{r^2} - 1\right] B_0. \tag{3.9}$$

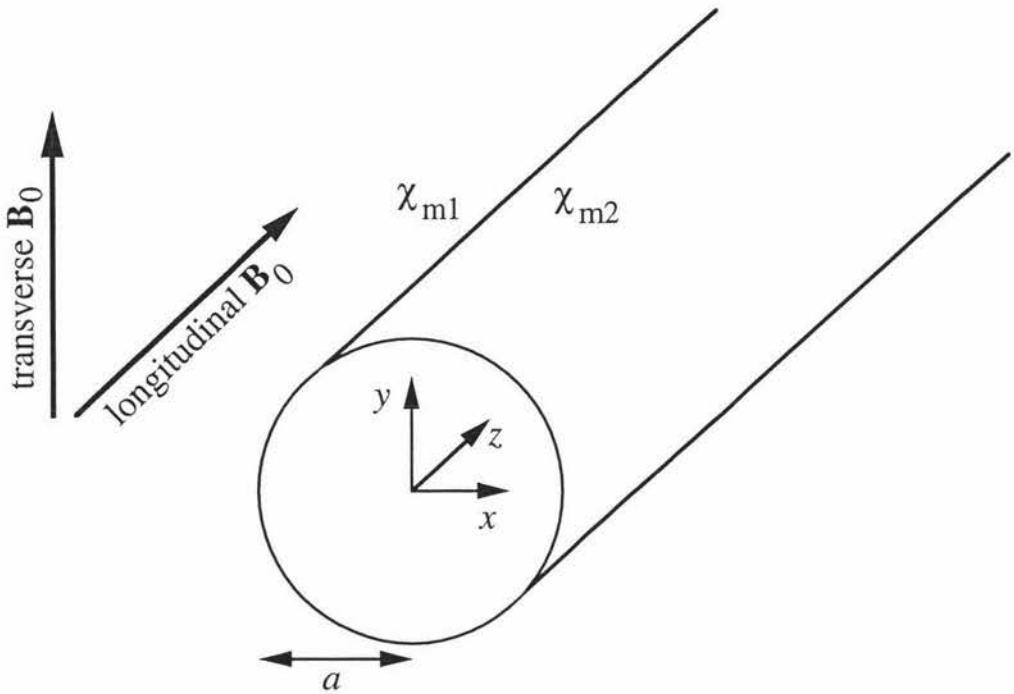

Figure 3.1. Schematic diagram showing the axis orientation used to find analytical solutions for susceptibility-related field offsets $\Delta B_0(x,y)$ around a long cylinder. The image slice is taken to be in the x-y plane. The solutions are trivial for all except the case of offsets outside the cylinder due to a transverse $\mathbf{B}_0$.

The field inside the cylinder is uniform irrespective of $\mathbf{B}_0$ direction, a property utilised in high-resolution NMR spectroscopy by employing cylindrical NMR tubes. This simply results in a constant Zeeman shift, so we may instead turn our attention to the exterior of the tube only. The trivial result for normal $\mathbf{B}_0$ suggests that care with orientation of some samples may minimise or totally eliminate distortion in the image. This leaves the only case of interest for the purposes of this study as $\Delta B_0(x,y)$ outside the cylinder, for transverse $\mathbf{B}_0$. The significance of transverse orientation relates particularly to the common use of transverse solenoidal rf receiver coils in NMR microscopy, in order to achieve a maximum signal-to-noise ratio and so resolution. Yet again, attempts to improve resolution may in fact impair it. Electromagnets are also usually associated with the same orientation, as well as the more general case of any sample which is impossible to reorient as mentioned above, and these set-ups will suffer the same problems.

Neglecting the trivial solutions from this point on, it is useful to note that $\Delta B_0(x,y)$ scales as a/r, and hence resulting positional distortion will not be dependent on the overall dimensions of the problem. This is in direct contrast to the diffusive effects we will encounter later, which may often be the predominant hindrance to the imaging of microscopic systems, above the fundamental sensitivity limitation set by the voxel size relationship to the signal-to-noise ratio.

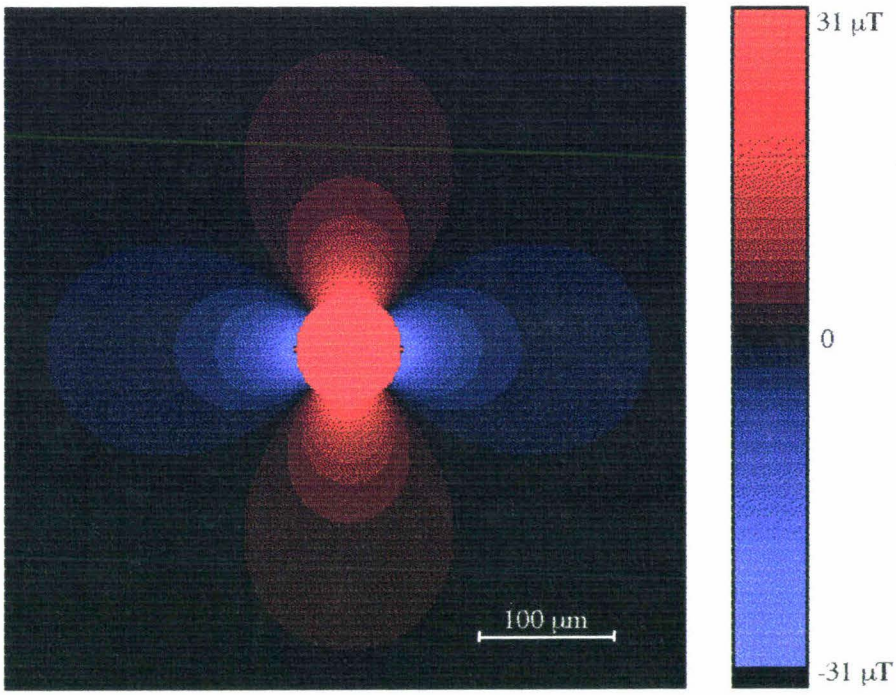

Figure 3.2. Distribution of magnetic field offsets ΔB_0 around a cylinder embedded in a surrounding medium of differing magnetic susceptibility χ. The external field $\mathbf{B}_0$ is oriented vertically in the slice plane and perpendicular to the long axis of the cylinder, causing both positive (red) and negative (blue) offsets. This map is derived using eqn (3.9). Parameters: B_0 = 7 T, $\Delta\chi_m = 9 \times 10^{-6}$, Δx = 2 μm, N = 256.

The simulation by computer of positional displacements may be easily performed by simply displacing each pixel appropriately by $\Delta B_0(x,y)/G_x$, and applying digital interpolation to give a smoother, more realistic image. This involves the transfer of pixel intensity proportional to the extra-integral portions of computed pixel shifts onto the next pixel, e.g. a computed shift of 6.5 pixels would result in half of the original pixel intensity travelling to the sixth pixel and half to the seventh one. Inevitably there will be regions of intensity concentration which are brighter than the object intensity and also other regions which will lose net intensity and will appear as dark regions. We should note in passing that it may not be possible to obtain a completely 'smooth' image with linear interpolation. Where two adjacent pixels have shifts which are more than one pixel in difference spurious lines will appear.

Fig 3.2 shows the map of $\Delta B_0(x,y)$, calculated using a susceptibility mismatch (χ_{m2}-χ_{m1}) of -9 x 10^{-6} and a B_0 of 7.05 T. This $\Delta\chi_m$ is the approximate value for mismatch between water and air, a common interface found in plants, usually between the aqueous cytoplasm and the intercellular air spaces, and the B_0 figure corresponds to a 300 MHz superconducting magnet as used in this lab. Notice that the interior of the cylinder has a large uniform negative field offset, while there are negatives lobes above and below, and positive lobes on either side. As each side has a positive offset, the pixels there will

all move in the same direction along the x-axis. If the negative of $\Delta\chi_m$ is taken, the map is inverted, swapping the positive and negative lobe orientations and meaning that all pixel shifts would simply change to the opposite direction. Due to the symmetry in the field offset map, when $\mathbf{B}_0$ is aligned in the x-direction instead of in the y the positive and negative lobes will again just swap, inverting the image shifts horizontally.

Fig 3.3 depicts the object used, the map of total field other than B_0, and the resulting image by simulation. The cylinder in this case has been coaxially centred in another 'circular' medium, and the outer medium has a finite signal intensity while the inner has been assigned no signal to contribute to the image, because we are not interested in the Zeeman shift-like effects present in the tube due to the uniform offset. The bandwidth Δf used was 60 kHz, corresponding to a read gradient of 2.8 T m^{-1} over a field of view of 500 μm. This rather idealistically small field of view would be well-suited to discern structures on the order of 10 μm or less, such as cells. The 'total field' map illustrates how the uniform frequency encoding gradient profile is disturbed in and near the cylinder, giving anomalous positions after reconstruction into an image. The typical resulting 'arrowhead' distortion is displayed. Such distortions were first proposed by Ludecke *et al (110)*. On the left the pixels have shifted away from the central tube to form the point of the arrowhead, whereas on the right the pixels have moved, also to the left, toward the tube and have flattened the curved edge. At the three points of the arrow the pixel intensities have been concentrated or 'focused' into bright spots, and with even smaller bandwidths diffuse, slightly dark areas appear between these spots. This simulation is not just an academic exercise, as at this plausible bandwidth plant cells could be quite misshapen. The process could easily be adapted to perform the same function for a spherical sample rather than a cylinder, but we will restrict our study to the latter example rather than unnecessarily duplicate the technique for little gain in information.

3.3 Image Intensity Modulation By Diffusive Attenuation in Homogeneous Systems

It was reported in an earlier paper by Posse and Aue *(111)* that diffusional signal losses may be spatially dependent in the presence of local susceptibility-related gradients, but first we must consider the extent of the attenuation in a homogeneous system. For the migration of molecules with self-diffusion coefficient D, the signal attenuation following the application of a time-dependent gradient $\mathbf{g}(t)$ at time t is given by the Bloch-Torrey equation *(112)*

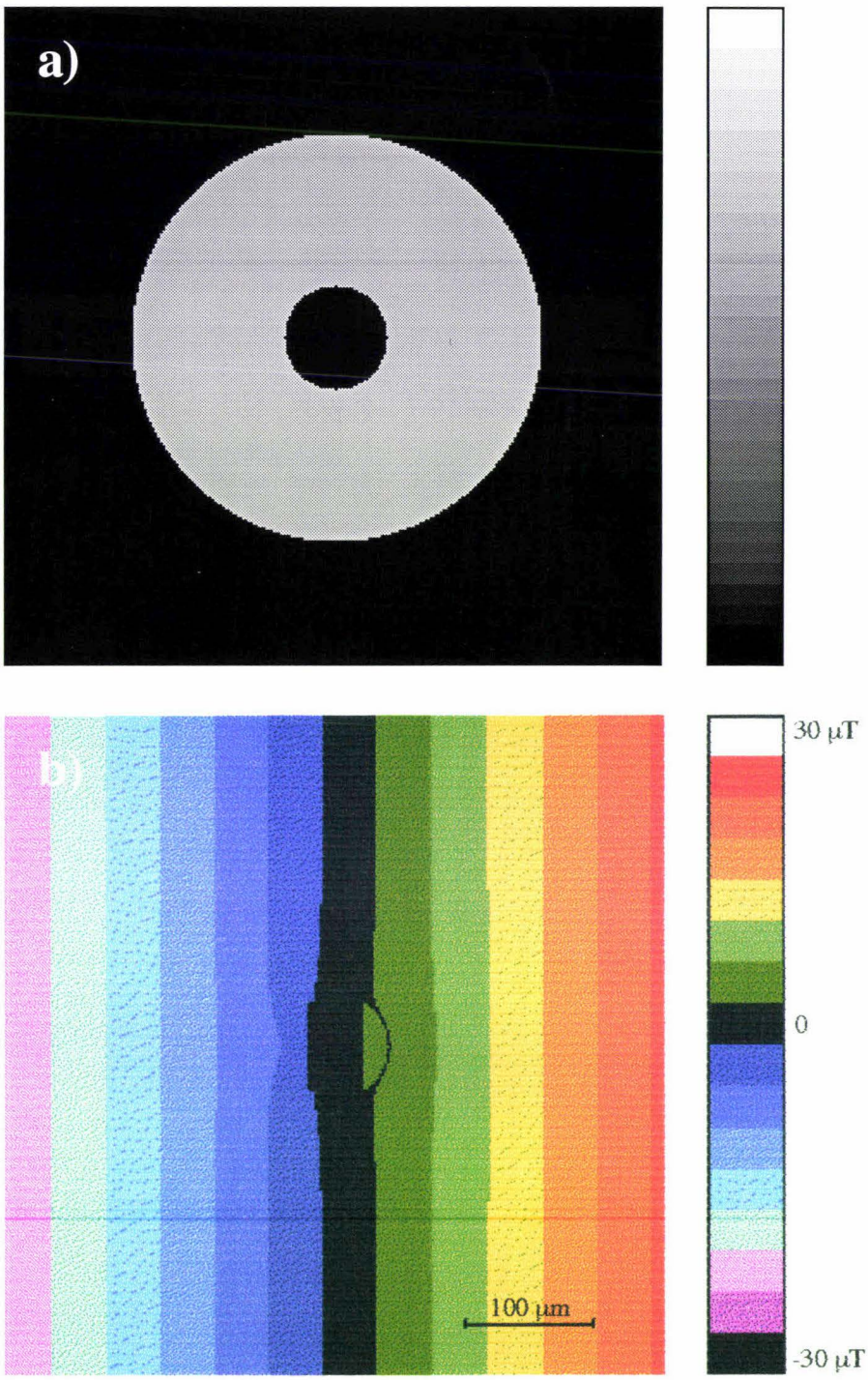

Figure 3.3. Computer-simulated images showing the distortion caused by susceptibility inhomogeneity. (a) Object to be imaged, consisting of a cylinder (contributing no signal) embedded in another cylindrical medium. (b) Map of the 'total' magnetic field calculated by summing the applied read gradient and the field offsets. The uniform read gradient is disturbed near to the cylinder, resulting in pixel shifts when the final image is reconstructed. (c) Final image showing characteristic arrowhead distortion, derived using the $\Delta B_0(x,y)/G_x$ image element shifts. Parameters: B_0 = 7T, $\Delta\chi_m$ = 9 x 10^{-6}, bandwidth = 60 kHz, Δx = 2 μm, N = 256.

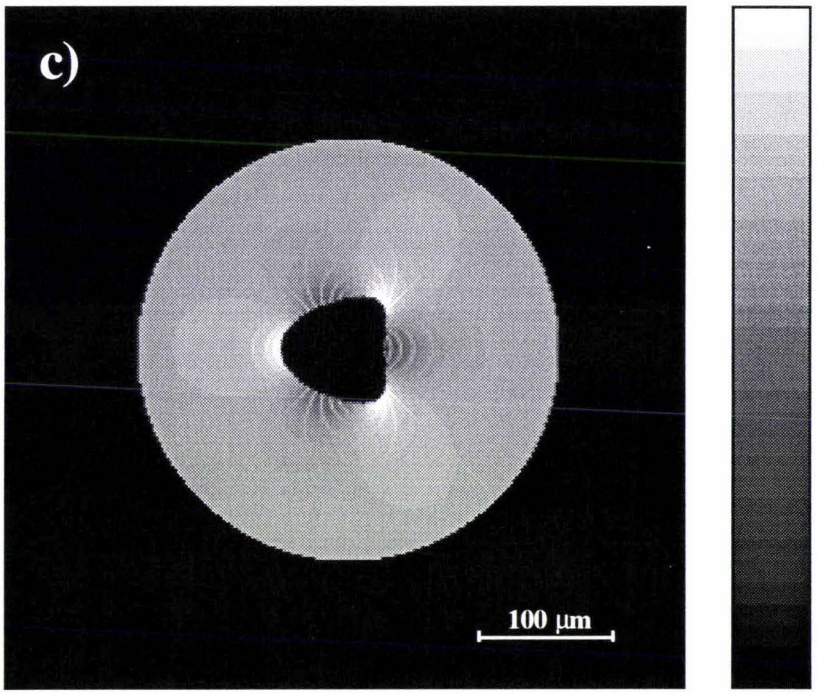

Figure 3.3 (c)

$$A(t) = \exp[-\gamma^2 D \int_0^t (\int_0^{t'} \mathbf{g}(t'')\, dt'')^2\, dt']. \qquad (3.10)$$

Note that $\mathbf{g}(t)$ is the effective gradient, so the sign will be inverted following phase inversion by 180° radio frequency pulses. Eqn (3.10) yields a factor of $\exp(-\frac{1}{3}\gamma^2 G^2 D t^3)$ for a steady, uniform gradient $\mathbf{G}$ of magnitude G, imposed for a time t. For a pair of closely-spaced gradient pulses of duration $\frac{1}{2}t$ and separation $t' \approx \frac{1}{2}t$, the attenuation is $\exp(-\frac{1}{12}\gamma^2 G^2 D t^3)$. Once again we must treat the phase and frequency encoding gradients separately because they clearly possess different $\mathbf{g}(t)$ functions in our pulse schemes, and furthermore the magnitude G of the phase encoding gradient is varied as $\mathbf{k}$-space is sampled, a fundamental distinction from the constant G of the read gradient.

Since the phase gradient is applied as a single rectangular pulse, the former of the two expressions above applies. Directly following the imposition of the phase gradient (of duration t_y) the k-dependent attenuation factor A_p will be *(108)*

$$\begin{aligned} A_p(k_y) &= \exp(-\tfrac{1}{3}\gamma^2 G_y^2 D t_y^3) \\ &= \exp(-\tfrac{4}{3}\pi^2 k_y^2 D t_y). \end{aligned} \qquad (3.11)$$

Additional to this is the usual delay to the echo centre, of duration (T_E - t_y), during which there occurs further signal attenuation due to the residual phase intentionally induced by the phase gradient, even though no other gradients are applied in this time (in the y-direction). From eqn (3.11) the extra factor for our pulse sequence is in the form of $\exp(-4\pi^2 k_y^2 D(T_E - t_y))$, leading to the final result

$$A_p(k_y) = \exp(-\tfrac{1}{3}\gamma^2 G_y^2 D t_y^3)\exp(-\gamma^2 G_y^2 D t_y^2 (T_E - t_y))$$
$$= \exp(-\tfrac{4}{3}\pi^2 k_y^2 D t_y)\exp(-4\pi^2 k_y^2 D(T_E - t_y)). \qquad (3.12)$$

The most striking characteristics to be noted are the strong attenuation experienced at high k_y and significantly the total absence of attenuation at $k_y = 0$, meaning that although the sharp features of the image will be blurred or smoothed, the average intensity, determined by the height of the echo at $k_y = 0$, will remain unchanged. If larger gradients are available then the blurring effect may be reduced by decreasing the phase encoding period t_y (and increasing G_y proportionally).

The frequency encoding gradient also generates a form of k-dependent attenuation, as well as a second more influential attenuation at the echo centre. The former concerns again an image blurring arising from t^3-governed signal attenuation *(113)* which follows the echo centre ($k_x = 0$), remembering that in this case k_x varies as time evolves rather than with incrementation of the gradient strength as in phase encoding. The resulting 'point spread function', a useful function in the description of smoothing effects, is complicated by the asymmetry of the attenuation exponent on either side of the the echo centre, i.e for negative and positive values of t_x and so k_x. The overall result is a fairly weak smoothing effect which we shall neglect, especially in comparison with the second more important effect concerning the action of the read gradient pair together in inducing significant attenuation of the echo amplitude at $k_x = 0$. The typical factor arising for this may be derived from the expression $\exp(-\gamma^2\delta^2 g^2 D(\Delta - \tfrac{1}{3}\delta)$*(103)*, where δ is the duration of each gradient pulse (equal for the two at the time of the echo maximum) and Δ represents the separation of the pulses, measured between the two leading edges of the pulses. In our displayed scheme δ is simply $\frac{1}{2}t_x = \frac{1}{2}NT$, NT being the acquisition time, and Δ may be taken as $(T_E - \frac{1}{2}NT)$, giving the full general attenuation expression *(108)*

$$A_{pf}(0,k_y) = \exp(-\tfrac{1}{3}\gamma^2 G_y^2 D t_y^3)\exp(-\gamma^2 G_y^2 D t_y^2 (T_E - t_y))$$
$$\times \exp(-\gamma^2 G_x^2 (\tfrac{1}{2}NT)^2 D(T_E - \tfrac{2}{3}NT)). \qquad (3.13)$$

For the minimum possible echo time, T_E is approximately NT, and t_y may also be assumed to be essentially $\frac{1}{2}NT$, simplifying eqn (3.13) to

$$A_{pf}(0,k_y) = \exp(-\frac{1}{6}\gamma^2 G_y^2 D(NT)^3)\exp(-\frac{1}{12}\gamma^2 G_x^2 D(NT)^3)$$
$$= \exp(-\frac{8}{3}\pi^2 k_y^2 DNT)\exp(-\frac{4}{3}\pi^2 k_x^{max2} DNT) \quad (3.14)$$

with k_x^{max} as the maximum of the k_x-raster, $(2\pi)^{-1}\gamma G_x(\frac{1}{2}NT)$. We can now observe that the effect will be strongly dependent on N, the number of pixels and Δf, the bandwidth. As T is the acquisition dwell time and the reciprocal of the sampling bandwidth Δf, a decrease of Δf will cause an increase in T and a deepening of attenuation too. Hence diffusive attenuation works in tandem with positional displacement to degrade resolution as the bandwidth is decreased in the search for improved signal-to-noise ratio.

The first component of eqn (3.14) represents the phase gradient smoothing effect and the second an intensity loss of the complete image, assuming the local gradient to be uniform as stated. The relative influences of these terms may be described by the introduction of a convenient parameter Δx_{diff}, which is the rms displacement of the spins over the acquisition period NT. Comparison of Δx_{diff} with Δx_{pixel}, the dimension of the pixel, gives a more intuitive feeling of the effect. Note that $k_x^{max} = k_y^{max} = (2/\Delta x_{pixel})$, and also that Δx_{diff} may be approximated as $(2DNT)^{1/2}$. In the case of Δx_{diff} approaching Δx_{pixel} in size, $(2k_x^{max})^2 2DNT$ and $(2k_y^{max})^2 2DNT$ will approach unity, and the second term will reduce the image intensity to 0.2 of the original. In comparison, by Fourier transform of the first term we see a spreading or blurring over adjacent pixels only. Consequently the smoothing effect will be overwhelmed, and insignificant for the case of homogeneous environments, but the situation may need to be reconsidered for treatment of heterogeneous environments.

3.4 Image Intensity Modulation By Diffusive Attenuation in Heterogeneous Systems

The assumption of uniform D and G was for the purposes of clarity only because there would be little point in real life in imaging such a sample. In order to deal with molecular motion in non-uniform environments, further insight into the nature of the motion is required. This may be roughly described by the regimes known as fast and slow 'exchange'*(114)*. The general phenomenon of 'exchange' may be thought of simply as the interchange of molecules or spins between populations which have unequal parameters such as precession frequency, relaxation rate, diffusion coefficient, binding state and so on. A common example of this is chemical shift exchange, where the populations of spins involved have different chemical shifts and so Larmor frequencies. Thus exchange may be characterised in terms of two parameters, the rms frequency

fluctuation $(\overline{\Delta\omega_0^2})^{1/2}$ between the sites or populations and the average fluctuation correlation time τ_c effectively separating them. To explain for our case of field inhomogeneities, spins will sample a range of local Larmor frequencies $(\overline{\Delta\omega_0^2})^{1/2}$ within the sample in the duration of the experiment and they will take an average time τ_c to diffuse over the distance of the local field variation. By definition fast and slow exchange are given by the criteria $\overline{\Delta\omega_0^2}\,\tau_c^2 << 1$ and $\overline{\Delta\omega_0^2}\,\tau_c^2 >> 1$ respectively *(94,114)*. In general fast exchange has the effect of blurring the distinction between dissimilar populations to the observer. In the instance of chemical exchange between two populations of unequal precession frequency, one might expect to see the two distinct frequencies in an NMR experiment for slow exchange, but for fast exchange only one 'average' value of precession will be observed.

We are considering heterogeneity resulting in disturbance of either the local magnetic field or the local self-diffusion coefficient only here, and the former case of diffusional migration across a region of local magnetic field offsets, $\Delta B_0(\mathbf{r})$, will be dealt with first. As mentioned the Larmor frequency experienced by the spins will fluctuate with their progress, with the rms frequency range $(\overline{\Delta\omega_0^2})^{1/2}$. In fast exchange the frequency spectrum expected from the applied gradient will collapse, leading to an absence of either phase or frequency distortion, with a relaxation term of $\exp(-2\,\overline{\Delta\omega_0^2}\,\tau_c t)$ at the echo at time $2t$. In slow exchange there is inhomogeneous broadening in the spectrum, which will become evident in the different results using spin and gradient echo pulse sequences as it can be refocused in a spin echo. Even with this refocusing there is still a residual echo attenuation term at $2t$ associated with slow exchange, $\exp(-\frac{2}{3}\overline{\Delta\omega_0^2}\,\tau_c^{-1}t^3)$, equivalent to the factor $\exp(-\frac{2}{3}\gamma^2G^2Dt^3)$ mentioned earlier where G will be obtained from $\nabla(\Delta B_0(\mathbf{r}))$ as usual. Reduction of the effective echo time $2t$ by means of a CPMG train (discussed in Section 3.5) offers improvement for the slow exchange attenuation, but not the fast exchange T_2-like relaxation. Once again a rise in B_0 associated with sharper images will exacerbate both the fast and slow exchange effects by increasing $(\overline{\Delta\omega_0^2})^{1/2}$.

We must determine the exchange criterion which applies in this context by estimation of likely $(\overline{\Delta\omega_0^2})^{1/2}$ and τ_c values. Given that the size of $(\overline{\Delta\omega_0^2})^{1/2}$ is of order $\gamma B_0 \Delta\chi_m$, our fairly severe choice of $\Delta\chi_m = -9 \times 10^{-6}$ will lead to spectral fluctuations of about 17×10^3 rad s^{-1} at the most, and any much less than 60 rad s^{-1} will be lost in the intrinsic linewidth due to T_2 relaxation. The correlation time τ_c is of the order $\xi^2/2D$, where ξ is the associated correlation length representing the length over which the field variation

occurs. To fulfil the fast exchange limit $\overline{\Delta\omega_0^2}\,\tau_c^2 << 1$, the example of 60 rad s^{-1} (the easiest to satisfy) would require a correlation time much less than 17 ms, and using the worst likely case of freely-diffusing water molecules this demands a correlation length much less than 9 μm. Larger $(\overline{\Delta\omega_0^2})^{1/2}$ or smaller D only leads to yet smaller ξ values. Since intrinsic NMR transverse resolution is constrained to about 5 μm at the extreme, heterogeneity on the scale of the pixel dimension or more, i.e. discernible by NMR microscopy, must fall into the slow exchange category. This broadly includes surfaces with radii of curvature of more than a few microns.

The remaining question is whether heterogeneity too small to be visible in the image, as must surely be present in living cellular systems, can nevertheless cause significant additional T_2 relaxation (via fast exchange). A range of T_2 values arising from the fast exchange relaxation term at many correlation lengths and $(\overline{\Delta\omega_0^2})^{1/2}$ values indicates the possible magnitude of the phenomenon (Fig 3.4). According to fast exchange conditions only the portions of the curves which obey $\overline{\Delta\omega_0^2}\,\tau_c^2 \leq 1$ are considered and plotted. Each curve, representing a certain $(\overline{\Delta\omega_0^2})^{1/2}$ value, shows that the transverse relaxation time decreases as ξ increases, until the point where fast exchange no longer applies. Nearly all the curves have regions of T_2 below 20 ms or so, where the relaxation rate would probably be faster than that from the background T_2 of the majority of just such cellular systems, and so would result in noticeable extra relaxation. The graph indicates that only heterogeneity (e.g. cells) of less than about 3 μm can be included in this fast exchange regime.

These figures suggest that fast exchange phenomena may indeed create problems in cases of microscopic heterogeneity and hinder efforts to operate effectively right down at the fundamental limits of resolution, depending upon the magnitude of the field offsets, but they will not be included in the general theory here because there is no distortion involved and the extra relaxation would not be distinguished from inherent T_2. In some cases there could be difficulty in estimating the degree of variation on a level which is too fine to be seen in an image (without destructive light microscopy). Moreover the situation would be less noticeable for susceptibility mismatches other than water/air (a gas-liquid interface), as might be found in the interior of cells, i.e. for ξ less than about 1 μm. Thus fast exchange will be neglected for the time being, but kept firmly in mind when interpreting plant images later where the sample heterogeneity is not entirely known.

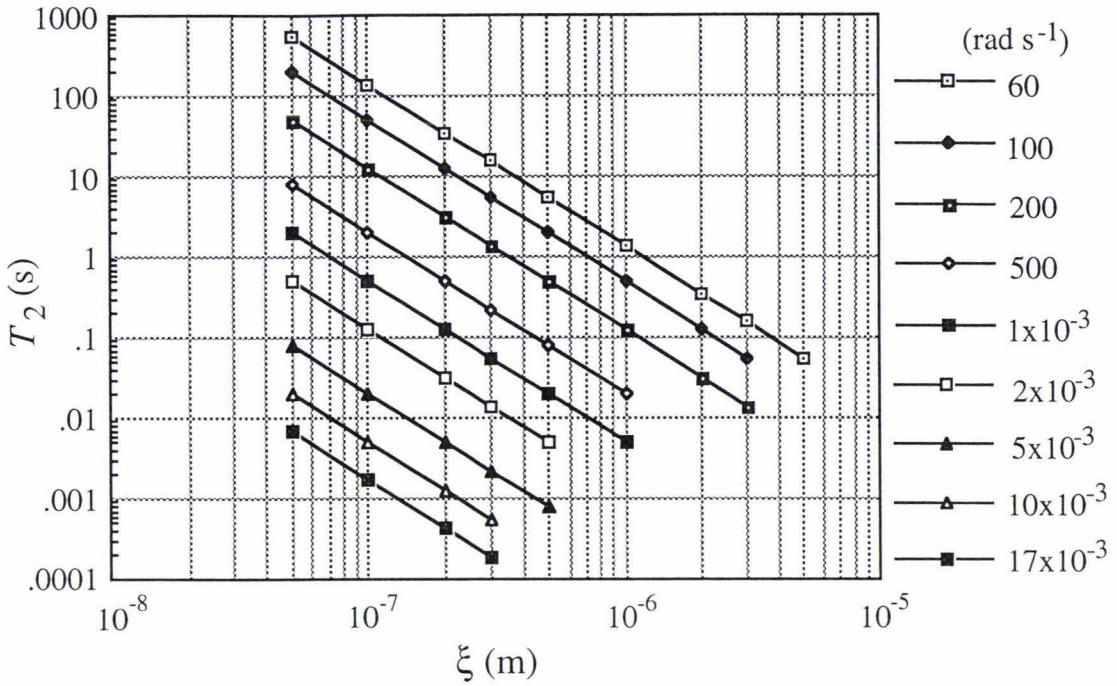

Figure 3.4. Plot of dependence of T_2 relaxation time on correlation length ξ (characteristic length scale for system heterogeneity) for a range of $(\overline{\Delta\omega_0^2})^{1/2}$ values due to susceptibility inhomogeneity. Only fast exchange conditions are considered here, meaning that $\overline{\Delta\omega_0^2}\,\tau_c^2 \leq 0.1$ at the least. The T_2 relaxation rate becomes faster as $(\overline{\Delta\omega_0^2})^{1/2}$ increases and, following each curve, as ξ gets larger until the point where fast exchange can no longer be applied. Above this point slow exchange behaviour begins to take over and the relaxation becomes weaker as ξ increases. For a typical biological system the extra relaxation (from this susceptibility inhomogeneity) will only become significant if it is on the order of 20 ms or less.

While the parameter of importance for displacement was the magnetic field offset $\Delta B_0(\mathbf{r})$, it is instead the local susceptibility-induced gradient $\nabla(\Delta B_0(\mathbf{r}))$, or $\mathbf{G}^{loc}(\mathbf{r})$, which determines the size of the diffusive attenuation effect. $\mathbf{G}^{loc}(\mathbf{r})$ must be superposed onto the combined imaging gradients $\mathbf{G}$

$$\mathbf{G}^{tot}(\mathbf{r}) = \mathbf{G} + \mathbf{G}^{loc}(\mathbf{r}). \tag{3.15}$$

In this way, the attenuation factor previously derived for the frequency encoding direction will become $\exp(-\frac{1}{12}\gamma^2 G_x^{tot}(\mathbf{r})^2 D(NT)^3)$ or $\exp(-\frac{4}{3}\pi^2 k_x^{tot}(\mathbf{r})^2 DNT)$ and dependent on position, where $k_x^{tot}(\mathbf{r}) = k_x^{max} + (2\pi)^{-1}\gamma G_x^{loc}(\mathbf{r})$. $G_x^{loc}(\mathbf{r})$ may be positive or negative, adding to or subtracting from the read gradient, so it is likely that in an image some areas will be darker and some brighter than the homogeneous identical case. If the local gradients are large enough to rival the read gradient, attenuation in that direction may be eliminated altogether in special sites, leading to exceptionally bright spots if significant attenuation prevails in other areas. While these gradient null points

might be expected to be sharp and point-like, the other light and dark regions will be less focused, more gradual. In images exhibiting both displacement and attenuation phenomena, it must be remembered that the signal loss suffered by an element will depend on its actual physical position in the object. However the attenuated element will most often appear in a different location in the image, and may be concentrated or 'focused' with other elements which have been displaced to the same location.

The phase encoding direction will also experience nulls, but these are distributed in **k**-space and will not by nature cause bright spots. The analysis has been detailed in a recent paper*(108)*, giving the complete point spread function for our y-direction

$$\mathrm{PSF}(y') = \left(\frac{3}{16\pi Dt_y}\right)^{3/2} \exp\left(-\frac{3y'^2}{16Dt_y}\right) \exp\left(-i\gamma\left(\frac{11}{8}\right)G_y^{\mathrm{loc}}(\mathbf{r})y't_y\right) \times \exp\left(-\frac{7}{48}\gamma^2 G_y^{\mathrm{loc}}(\mathbf{r})^2 Dt_y^3\right) \qquad (3.16)$$

where y' is the point displacement from the unsmoothed original, and t_y can again be approximated as $\frac{1}{2}NT$. Once more phase shifts due to precession induced by the local field are not applicable to the spin echo scheme used here. The elements are smoothed by a gaussian of width $(2Dt_y)^{1/2}$, or Δx_{diff}, in this sense the diffusion distance during the phase encoding gradient. The gaussian is modulated by a phase roll or oscillation, capable of producing cancellation of intensity by interference for significant oscillation over at least adjacent pixels. There is an additional weak attenuation factor $\exp\left(-\frac{7}{48}\gamma^2 G_y^{\mathrm{loc}}(\mathbf{r})^2 Dt_y^3\right)$ which will only become important for long t_y. Thus where the phase gradient caused smoothing without attenuation in homogeneous environments, diffusion over a few pixels in time t_y in local field gradients may produce observable signal loss. The strong dependence on t_y means that it may be eliminated again with sufficiently large gradients to allow short t_y.

The total expression is *(108)*

$$A_{\mathrm{pf}}(0,k_y) = \left(\frac{3}{32\pi DNT}\right)^{3/2} \exp\left(-\frac{3y'^2}{32DNT}\right) \exp\left(-i\gamma\left(\frac{11}{16}\right)G_y^{\mathrm{loc}}(x,y)y'NT\right) \times \exp\left(-\frac{7}{384}\gamma^2 G_y^{\mathrm{loc}}(x,y)^2 D(NT)^3\right) \exp\left(-\frac{1}{12}\gamma^2 G_x^{\mathrm{tot}}(x,y)^2 D(NT)^3\right). \qquad (3.17)$$

Using the same example as before, simulation of a more complete picture in the real NMR micrograph may be achieved comprising both distortion and diffusion phenomena. Fig 3.5 shows the maps of $G_x^{\mathrm{loc}}(x,y)$ and $G_y^{\mathrm{loc}}(x,y)$, containing six lobes rather than the

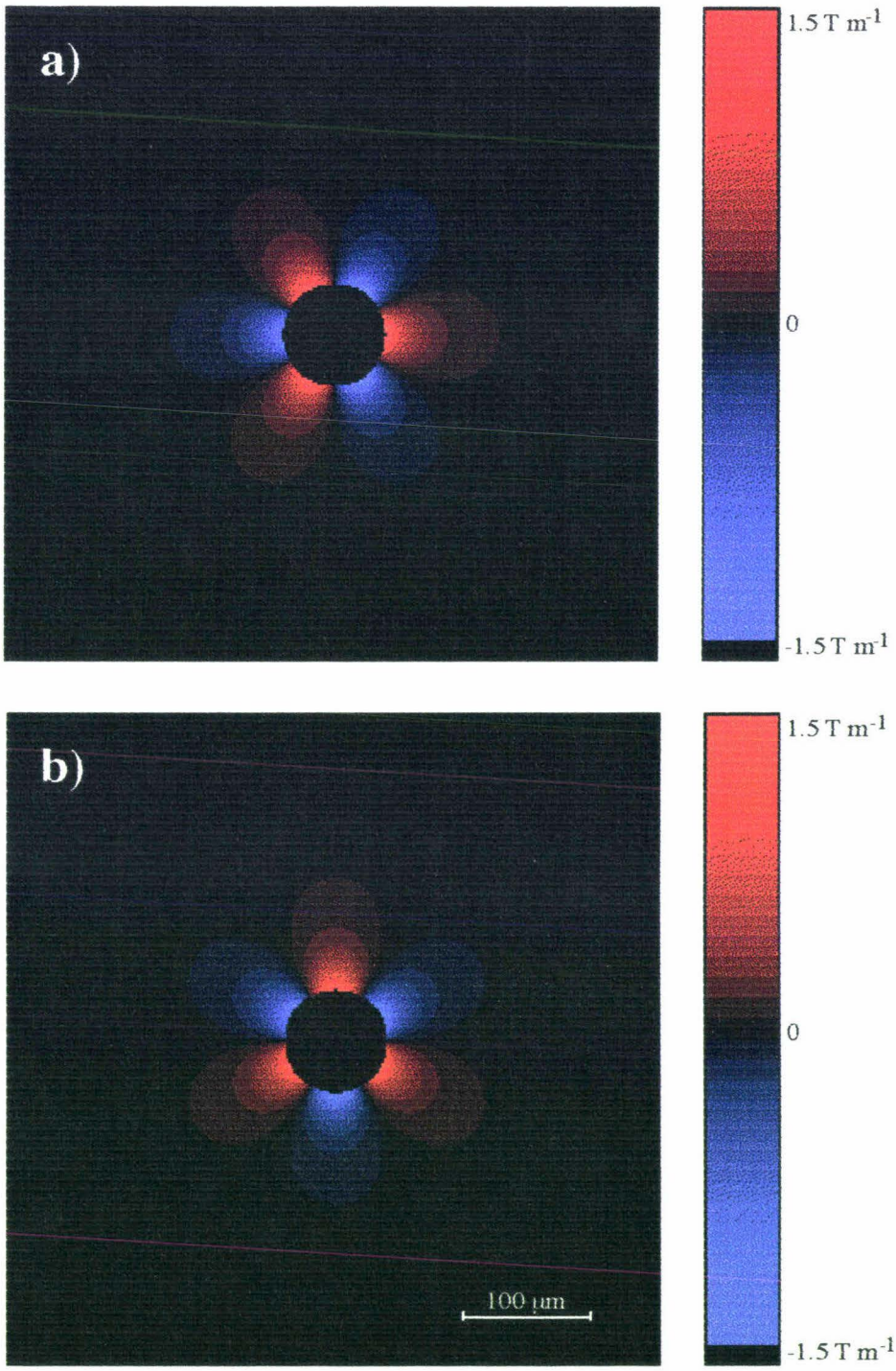

Figure 3.5. Magnetic gradient offsets (a) ΔG_x^{loc} and (b) ΔG_y^{loc} around a cylinder with susceptibility mismatch and applied $\mathbf{B}_0$ as in Fig. 3.2. Again both positive and negative offsets are present, and these will add to and subtract from the read gradient respectively. Parameters: $B_0 = 7$ T, $\Delta\chi_m = 9 \times 10^{-6}$, $\Delta x = 2$ µm, $N = 256$.

four in $\Delta B_0(x,y)$. Negative lobes of $G_x^{loc}(x,y)$ will cancel the read gradient, lessening attenuation in those areas, while positive components will lead to even darker regions, as can be observed in Fig 3.6a. It is interesting to note that the read gradient attenuation map

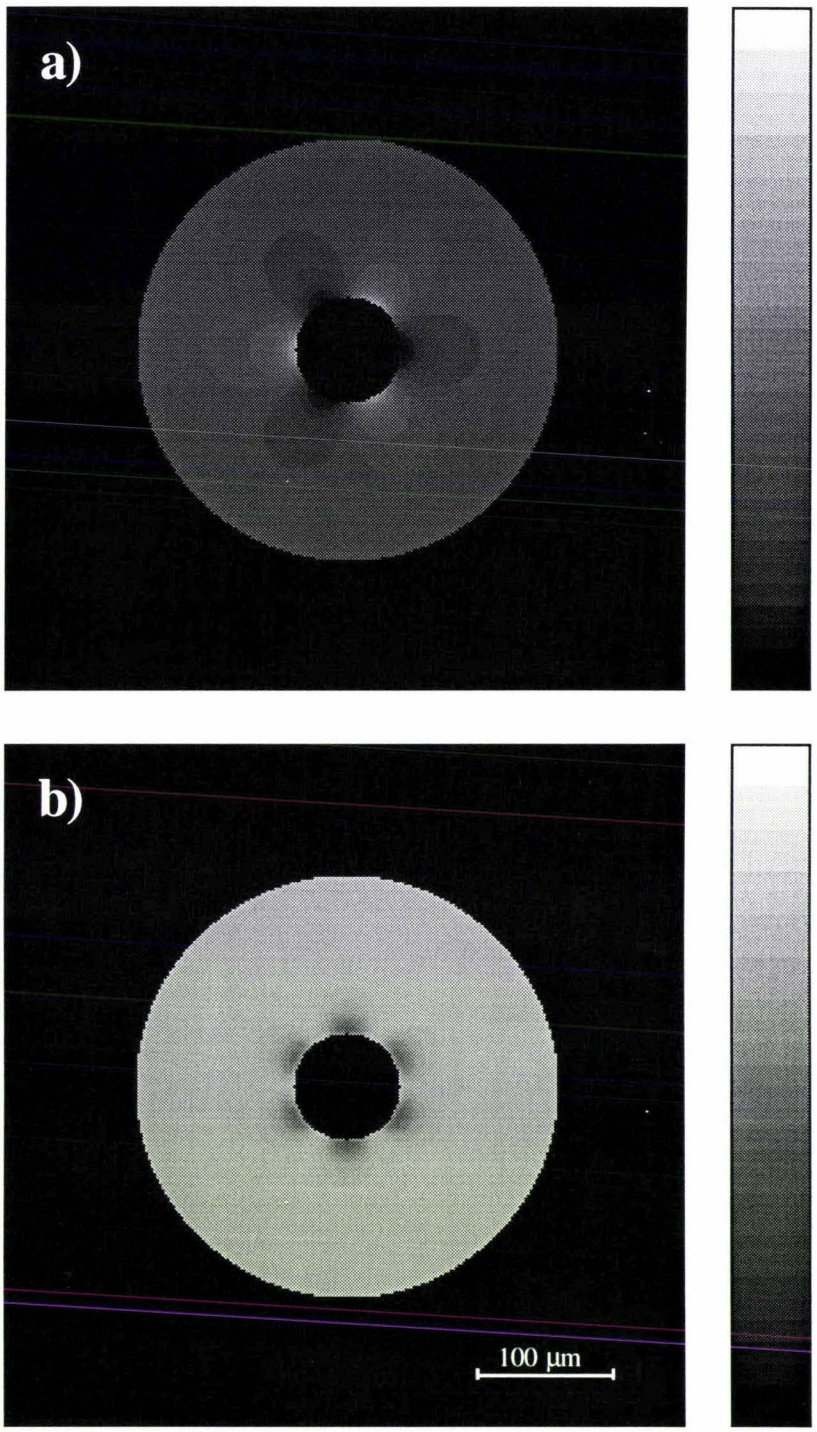

Figure 3.6. Computer-simulated images showing the coupled distortion and diffusive attenuation caused by susceptibility inhomogeneity. (a) Attenuation due to the sum of the gradients in the x-direction, including the read gradient. (b) Attenuation due to the y-component gradients, which when added to (a) gives the total pre-displacement attenuation, in (c). The read gradient has, in general, a more significant effect on image intensity than local gradient offsets. (d) Final image showing arrowhead distortion enhanced by dark regions. Parameters: B_0 = 7T, $\Delta\chi_m = 9 \times 10^{-6}$, $D = 2.5 \times 10^{-9}$ m^2 s^{-1}, bandwidth = 60 kHz, Δx = 2 μm, N = 256.

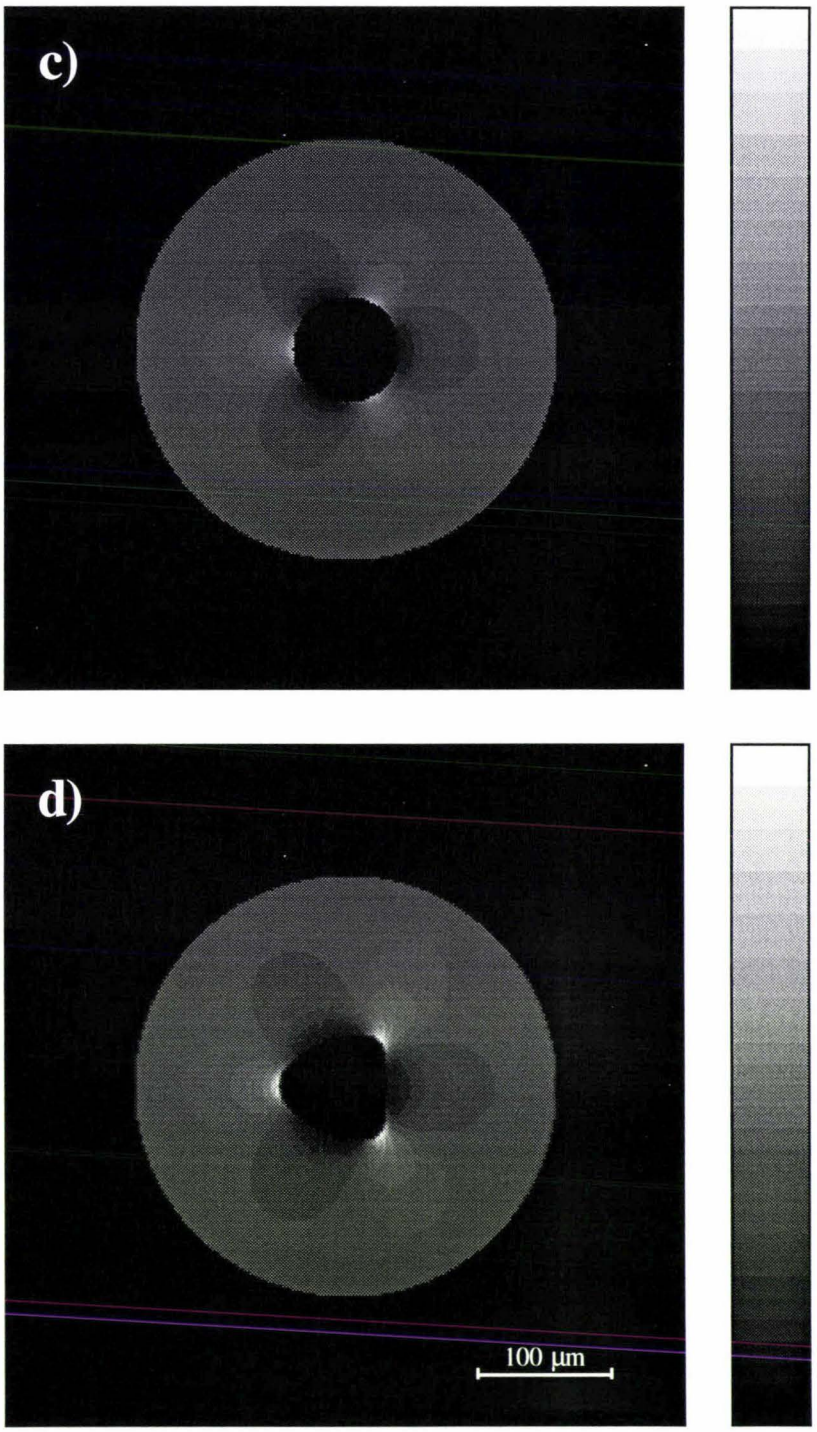

Figure 3.6 (c), (d)

is reminiscent of the arrowhead configuration for the displacement map, and moreover the arrow is in the same sense, giving reinforcement of positional concentration. The very weak phase attenuation map in Fig 3.6b mirrors $G_y^{loc}(x,y)$, not surprisingly, and again there are faint bright regions in the same locations as the arrow-points, preserving those features. This effect will be more marked if a smaller bandwidth is used, lengthening t_y. The attenuation map for both directions (at once) is displayed in Fig 3.6c, and the subsequent displaced image in Fig 3.6d. In comparison with the simple displaced image

in Fig 3.3, the arrowhead has become much more prominent, and may be used as a signature for simple cylindrical or spherical components occurring in real-life samples. Investigation of the adherence of experiments to the theory while varying parameters such as the bandwidth (and echo time) and the self-diffusion coefficient is covered in Chapter 4.

Turning our attention back to the second case of non-uniform self-diffusion coefficient *D (115-118)*, spins travelling through a uniform gradient but confined in motion by some restriction will again sample the range of Larmor frequencies $(\overline{\Delta\omega_0^2})^{1/2}$. One might think for example of a boundary layer of fluid next to a restriction which has a lower effective diffusion coefficient than the bulk fluid distant from the restriction. The two populations might have different relaxation rates due to the effects of diffusion in the gradient, and there will be exchange between these groups. Quantitatively the relevant factor may be extracted from the previous expression for attenuation in 'homogeneous' environments. Remembering that attenuation encountered in the phase encoding direction was shown to be unimportant in this case, the remaining term is $\exp(-\frac{1}{12}\gamma^2 G_x^2 D(NT)^3)$. Rewritten as $\exp(-\frac{1}{3}\pi^2 G_x^2 DNT/\Delta x_{\text{pixel}}2)$, the dependence of the attenuation on pixel size and the number of pixels N is noticeable. Thus reduction of the pixel dimension gives not only a loss of signal-to-noise ratio due to diminishing voxel size, but also a deepening of attenuation effects. Possibilities of diffusion coefficient heterogeneity include the presence of more than one species of molecule, and local boundaries which restrict diffusion in a certain direction. It should be noted that only inhibition of diffusion in the read direction, as is caused by walls perpendicular to that direction, will be applicable here.

3.5 Reduction of Diffusive Attenuation By CPMG Methods

Under slow exchange the factor for attenuation $\exp(-\frac{2}{3}\gamma^2 G^2 D t^3)$ may be further weakened by lessening the effective echo time $2t$. If a general period of evolution τ giving an attenuation factor A_f of $\exp(-\frac{1}{3}\gamma^2 G^2 D\tau^3)$ is bisected by a 180° refocusing rf pulse, there will be two consecutive periods of evolution both resulting in $\exp(-\frac{1}{3}\gamma^2 G^2 D(\frac{\tau}{2})^3)$ and giving the combined outcome of $\exp(-\frac{1}{3}\gamma^2 G^2 D2(\frac{\tau}{2})^3)$. Similarly if the period is trisected the outcome will be $\exp(-\frac{1}{3}\gamma^2 G^2 D3(\frac{\tau}{3})^3)$. By inspection the general

case of n 180° refocusing pulses at equal intervals during time τ will give $\exp(-\frac{1}{3}\gamma^2G^2D(n+1)(\frac{\tau}{n+1})^3)$, or in a form reminiscent of conventional relaxation $\exp(-\frac{1}{3}\gamma^2G^2D(\frac{\tau}{n+1})^2\tau)$, which is a weaker attenuation than the original $\exp(-\frac{1}{3}\gamma^2G^2D\tau^3)$ if $n \geq 1$. Unfortunately these CPMG methods (introduced in Section 2.9) cannot easily help the case of the minimum echo time pulse sequence as there is no period without a vital function in the imaging process.

Chapter 4
Experiments With Model Systems

4.1 The Model System

Now we are ready to compare our theory of susceptibility inhomogeneity artefacts with real experiments. A suitable model system for investigating the special case of cylinder geometry, discussed at length in Section 3.2, is shown in Fig 4.1. A small glass rod of diameter 0.35 mm is placed inside a small glass capillary filled with liquid, of inner diameter 1.6 mm. A diamagnetic susceptibility mismatch comparable to water versus air ($\chi_{m2} - \chi_{m1} = 9 \times 10^{-6}$) is not entirely ideal for illustration of the concepts because it is instructive to be able to increase the acquisition bandwidth to the point where the artefacts are overwhelmed, and the imaging gradients needed to achieve this (3.3 T m^{-1}) are not available in the Bruker microimaging probe used in this work. Thus the less severe discontinuity of a liquid vs solid phase was chosen, corresponding to the more manageable range of $\Delta\chi_m < 1 \times 10^{-6}$. Glass is a good candidate for the solid interior, because it yields no NMR signal and so does not mask distortion of the medium outside the rod. The size of the model also has to be small enough to exhibit diffusion effects in extreme conditions, although the construction becomes more difficult as the sample gets smaller.

A Bruker AMX 300 MHz imaging system (B_0 of 7.05 T) with a wide bore superconducting magnet was used for all experiments. In Section 3.2 it was shown that transverse orientation of the radio frequency receiver coil is necessary to observe susceptibility artefacts for cylinders, so naturally a solenoidal coil was used (fortunately solenoidal coils usually give the best rf field homogeneity) with only a 3 mm diameter because optimal signal-to-noise ratio is attained with minimum size. The z-direction is taken to be the long axis of the rod/tube, with read and phase directions of x and y respectively as mentioned earlier. $\mathbf{B}_0$ acts along the y-axis.

4.2 Determination of $\Delta\chi_m$

Since glass is manufactured in a wide range of properties, we cannot simply find the correct $\Delta\chi_m$ in the tables and must determine it directly from comparison of experiments with simulations. Logically it will be more evident if pixel shifts are the only phenomena observed, in the effective absence of self-diffusion effects. To achieve this in practice a 10% polyethylene oxide (PEO) polymer and water solution is used for the

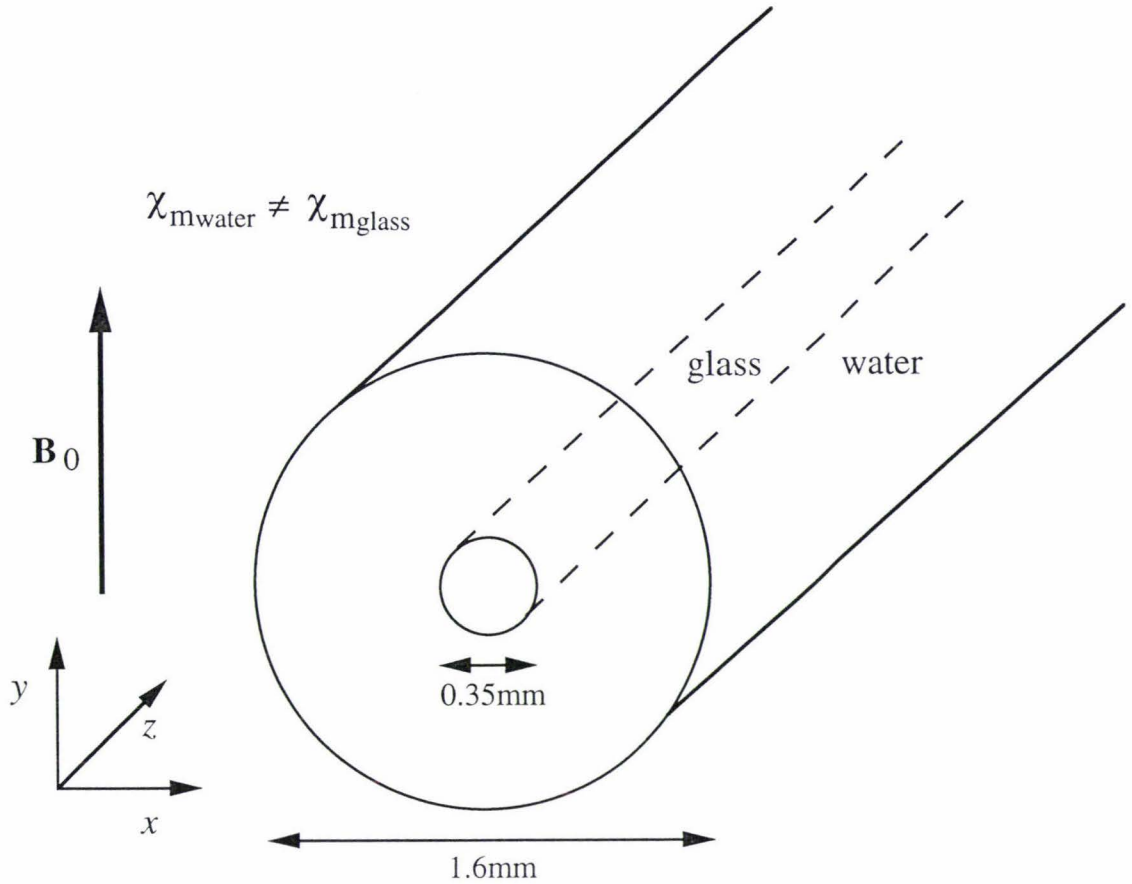

Figure 4.1. Schematic diagram of the sample geometry and orientation used in experiments in Chapter 4.

liquid medium around the rod, and the polymer protons (rather than the water protons) are selectively imaged by chemical selection because at this concentration the self-diffusion of WSR301 PEO is approximately 5 orders of magnitude slower than water. However the bulk diamagnetic susceptibility is still dominated by the 90% water and is negligibly different from that of water.

A series of 128^2 images obtained using the standard spin warp sequence shown in Fig 2.3, with successively decreasing acquisition bandwidths and a field of view of 2.5 mm, is depicted in Fig 4.2. The improvement of signal-to-noise ratio as the bandwidth is reduced is plainly obvious in the images. The shapes of the features are as predicted in Section 3.2, with a flattening of the right edge of the glass rod and a pointed edge at the left at moderate bandwidth (5 kHz), transforming into a completely distorted arrowhead or 'side-on smile' shape with prominent bright spots at the lowest bandwidth (1 kHz). As desired it is possible to obtain a nearly undistorted image at 20 kHz, or more certainly at 40 kHz, where the signal-to-noise ratio is still favourable. The degree of

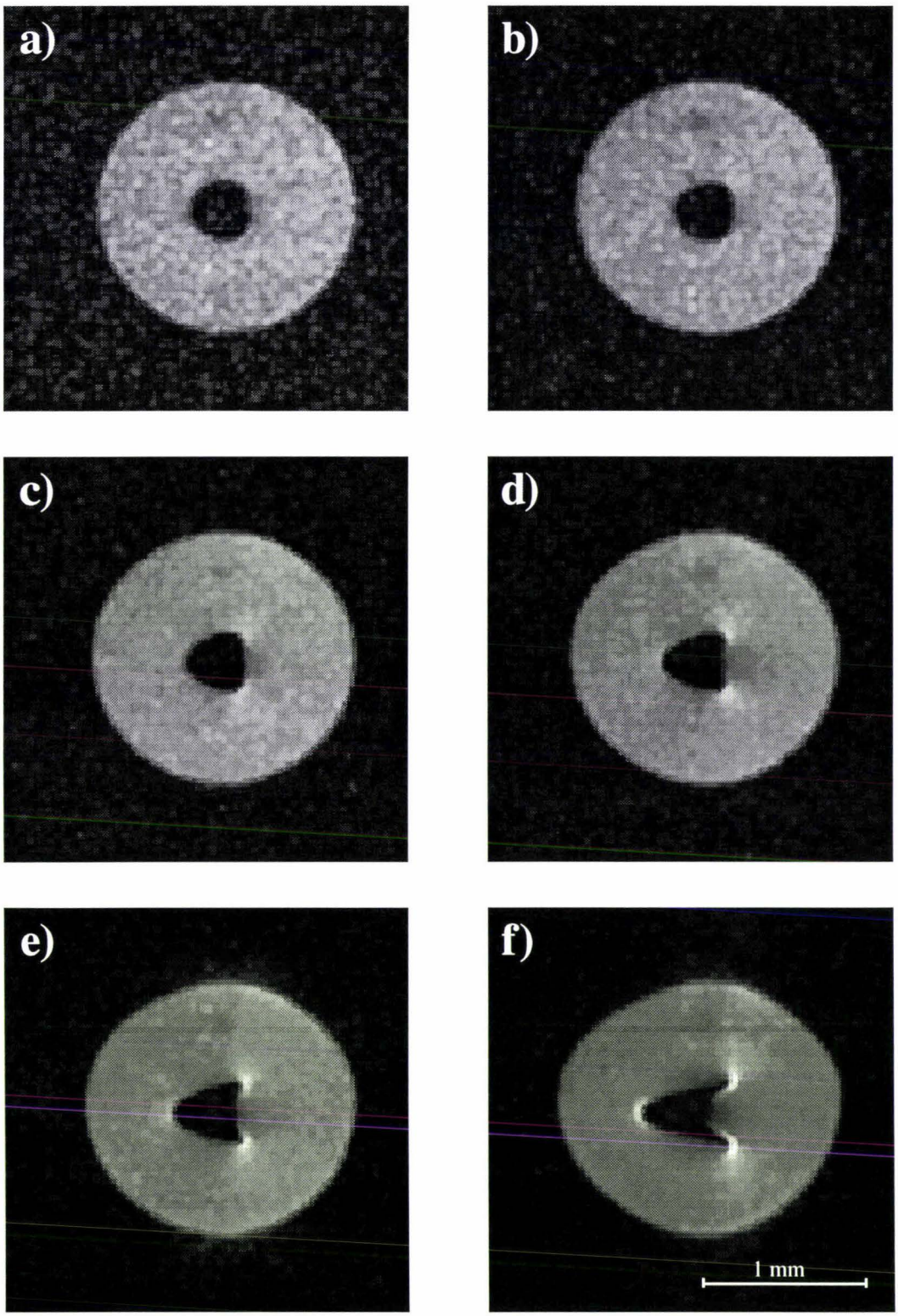

Figure 4.2. A series of spin echo images of the sample shown in Fig. 4.1 with 10% polyethylene oxide solution replacing the water. The PEO molecules possess a very small self-diffusion constant D and so have been selectively imaged to remove diffusive attenuation effects. The bandwidths used were (a) 20 kHz, (b) 10 kHz, (c) 5 kHz, (d) 3 kHz, (e) 2 kHz and (f) 1 kHz. The images become more distorted as the read gradient is reduced in size relative to the local field offsets. $\Delta\chi_m$ is approximately 0.7 x 10^{-6}. Parameters: pulse sequence - chemical shift selective spin echo, B_0 = 7 T, Δx = 19 μm, N = 128, number of acquisitions (n_{acq}) = 32, slice thickness = 300 μm, T_R = 2 s.

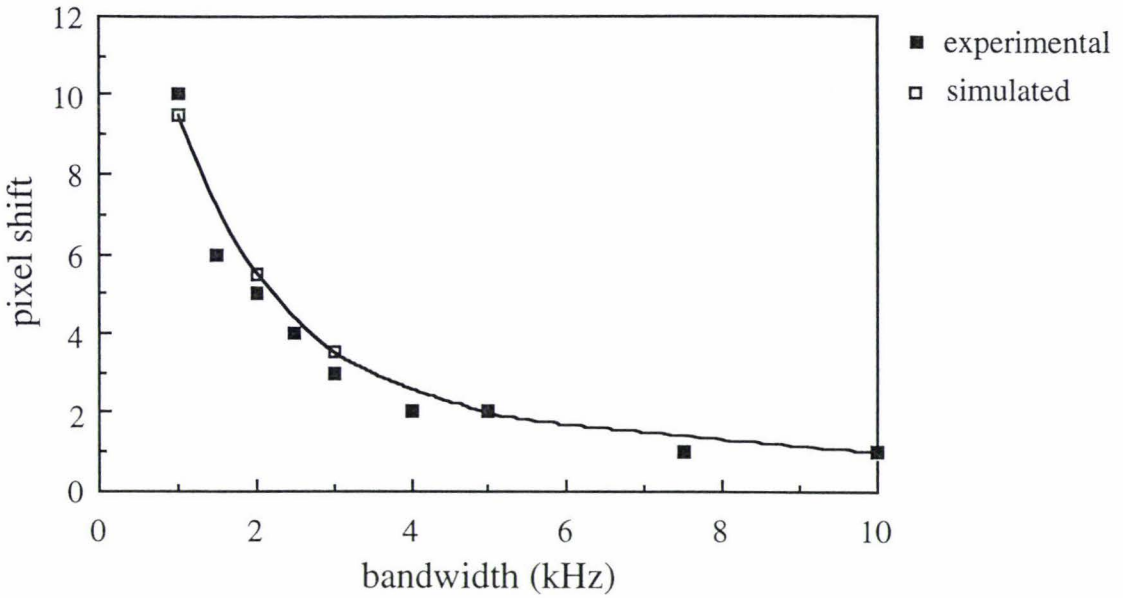

Figure 4.3. Plot of the distance shifted (in pixels) by the vertex of the arrowhead characteristic to susceptibility distortion (seen in Fig. 4.2) at a range of acquisition bandwidths. A simulation using a susceptibility difference $\Delta\chi_m$ of 0.7 x 10^{-6} was found to match the experimental data best, to an uncertainty of $\pm 0.2 \times 10^{-6}$.

distortion is measured by the position of the right edge of the arrow-point, relative to the position of the original edge of the glass rod in a high bandwidth (20 kHz) image. Fig 4.3 shows the plot of this pixel shift against bandwidth.

When we inspect the 1 kHz case more closely the inner wall of the tube also appears to be distorted, because the field disturbance induced by the glass cylinder is becoming so significant in comparison to the applied gradient that lobes reach right to the tube walls. It is not possible that the tube walls themselves are causing the distortion because the field inside a cylinder is uniform, hence susceptibility effects caused by the tube are only outside it where there is no signal.

Simulations were run using a range of $\Delta\chi_m$ values and a low bandwidth of 1 kHz (the most extreme case of distortion will give maximum sensitivity to susceptibility mismatch) to gain an approximation of the true $\Delta\chi_m$. $\Delta\chi_m$ was found to be 0.7 ppm with an uncertainty in the region of 0.02 ppm. Using this a whole series of 256^2 images was calculated by simulation, shown in Fig 4.4. Obviously there is no varying signal-to-noise ratio or even noise at all, but the shapes displayed compare very well to their experimental counterparts. A plot of (pixel shifts)/2 equivalent to the earlier plot demonstrates that the simulation holds fairly well for all the bandwidths (Fig 4.3), not differing by more than half of a pixel (except for the 1.5 kHz bandwidth) and confirming

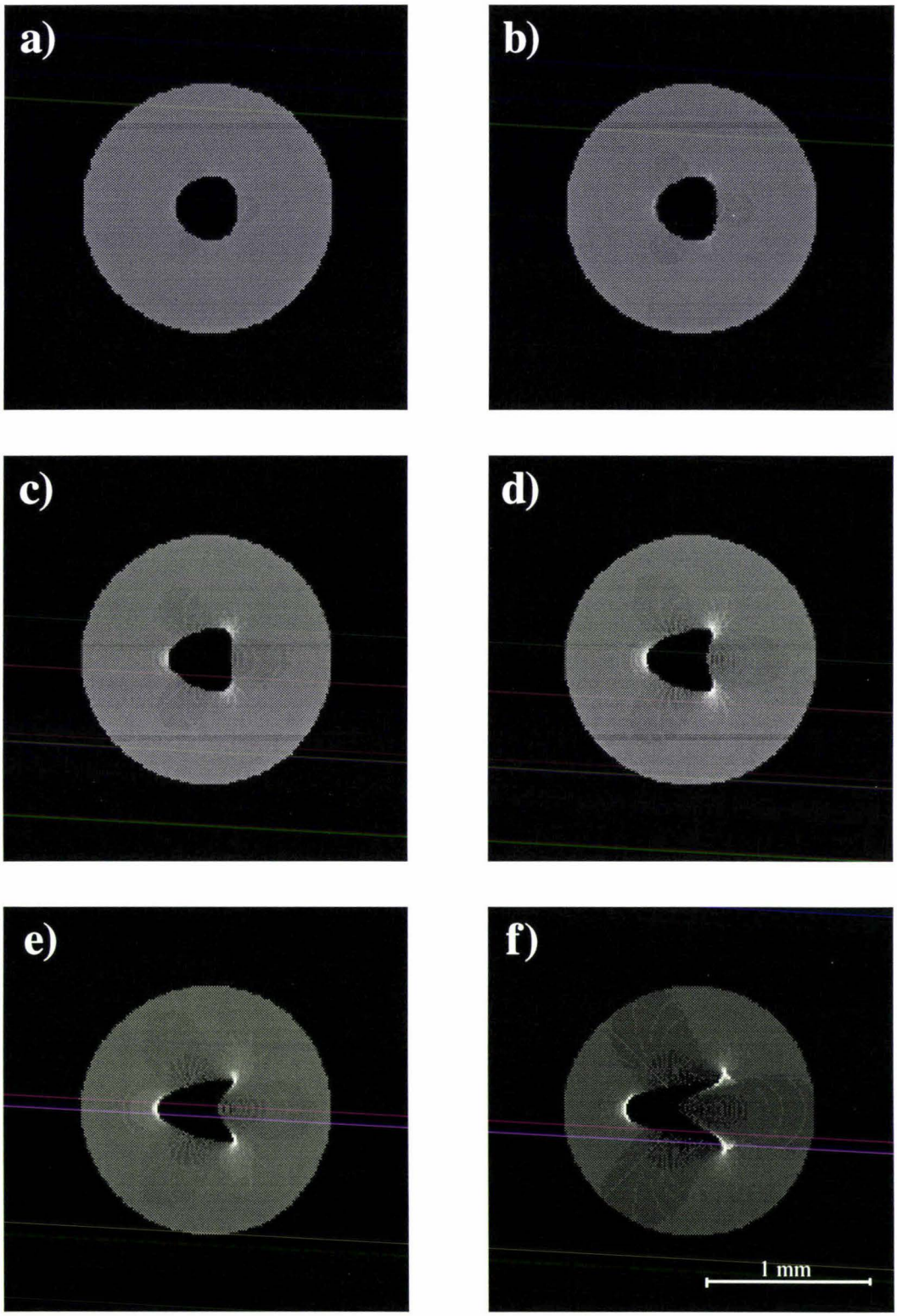

Figure 4.4. Computer-simulated images calculated using the conditions of the experiment shown in Fig. 4.2. Again the bandwidths correspond to (a) 20 kHz, (b) 10 kHz, (c) 5 kHz, (d) 3 kHz, (e) 2 kHz and (f) 1 kHz. The self-diffusion coefficient D is taken to be effectively 0. Lines seen in some of the images are an artefact of the simulation procedure. Parameters: $B_0 = 7$ T, $\Delta\chi_m = 0.7 \times 10^{-6}$, $\Delta x = 9.7$ μm, $N = 256$.

the accuracy of the susceptibility mismatch estimate between the glass and the surrounding solution. The appearance in the images of stripes or corrugations is due to the limitations of the interpolation procedure, mentioned in Chapter 3, and should not cause concern although they could possibly be eliminated with further modifications to the simulation programme (regarding the interpolation) if it were appropriate. It is impossible to discern in the experimental images the fine structure displayed in the arrowhead vertices of the 1 kHz simulation, as the resolution is not sufficient even though 20 accumulations were used for signal averaging.

4.3 Combined Displacement and Attenuation Effects

A second sample was constructed without polymer for the inclusion of diffusion effects into the experiments. The same series of acquisition bandwidths was used to gain the succession of 128^2 images in Fig 4.5. Unfortunately the absolute image intensities cannot be taken as directly comparable with eachother, because there is a gain dependence on bandwidth which precludes matching of images by the level of background noise, but the relative intensities of the regions should still be be correct.

For this range of bandwidths the read gradient sizes G_x, given by $\frac{2\pi\Delta f}{\gamma N \Delta x}$, vary from 0.189 T m^{-1} to 0.009 T m^{-1}. The diffusive attenuation factor A_f for the read direction was given as $\exp(-\frac{1}{12}\gamma^2 G_x^{tot}(x,y)^2 D(NT)^3)$, but ignoring G_x^{loc} and taking D to be typically 2.5 x 10^{-9} m^2 s^{-1} A_f varies from 0.87 to 0.08 over these bandwidths. Therefore there will be easily observable darkening of the image, as is apparent in the images. For example, it is easier to judge with the eye the moderate attenuation in the 3 kHz image which should be in the vicinity of 0.39. G_x^{loc} is on the order of $\Delta\chi_m B_0/a$ or less, at a maximum close to the rod, and this corresponds to 0.028 T m^{-1}. This value is intermediate in the range of G_x values and so should be capable of producing gradient null points which can show up as bright spots, though not necessarily in the place of origin after distortion. In fact, these spots are the only significant feature to survive attenuation for the 1 kHz image. As G_x becomes smaller, the actual null points will move further from the rod in the x direction, and will be 'focused' further still by the displacement process. The effect of G_y^{loc} is more subtle, and we will leave this consideration to the simulation where it may be dealt with completely. It is interesting to note that the wall of the tube on the left and right is slightly enhanced in the 1 kHz image, indicating restriction of diffusion by the boundary. This phenomenon will be investigated with more suitable conditions in Section 4.4.

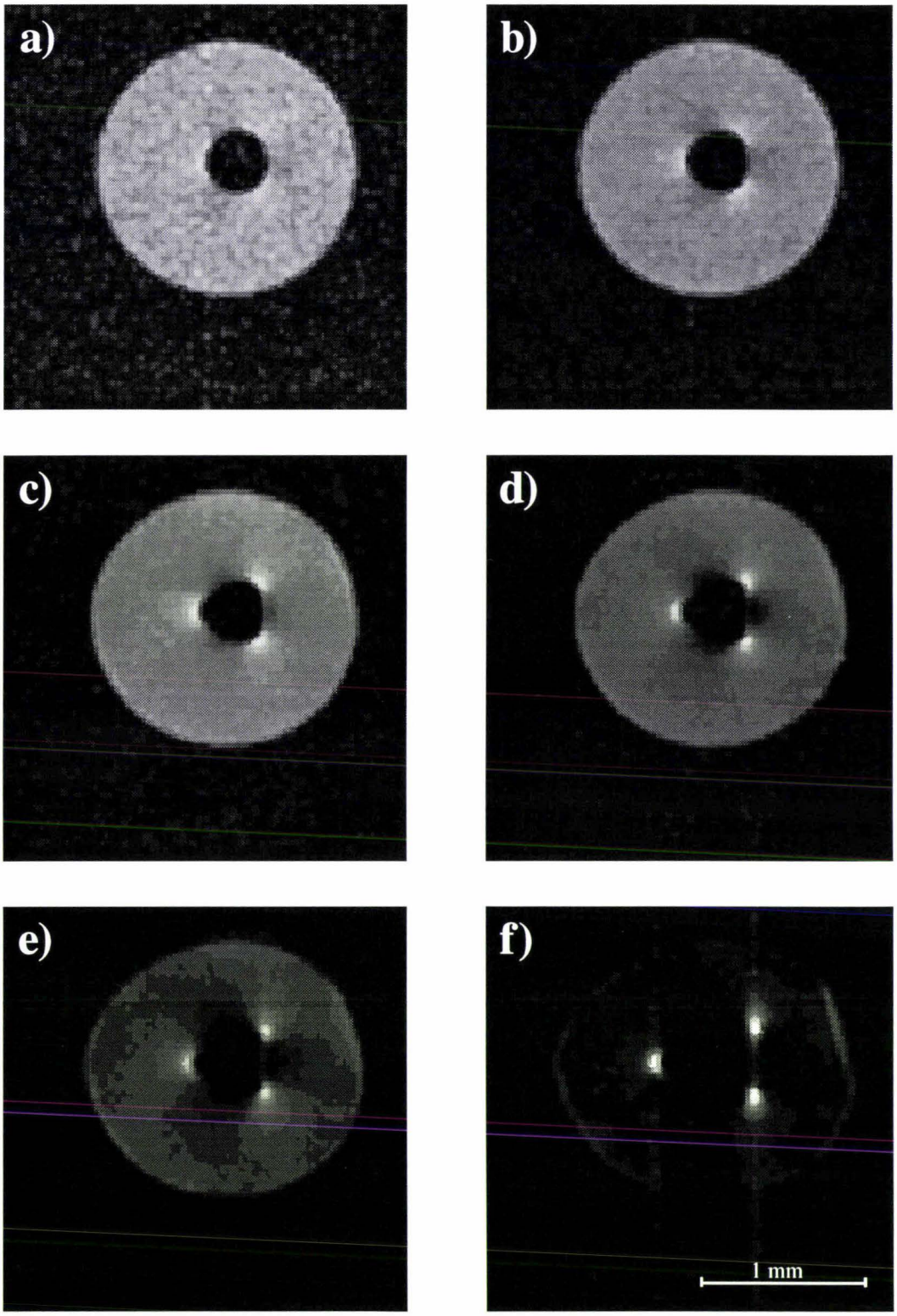

Figure 4.5. A series of spin echo images under the same conditions and acquisition bandwidth sequence as Fig 4.2, except that the sample contains only water and no polyethylene oxide. It is evident that diffusive attenuation (like distortion) deepens as the bandwidth is reduced, mainly because of longer echo times. Bandwidths used were (a) 20 kHz, (b) 10 kHz, (c) 5 kHz, (d) 3 kHz, (e) 2 kHz and (f) 1 kHz giving echo times T_E of 17, 23, 36, 53, 74 and 138 ms respectively. $\Delta\chi_m$ is still approximately 0.7×10^{-6} as the solution is 90% water. Parameters: pulse sequence - spin echo, B_0 = 7 T, Δx = 19 μm, N = 128, n_{acq} = 32, slice thickness = 300 μm, T_R = 2 s.

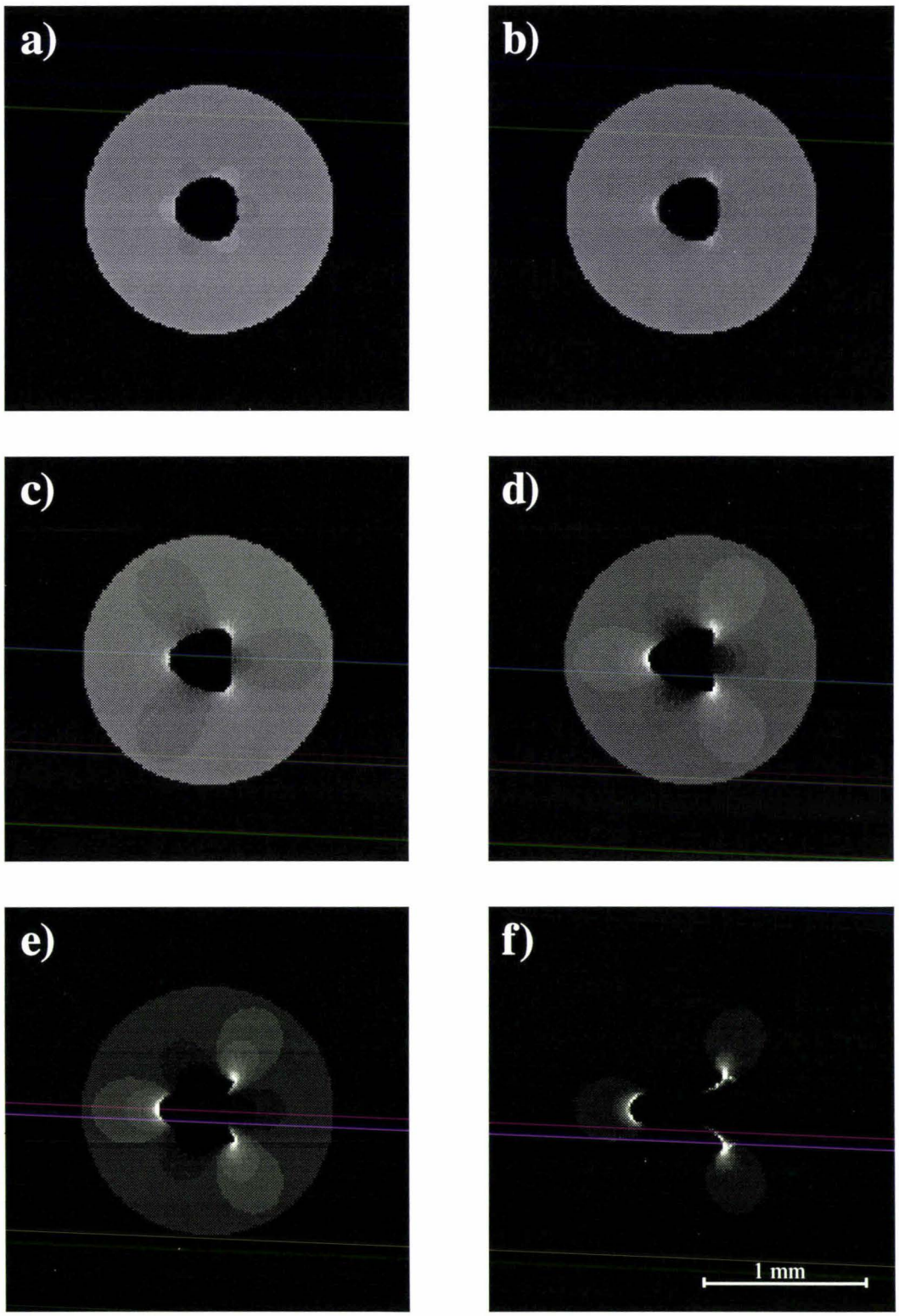

Figure 4.6. Computer-simulated images calculated using the conditions of the experiment shown in Fig. 4.5. Again the bandwidths correspond to (a) 20 kHz, (b) 10 kHz, (c) 5 kHz, (d) 3 kHz, (e) 2 kHz and (f) 1 kHz. Note that the attenuation is calculated as though the pixel size Δx is 19 μm as in the real experiment. Absolute image intensities are not directly comparable with those in Fig. 4.5 because of the bandwidth dependence of the noise level in the experiments. Parameters: $B_0 = 7$ T, $\Delta\chi_m = 0.7 \times 10^{-6}$, $D = 2.5 \times 10^{-9}$ m^2 s^{-1}, $\Delta x = 9.7$ μm, $N = 256$.

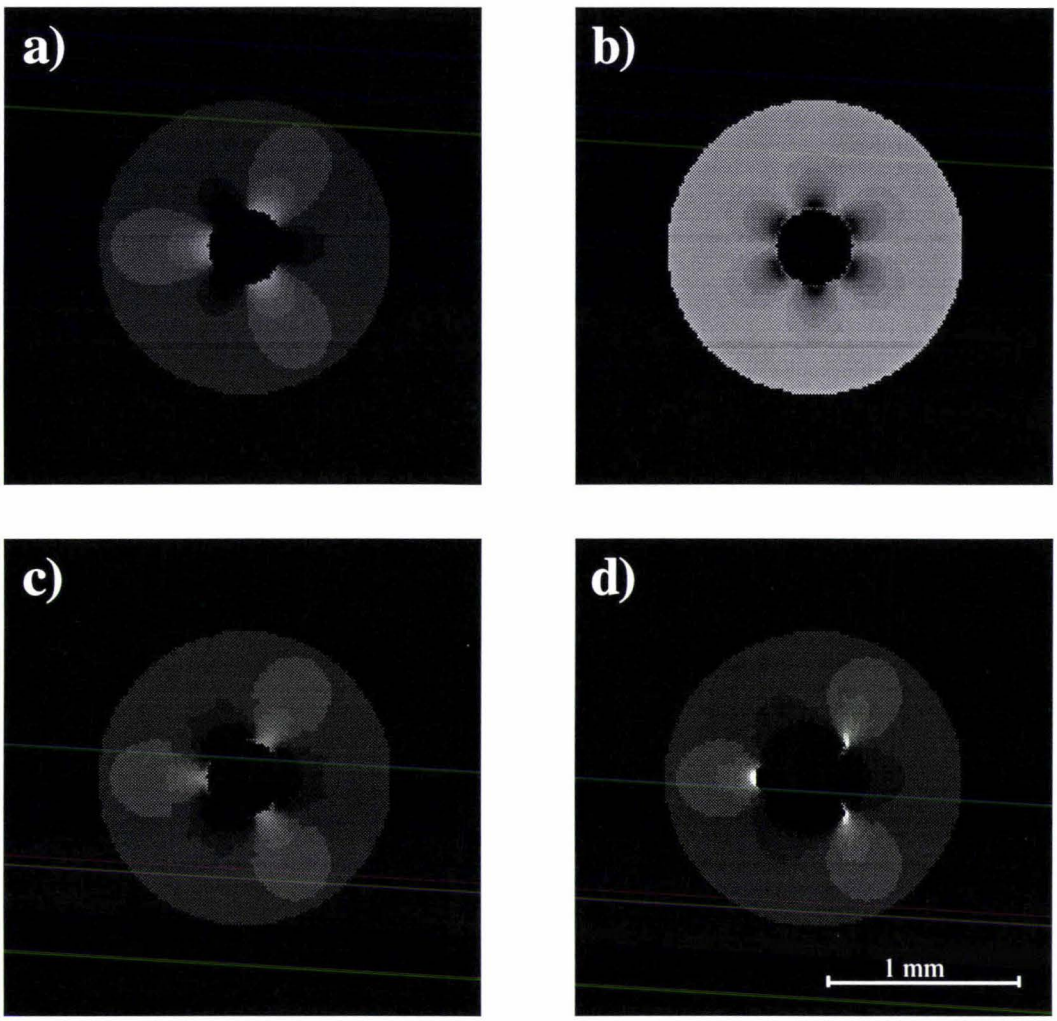

Figure 4.7. Computer-simulated images showing the role of diffusive attenuation due to the *y*-component local gradients. (a) Attenuation due to the sum of the gradients in the *x*-direction, including the read gradient. (b) Attenuation due to the *y*-component gradients, which when added to (a) gives the total pre-displacement attenuation, in (c). (d) Final image showing arrowhead distortion modulated by dark regions. (a) - (d) correspond to a bandwidth of 2 kHz while (e) - (h) show the same series of images for 1 kHz. The final images are not significantly altered from their equivalents in Fig. 4.8, meaning that *y*-component local gradients may be neglected in our attenuation simulations. Again the attenuation is calculated as though the pixel size Δx is 19 μm as in the real experiment. Parameters: B_0 = 7 T, $\Delta\chi_m = 0.7 \times 10^{-6}$, $D = 2.5 \times 10^{-9}$ m^2 s^{-1}, Δx = 9.7 μm, N = 256.

Fig 4.6 shows the equivalent set of simulated images incorporating diffusive terms. The triangular array of bright spots or regions do not appear until a smaller bandwidth than for the real case, and are more sharply-defined. The occurrence of restricted diffusion at the walls of the glass cylinder may contribute the extra signal in our sample which is then refocused into the bright vertices, but it is not easy to confirm this. The effects of diffusion for the phase direction are demonstrated in Fig 4.7, where the pre-displacement attenuation is depicted for the *x*- and *y*-directions separately in the 2 and 1 kHz bandwidth (worst case) examples. As was found in Section 3.4 the position of

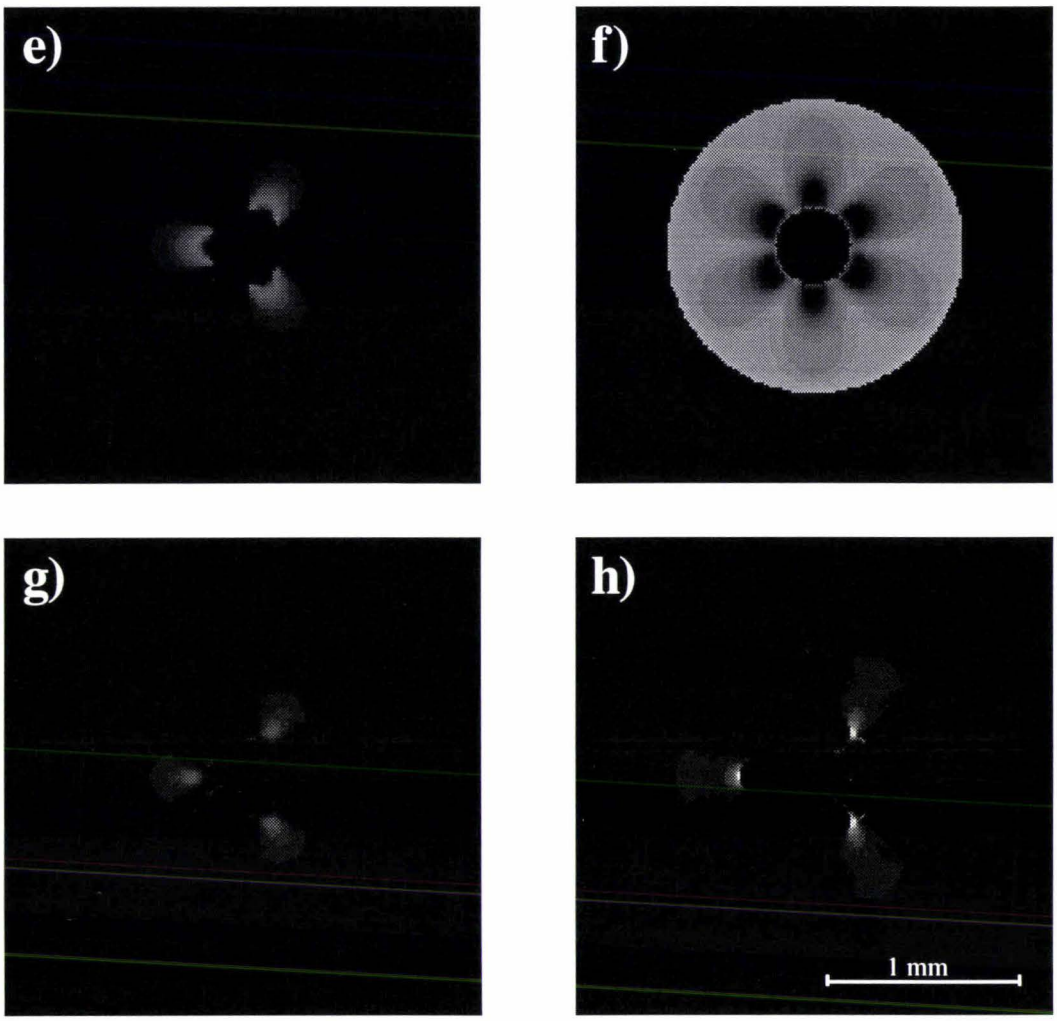

Fig 4.7 (e), (f), (g), (h)

intense lobes for the *y*-components largely coincides with the regions contributing to the triangle of spots, and it can be seen that when the two effects are combined, and transformed by the appropriate displacement, there is little change to the outcome compared with that arising purely from the read gradient. Careful inspection shows only that the bright spots are somewhat diminished.

4.4 Restricted Diffusion at Impermeable Boundaries

To effectively illustrate bounded diffusion the susceptibility aspects are momentarily put aside, and to this purpose an identical tube was imaged with no susceptibility disturbance, i.e. a tube containing only water. Since the relevant attenuation factor is $\exp(-\frac{1}{3}\pi^2 G_x^2 DNT/\Delta x_{\text{pixel}}^2)$, reduction of the pixel dimension will dramatically enhance the attenuation and so also any contrast afforded by inhomogeneous self-diffusion. At half the pixel size used before (256^2), and a mere 10 kHz bandwidth, vivid edge

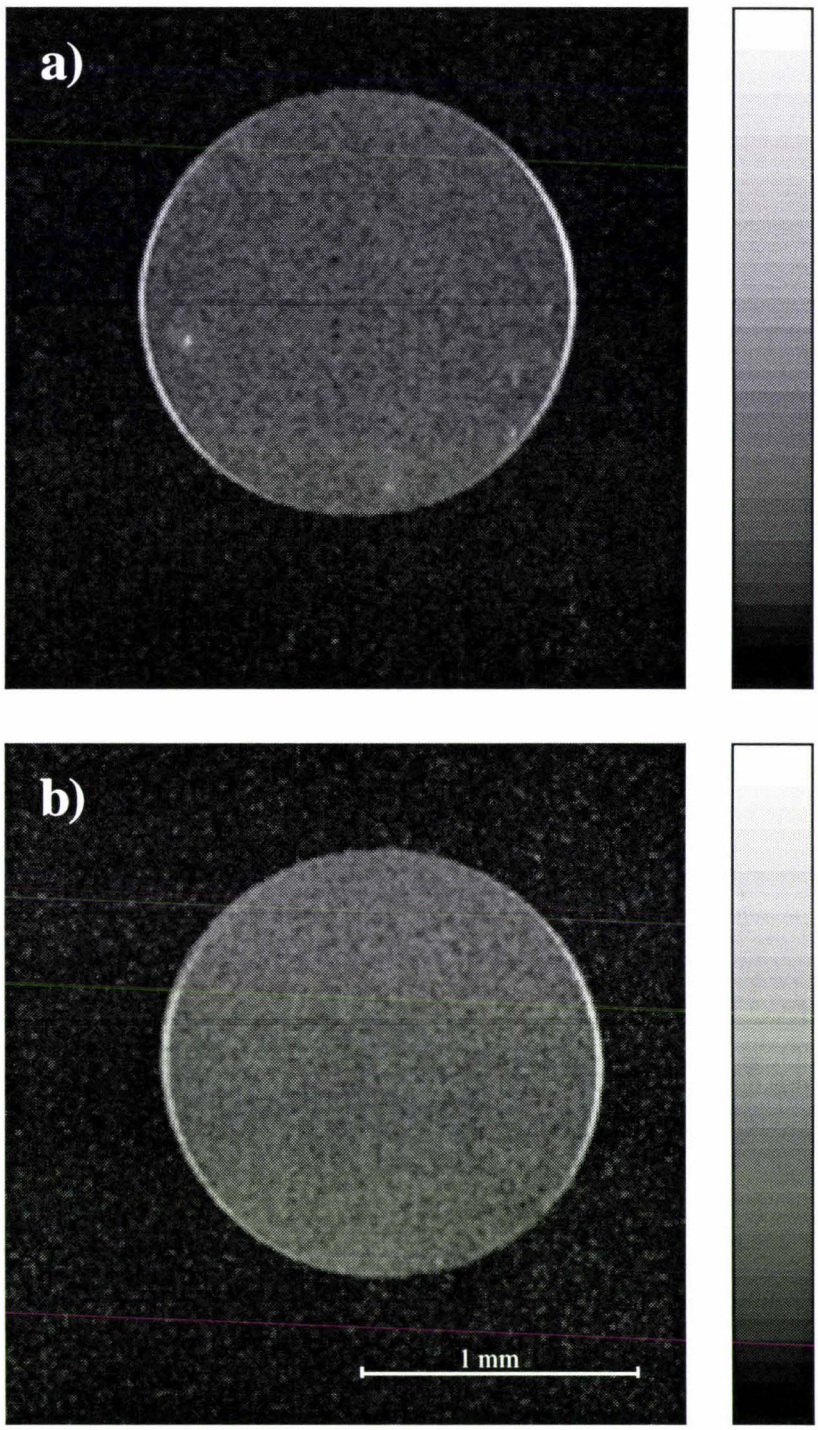

Figure 4.8. (a) Spin echo image of a 1.6 mm ID capillary of water. A decrease in pixel size in this experiment allows diffusive attenuation to be observed at a higher bandwidth than in previous experiments. Reduction of read gradient attenuation can be seen near the walls where molecular diffusion is somewhat slowed in the read direction. (b) Similar image of a capillary containing water filtered with a 0.22 μm pore size filter. The bright flecks visible in (a) seem to have been removed, and may have been due to small particles causing restricted diffusion of the water. Parameters: pulse sequence - spin echo, B_0 = 7 T, bandwidth = 10 kHz, Δx = 9.7 μm, N = 256, n_{acq} = 20, slice thickness = 500 μm, T_E = 32 ms, T_R = 1 s.

enhancement can be seen in Fig 4.8a. It must be remembered here that bright areas indicate an absence of attenuation, rather than any increase of original signal. As predicted there is only detection of diffusion slowed in the *x*- or read direction, giving rise to crescents on the left and right where molecules interact with the walls, rather than a full circle. The presence of curious bright flecks in the body of the water introduces the possibility of observing fine unresolvable objects by the strong indirect detection of restricted diffusion. Presuming the objects to be particles of dust, or less likely small bubbles, the same experiment was repeated using distilled water which had been passed through a 0.22 μm pore size filter. The result, in Fig 4.8b, shows an absence of such bright spots supporting our assumption. This type of powerful sensitivity to solid impurities might have a variety of uses, especially as it is not even necessary that the object possess different susceptibility. For example the purity of a liquid sample might be tested this way.

4.5 Model System with Multiple Cylinders

Many samples imaged by NMR have a periodic structure, with arrays of cells in biological systems and pores in porous media etc. How can the model of a single cylinder be expanded to accommodate a closely-packed array? In fact it is very simple, because the magnetic field offsets produced by each 'unit' of a complex structure will simply add. Strictly-speaking the field offset from one unit will itself induce an extra component in the next, and vice-versa throughout the array, but in reality the field offsets generated by the main field are already several orders of magnitude (five here) smaller than that main field. Therefore we may neglect any second-order induced offsets, and the field contribution from each may be determined independently and then summed for the final effect. A bundle of nine glass cylinders identical to those used previously were packed into another identical capillary filled with water and imaged, again with a range of bandwidths. It was necessary to use a bandwidth of 40 kHz to achieve an undistorted picture, and it wasn't instructive to go as low as 1 kHz because there was little left to see, so a range from 2.5 kHz to 40 kHz was employed (shown in Fig 4.9). The regular bright spots occurring in the images of a single cylinder do not all persist through to the final result as they are no longer cleanly focused, instead being pushed and pulled in conflicting directions, giving rise to some intense points in unexpected positions. The three rods in a row along the 'bottom' of the tube give a reasonably regular pattern, with the two bright vertices on the right hand of each rod showing up, and the ones on the left side cancelling except for the last of the row on the left. Thus an irregular pattern of objects will be hard to interpret or even see after cancellation and attenuation, but a repeating one may be more amenable to analysis.

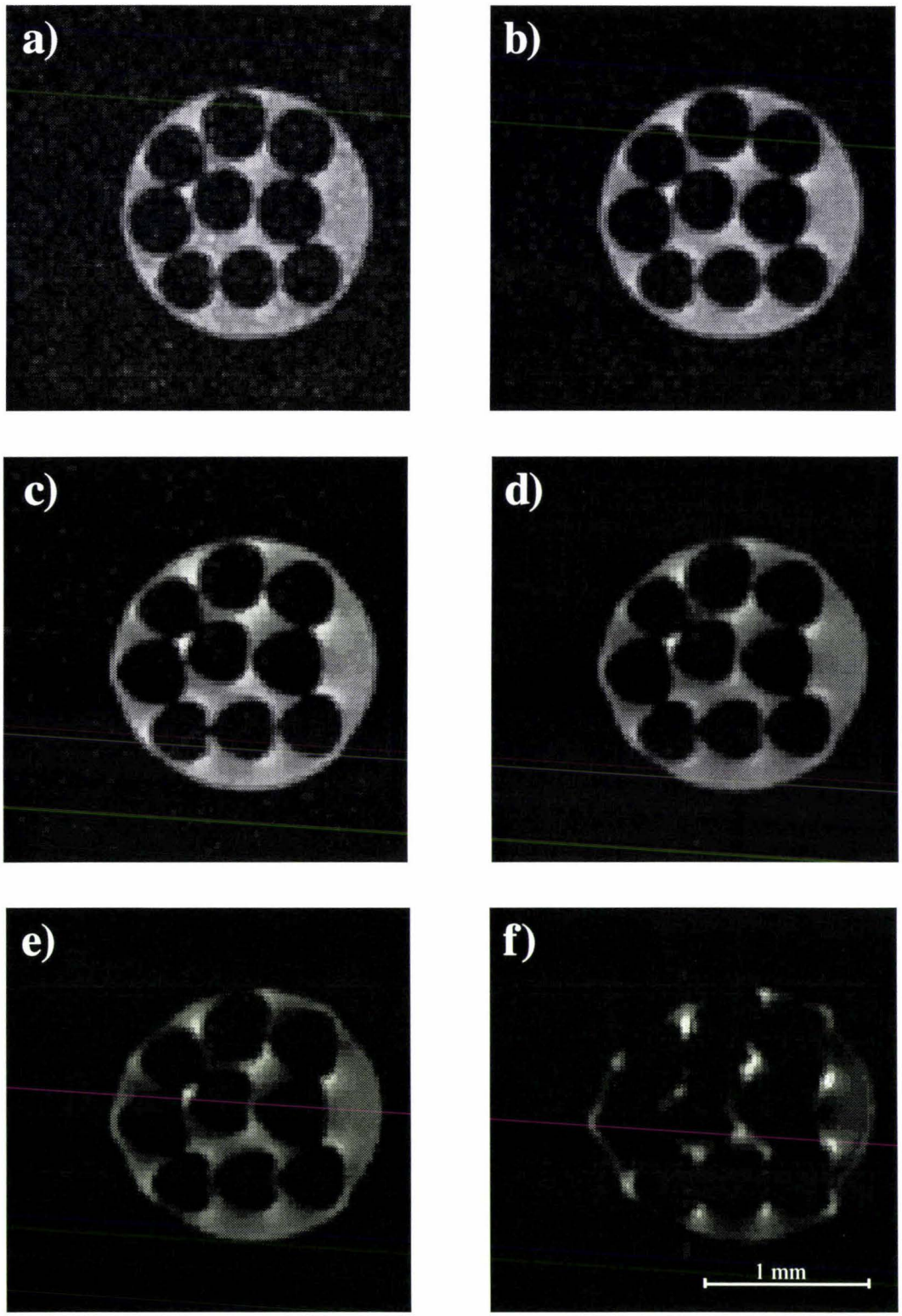

Figure 4.9. A series of spin echo images under the same conditions as Fig 4.5, except that the sample consists of a bundle of glass rods inside a capillary of water. Bandwidths used were (a) 40 kHz, (b) 20 kHz, (c) 10 kHz, (d) 7.5 kHz, (e) 5 kHz and (f) 2.5 kHz giving echo times T_E of 10, 13, 19, 24, 32 and 58 ms respectively. The normal arrowhead distortion is less distinct in the low bandwidth images due to interference between neighbouring rods. $\Delta\chi_m$ is approximately 0.7×10^{-6}. Parameters: pulse sequence - spin echo, B_0 = 7 T, Δx = 19 μm, N = 128, n_{acq} = 20, slice thickness = 500 μm, T_R = 2 s.

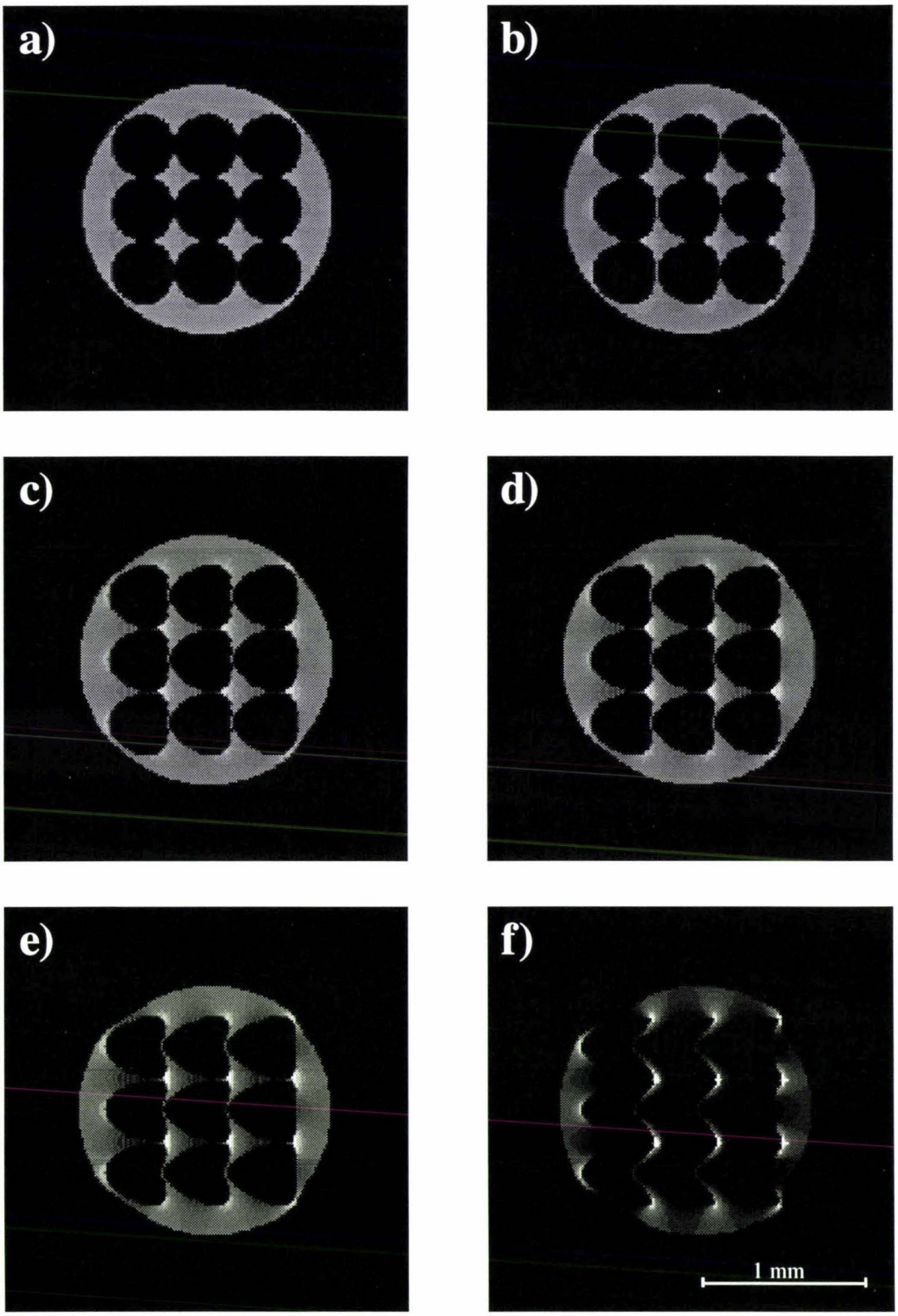

Figure 4.10. Computer-simulated images calculated using the conditions of the experiment shown in Fig. 4.9. Bandwidths correspond to (a) 40 kHz, (b) 20 kHz, (c) 10 kHz, (d) 7.5 kHz, (e) 5 kHz and (f) 2.5 kHz. The attenuation is calculated as though the pixel size Δx is 19 μm as in the real experiment. Absolute image intensities are not directly comparable with those in Fig. 4.9 because of the bandwidth dependence of the noise level in the experiments. Parameters: $B_0 = 7$ T, $\Delta\chi_m = 0.7 \times 10^{-6}$, $D = 2.5 \times 10^{-9}$ m^2 s^{-1}, $\Delta x = 9.7$ μm, $N = 256$.

The corresponding simulation, carried out for nine such rods in a perfectly regular arrangement, is demonstrated in Fig 4.10. There is a good likeness between experiment and simulation, including the distortion of the tube wall where the rods come in close proximity. On the left the wall bends in towards the rods, and on the right it bulges out away from them. Once again it is not easy to normalise the intensities of the experimental images and so directly compare absolute intensity with simulation.

4.6 Direct Visualisation of Susceptibility-Related Gradients

The ability of CPMG pulse sequences to allow very long echo times while suffering little or no diffusive attenuation grants us a new means of examining the local gradients present (i.e. those other than ones applied for imaging). If parameters usually resulting in negligible signal loss at the minimum echo time and severe loss at extended echo times (despite long intrinsic T_2) are employed, then an extra delay may be inserted into the minimum sequence so as to enhance only the attenuation caused by the non-imaging gradients. This is specifically achieved by our CPMG sequence (Fig 2.4) described in Section 2.9 which adds the delay into the space before the imposition of the phase gradient and read precursor and after the 90° excitation pulse. Hence although the main part of the sequence is unchanged, there is a long period during which the only gradients present will be those present at all times.

The results of this technique for our multiple cylinder system are shown in Fig 4.11. A long additional delay of 100 ms was inserted before the read precursor as mentioned and a number of refocusing 180° pulses were spread appropriately throughout this delay, ranging from one to ten. With the single pulse only, the resulting image (Fig 4.11f) is not even recognisable as the original sample, but with ten (and a corresponding half delay between pulses of 5 ms) all of the signal is regained (Fig 4.11a). We would expect the CPMG train to reverse the attenuation effects since the scale of the cylinders is large enough to form slow exchange conditions. An added advantage of this technique is that the attenuation effects are able to be viewed without increasing distortion of the shapes.

More telling is the same treatment on the original sample containing only the single cylinder, seen in Fig 4.12. Identical parameters were employed, giving a clear picture much removed from the ever-present arrowhead. In these circumstances we need no longer handle G_x^{loc} and G_y^{loc} separately as in previous analyses. This is because during the period added before imaging, any gradient G present in the x- or y-direction, positive

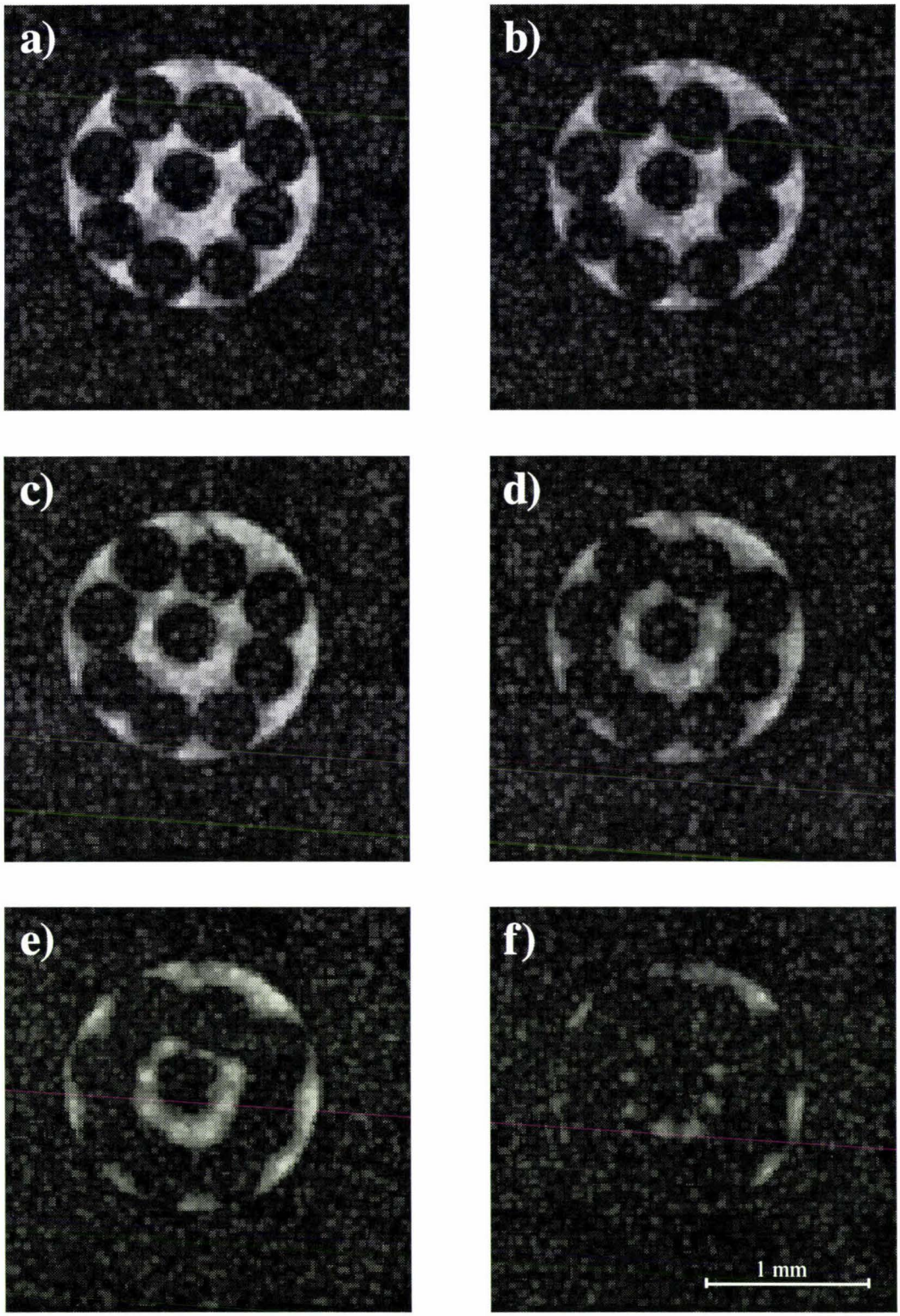

Figure 4.11. A series of CPMG images of the multiple cylinder sample. Each instance had a number of 180_y pulses (n) inserted into a long delay (100 ms) situated before the read precursor. The images are in order of decreasing n, specifically (a) 10, (b) 7, (c) 4, (d) 3, (e) 2, (f) 1. The severity of the attenuation is dependent on the interpulse spacing, as the refocusing pulses can reverse the diffusive attenuation effect if sufficiently close together. $\Delta\chi_m$ is approximately 0.7×10^{-6}. Parameters: pulse sequence - CPMG, B_0 = 7 T, bandwidth = 20 kHz, Δx = 19 μm, N = 128, n_{acq} = 8, slice thickness = 500 μm, T_E = 113 ms, T_R = 2 s.

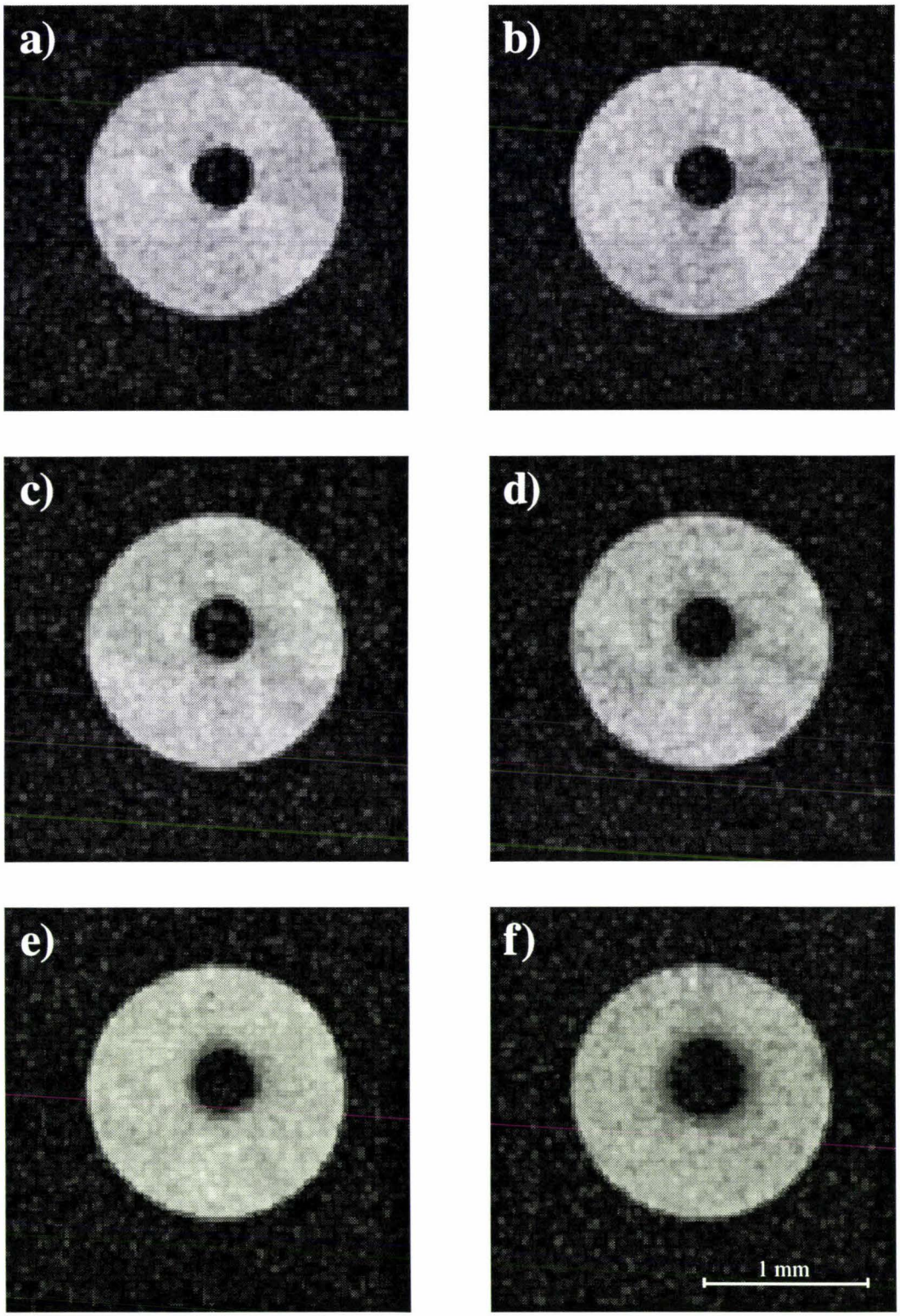

Figure 4.12. A series of CPMG images of the single cylinder sample under the same conditions as Fig 4.11. The number of 180_y pulses n for each case is again (a) 10, (b) 7, (c) 4, (d) 3, (e) 2, (f) 1. The attenuation, most visible in (f) with only one 180_y pulse, reflects the form of the modulus of the local gradient offsets ΔG_x^{loc} and ΔG_y^{loc}, because these are the only gradients present during the long delay before the read precursor gradient. $\Delta\chi_m$ is approximately 0.7×10^{-6}. Parameters: pulse sequence - CPMG, B_0 = 7 T, bandwidth = 20 kHz, Δx = 19 μm, N = 128, n_{acq} = 8, slice thickness = 500 μm, T_E = 113 ms, T_R = 2 s.

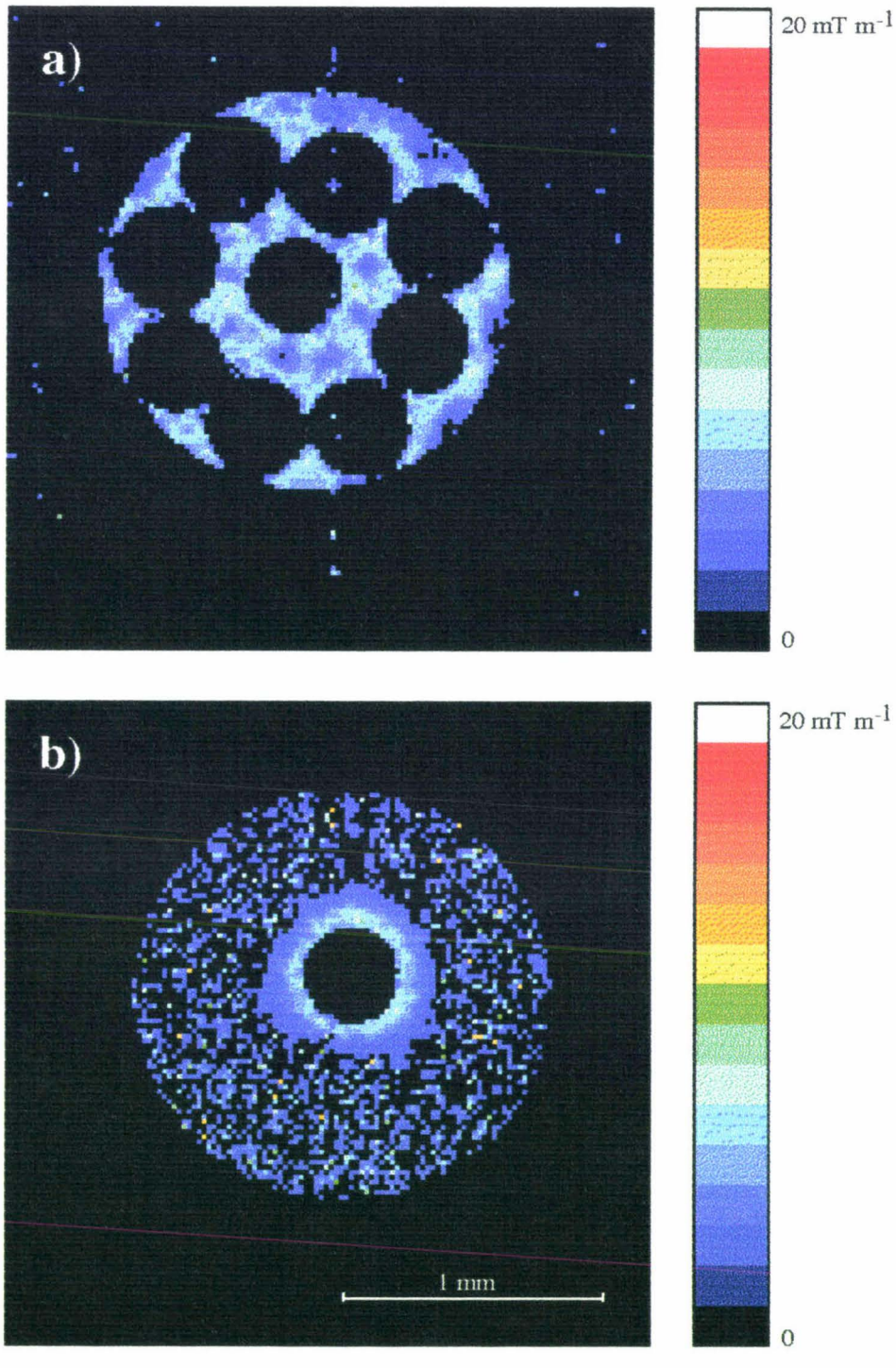

Figure 4.13. Maps of ΔG^{loc} (the modulus of the x- and y-components) for the (a) multiple and (b) single cylinder samples. These were calculated from the series of images in Fig.s 4.11 and 4.12 by standard exponential fitting. (c) and (d) show the same maps simulated by computer for comparison. The experimental maps have values somewhat reduced from the simulations, possibly because the self-diffusion coefficient is a little lower close to the rod wall than in the bulk as was seen in Fig. 4.8. Parameters: B_0 = 7 T, $\Delta\chi_m$ = 0.7 x 10^{-6}, Δx = 19 μm, N = 128.

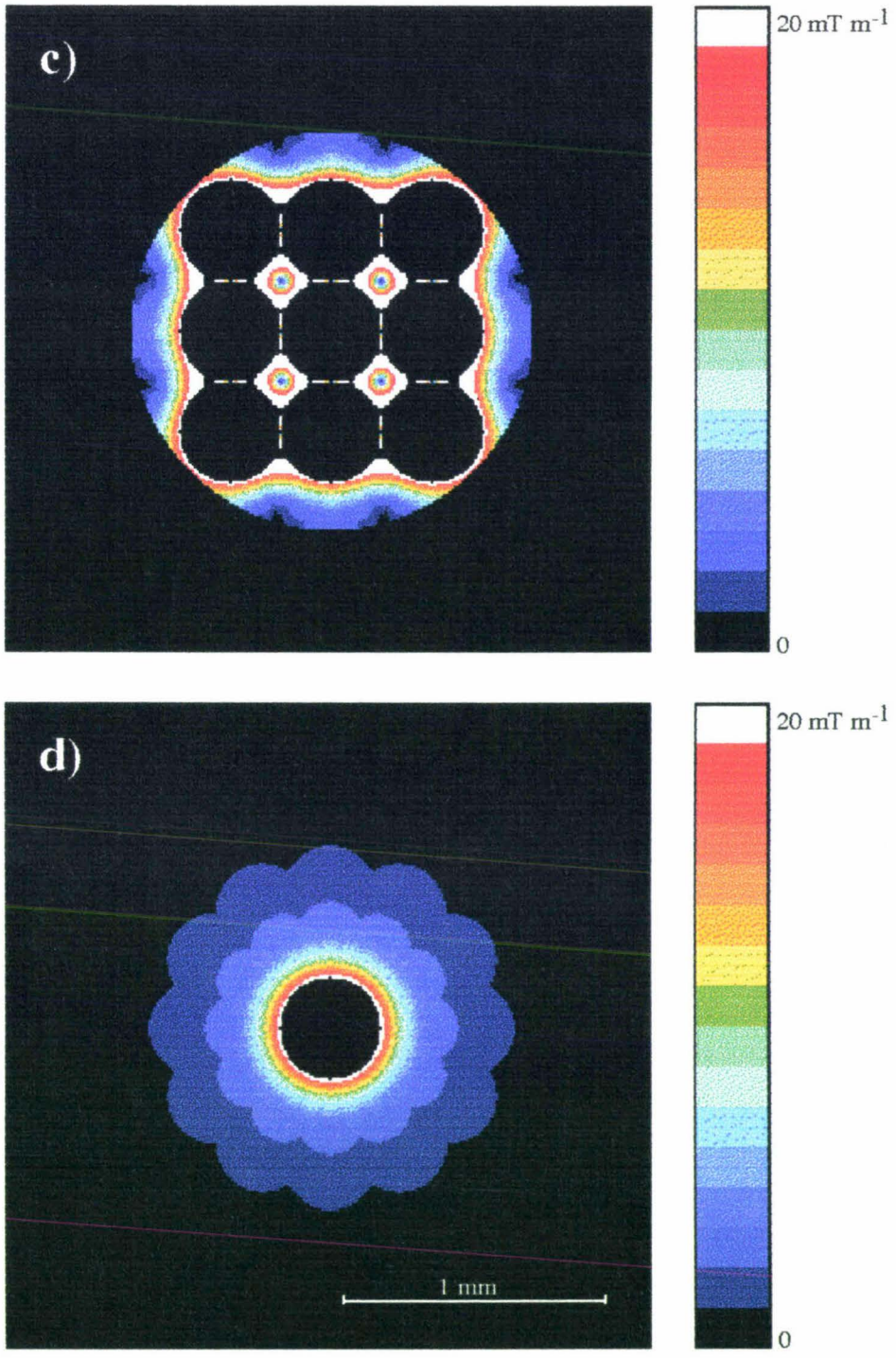

Figure 4.13 (c), (d)

or negative, will induce attenuation according to its magnitude by the formula $\exp(-\frac{1}{3}\gamma^2 G^2 D t^3)$, where t is the duration of that certain period. Thus the attenuation seen mirrors the shape of a map of G^{loc}, obtained from $(G_x^{loc2} + G_x^{loc2})^{1/2}$. The simulated G^{loc} map is displayed in Fig 4.13d.

These images may also be analysed to actually measure the absolute G^{loc} magnitudes, giving a calibrated map. As explained in Section 2.5, the attenuation for our

CPMG images is given by $\exp(-\frac{1}{3}\gamma^2 G^{loc2} D(\frac{\tau}{n})^2 \tau)$, and if this is compared to the familiar T_2 relaxation expression $\exp(-t/T_2)$ it is evident that normal T_2 analysis, substituting $(\tau/n)^2$ for t, will extract the factor $(\frac{1}{3}\gamma^2 G^{loc2} D\tau)^{-1}$ in place of T_2. Hence G^{loc} is easily calculated knowing γ, D and τ, and maps of G^{loc} are shown in Fig 4.13 for both the bundle and the single cylinder. Comparison with the respective simulated G^{loc} maps, also shown (with identical scales), confirms that the shape of the gradient distribution is in good agreement, but the magnitudes are not quite the same. Concentrating on the single cylinder, the values within a few pixels of the cylinder surface are as much as four times smaller than in the simulation, whilst further out they are around two times smaller. It is more difficult to estimate the disparity for the bundle of cylinders as they are not evenly stacked (as in the simulation), and thus the superposition of the gradients of different cylinders will cancel and add in altered ways. The loss or reduction of the largest gradients close to the cylinder surface is not straightforward to explain. Obviously the pixels actually on the boundaries between glass and water will not be useful for analysis due to the reduced signal available. It is possible that the ten 180_y rf pulses used to regain maximum signal do not quite succeed in preserving all of the phase coherence which is lost with only one pulse, either because the interpulse period is still too long at 10 ms (the shortest time) or because the pulses are not perfectly 180_y, but comparison with normal spin echo images (without the 100 ms delay) of the same bandwidth doesn't support this. The best explanation may be a reduction of D itself next to the glass rod due to restricted movement, just as we observed in Section 4.4 on the inside capillary walls.

It will be interesting to apply the same CPMG treatments to the biological case studies where it is more than likely that there is as much heterogeneity below visible resolution (most cells will be unresolvable!) as is actually apparent in images, meaning that fast exchange susceptibility-related effects may also be present. These are unaffected by CPMG refocusing.

Chapter 5

Plant Microscopy

5.1 Introduction

Finally we may apply the knowledge gained about susceptibility and diffusion effects from exploring simple model samples to the more complex examples likely to be encountered in everyday NMR microscopy. In particular we will be studying the small stem of a common dicotyledonous weed, *Stachys sylvatica* L. or 'hedge woundwort'. In cells large enough to be seen individually in the image the phenomena occurring at the boundaries may be observed and in other tissues susceptibility-related distortion and attenuation, as well as non-related relaxation mechanisms, will produce a final average intensity. This kind of thorough attempt to correlate image contrast with known cell characteristics may help to provide understanding in the future sufficient to enable recognition of such characteristics in the NMR images themselves without resorting to more conventional microscopy methods.

Although the task of accommodating an entire and intact plant within the strict constraints of a microimaging probe inside a superconducting magnet is at times tricky, it seemed important not to excise the stem and destroy the normal water relations (especially the typical positive pressure in the phloem and tension in the xylem) which surely influence the NMR parameters we see. The plant species, a small herbaceous weed which grows in abundance in the gardens of Massey University and which has been studied before *(96,97)*, was suitable because of the easy availability of many small seedlings which could be readily grown to a suitable size in the glasshouse in just a few weeks. *Stachys sylvatica* also typically exhibits an erect, unbranching habit, and a thick, robust stem, ideal for the study of stem morphology by imaging.

5.2 Materials and Methods

Stachys sylvatica is classified in the Labiaceae family along with the more commonly known mint, and it has the unusual square cross-sectional stem profile characteristic of the family. It has a considerable covering of hairs, rather like the nettle, especially on the undersides of the leaves. A strong rib is present at the four 'corners' of the square stem giving the stem much rigidity and enabling the erect habit in windy conditions. The stem has a diameter of about 4 mm when it has reached a height of approximately 25 cm, and about 2 mm at a height of 15 cm. A red pigment (anthocyanin) appears in the stem as it ages. The leaves are pointed heart-shapes and are arranged in

opposite and alternate conformation on the stem. *Stachys sylvatica* is very efficient at vegetative multiplication by runners under the ground and so can create a problem in gardens, but it also sets seed in the right conditions, with small purple flowers pollinated by bees. Care had to be taken to excise any runners from the primary root prior to significant growth in the glasshouse as we required a single plant for these experiments.

The microimaging apparatus provided some challenges and drawbacks in its present form. The receiver rf coils with diameters of more than 5 mm did not allow a water-filled tube to protrude down into the probe below, an essential feature when working with live stems so that roots may remain intact. Although the 5 mm coil is ideal for maximum sensitivity in a stem roughly 2-4 mm wide, it is not easy to gingerly feed either the roots or leaves through the small coil to enable it to surround the stem. Obviously a purpose-built receiver coil would solve these problems, but for the short period in which the plant was required to be healthy, this system was adequate. Plants without large nodules or runners on the roots were chosen, and the roots were selectively pruned until they could be inserted into a 5 mm diameter tube of water, ready to be threaded through the rf coil. This arrangement is shown by photograph in Fig 5.1, with a typical plant positioned inside a tube beside the probe. Unfortunately the lowest leaves of the plant must also be excised, preferably some time before the experiment to allow healing, so that the saddle coil may be positioned at an appropriate internode of the stem. Fig 5.1 also shows the specific coil used, and a plant in place for an experiment. The gradient coils were easily slipped on outside the plant and rf coil. While in the superconducting magnet bore the plant did not receive much light, necessary for studying growth processes, but not for the simple scrutiny of tissue properties. The roots were also not aerated, a treatment vital for sustained viability (to avoid root decay). Thus the plants became unhealthy after some days in the experimental set-up if not removed, and so all experiments on a single plant were completed within 12 hours to avoid deterioration of the sample. Further modifications of the apparatus would enable more complex and on-going developmental plant studies.

5.3 Stem Anatomy

A preliminary transverse image of one such plant (using a spin echo), with conditions favourable to avoid most T_1 and T_2 relaxation, is depicted in Fig 5.2. That is, it was possible to lengthen the repetition time to the point where no T_1 contrast was observed, but not to shorten the echo time to zero, so the remaining variation in intensity is due both to concentration of water and slight transverse relaxation. All of the main

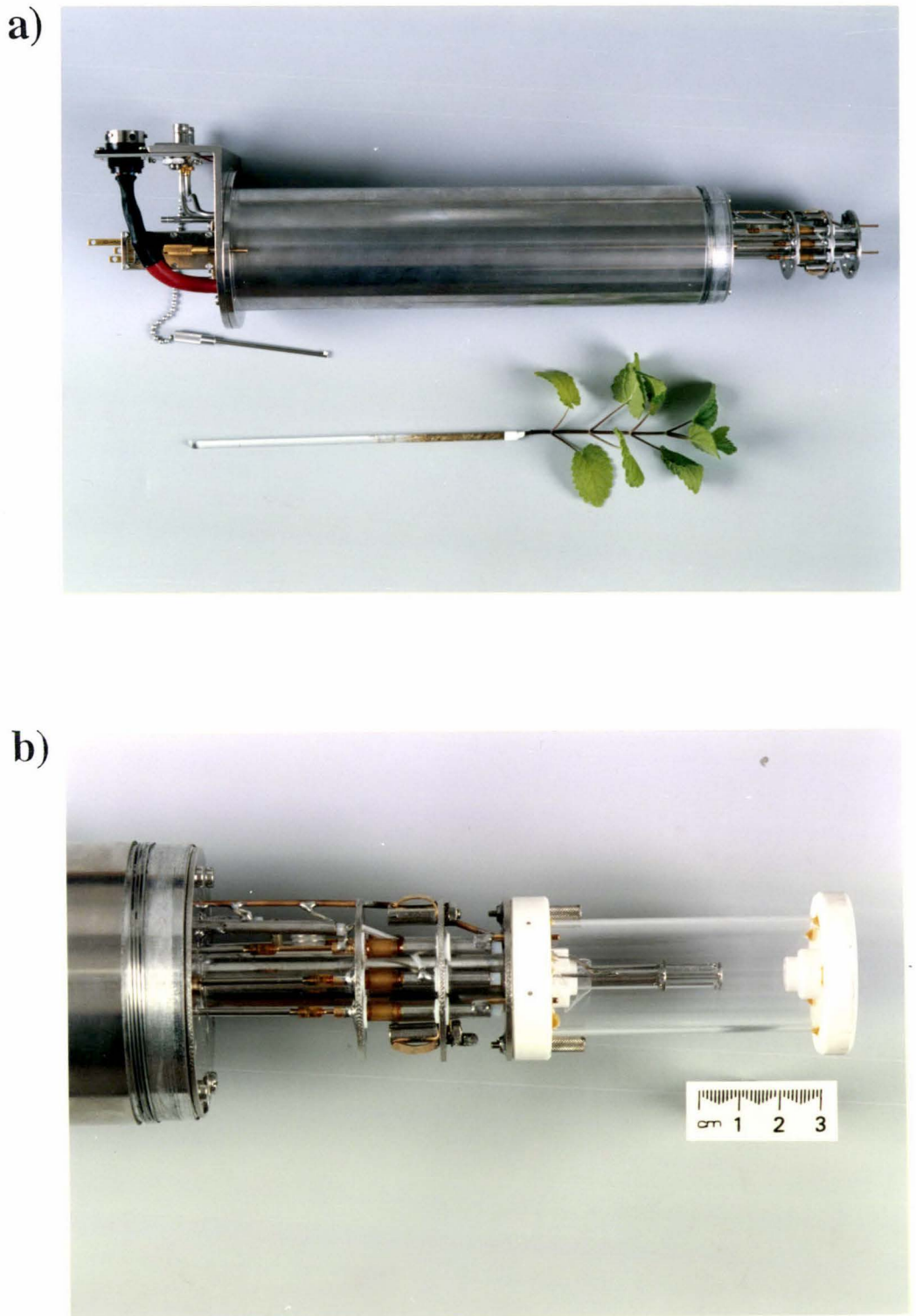

Figure 5.1. (a) Microimaging probe and *Stachys sylvatica* plant ready for insertion into the apparatus. (b) 5 mm radio frequency saddle coil. (c) Plant positioned in the rf coil after excision of the lower leaves, and in the gradient coil set (d) ready for imaging.

c)

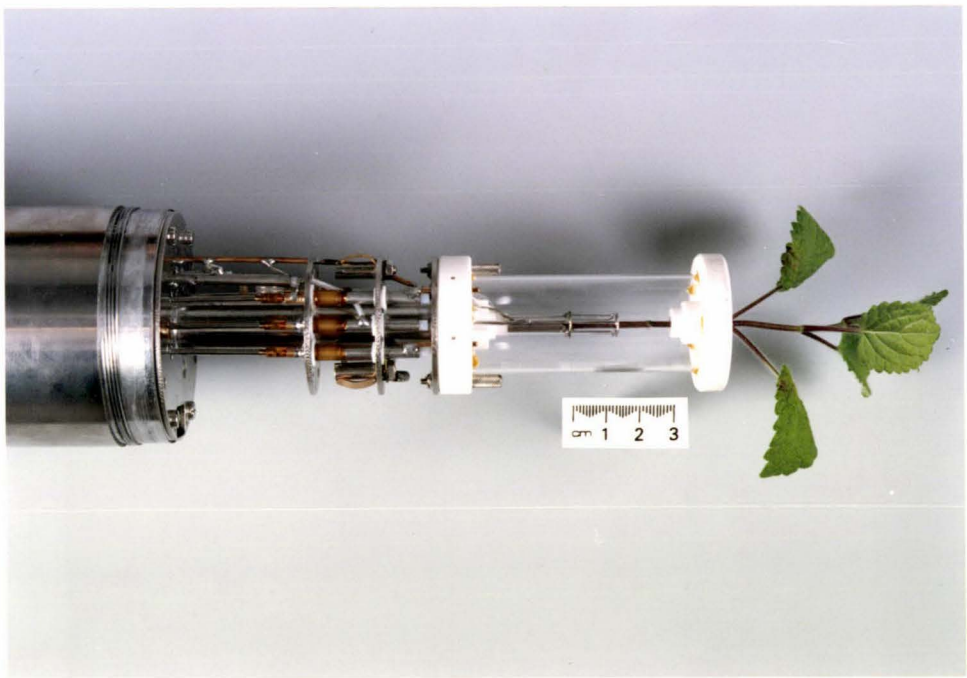

d)

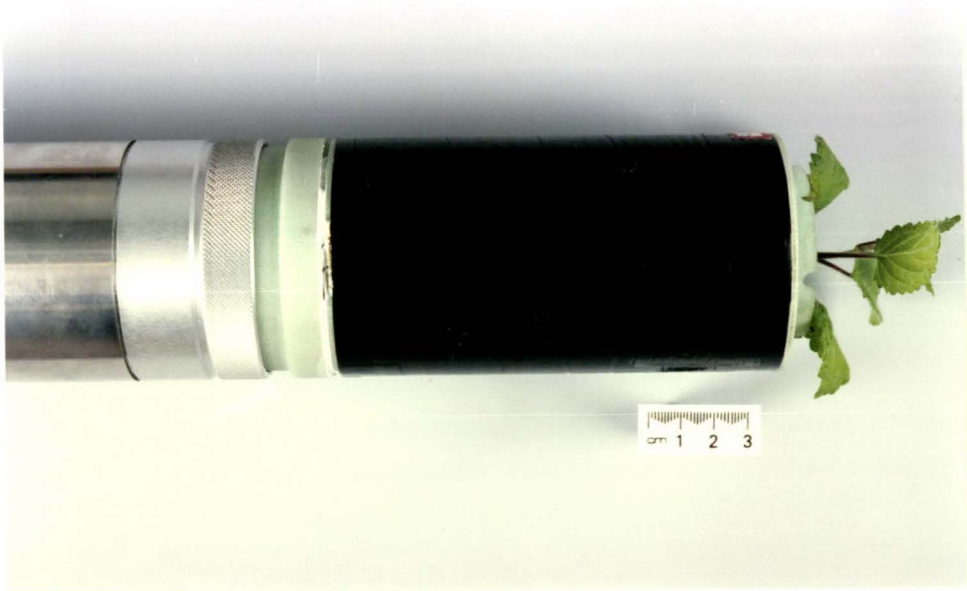

Figure 5.1 (c), (d)

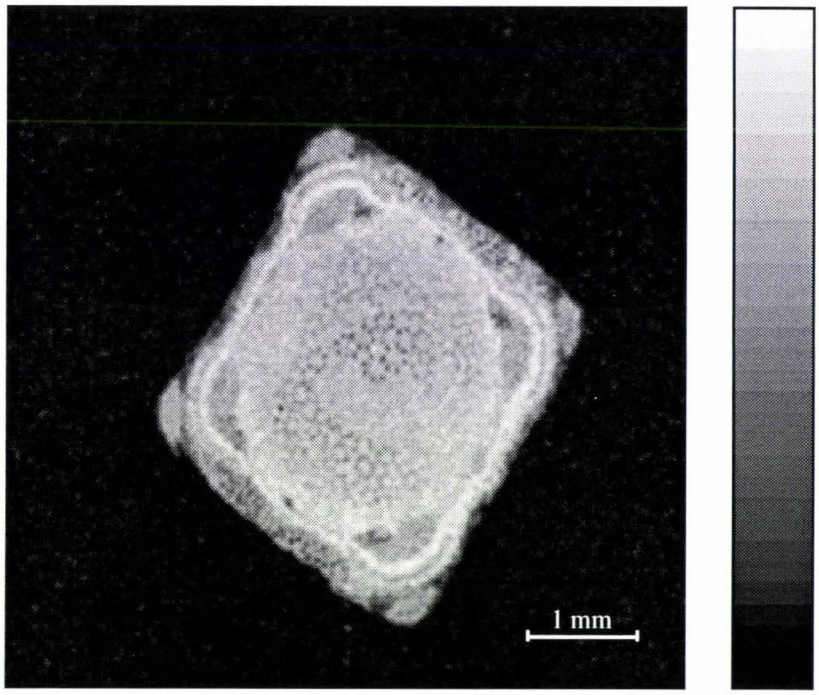

Figure 5.2. Spin echo image of the stem of *Stachys sylvatica* using long repetition time and minimum echo time to avoid most relaxation contrast. The plant is set up as shown in Fig. 5.1. Parameters: pulse sequence - spin echo, B_0 = 7 T, bandwidth = 40 kHz, Δx = 23 μm, N = 256, n_{acq} = 2, slice thickness = 500 μm, T_E = 10 ms, T_R = 4 s.

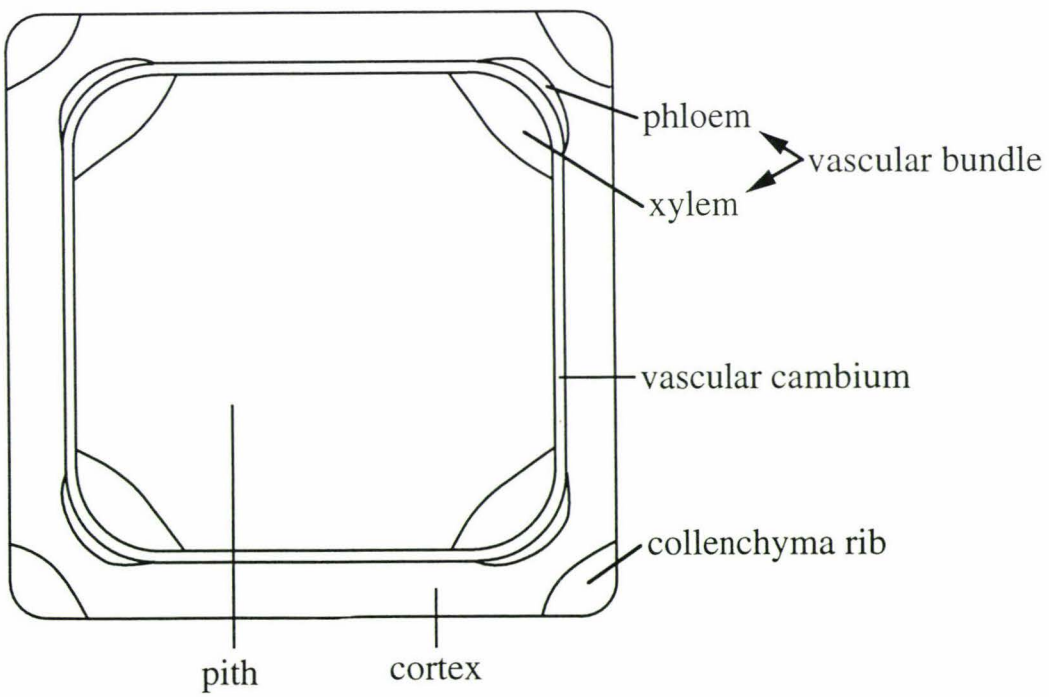

Figure 5.3. Schematic diagram of a typical *Stachys sylvatica* stem. The vascular cambium can be seen in the spin echo image (Fig. 5.2) as a thin bright ring, and the phloem is recognisable as the narrow dark line just outside the cambium. In fact the phloem appears to be sandwiched between the relatively bright cambium and cortex tissues.

tissue types may be distinguished here, illustrated further by a stylised diagram of the stem (Fig 5.3). The large-celled pith is seen in the centre, consisting only of parenchymatous or ground tissue with large air spaces between cells to allow circulation of air in the stem. The pith generally has little useful function, and indeed as the diameter of the stem increases via secondary growth the pith cells may fail to expand sufficiently rapidly and may be torn apart to leave a cavity. Choice of vertical position along the stem will therefore determine the presence or lack of pith for observation. This image was taken at a distance of approximately 2 cm from the roots.

Four separate vascular bundles are seen toward the 'corners' linked by a narrow ring of vascular cambium. The ground tissue on the inside of the cambium is known as pith, and that toward the outside is cortex. In the extreme corners are ribs of collenchyma cells, which are usually thin and elongated, and themselves contain heavy ribs of wall thickening. These ribs confer structural strength on the stem over that provided by the highly-lignified xylem in the vascular bundles. Each bundle consists of xylem tissue on the inside, which is primarily involved in water transport upwards from the roots to the leaves, and phloem, which facilitates nutrient transport from sources such as photosynthesising leaves to sinks such as roots. A single layer of meristematic cells, or 'cambium', separates the two primary transport tissues and continues right around the stem, dividing to form a trail of cells on the inside and outside destined to differentiate into new secondary xylem and phloem respectively. Thus the undifferentiated radial rows adjacent to the cambium are collectively called the cambial zone, the ring or cylinder of cells apparent in the image. This secondary formation enables the plant stem to increase in diameter with age, as is conspicuous in growing trees, in order to handle an increased demand for transport and support of the larger plant.

Xylem consists of water-conducting tracheary elements as well as some parenchyma and fibre cells. Tracheary elements are long wide cells with thick lignified walls which no longer have cytoplasmic contents and so are non-living. Elements with no end walls are commonly joined end-to-end to form a vessel, while those separated by end walls are interleaved and connected by numerous pits in the walls. Phloem consists of sieve tube elements with companion parenchyma cells. Again the elements are joined end-to-end to make up a sieve tube, and are separated by end walls perforated by large sieve pores through which cytoplasmic threads are able to pass. Thus the sieve cells are living, but are not separated from eachother by membranes, and do not contain nuclei. In many plants, including *Stachys sylvatica*, the sieve cells are fairly long and very narrow, and would not easily be mistaken for xylem vessels. In our plant it is just possible to see

small pockets of new xylem and phloem forming from the cambium midway between the vascular bundles.

5.4 Imaging of the Stem in Cross-Section

A whole series of imaging pulse schemes was applied to another suitable plant, as shown in Fig 5.4. First a simple transverse image with long repetition time and minimum echo time is shown as before, and then maps of T_1 and T_2 values using images at a range of echo times (T_E) and repetition times (T_R) as explained in Section 2.9. The images processed to calculate the T_2 map also yield an extrapolated map of image intensity for zero echo time. A gradient echo pulse sequence was used to obtain another image with little relaxation contrast, and further images taken at varying T_E gave a map of T_2*. Lastly maps of diffusion and velocity were acquired, to be shown and discussed later. These images may all be compared to the equivalent light micrographs (Fig 5.5) taken after the NMR microscopy was finished.

This stem (Fig 5.4a) seems to closely follow the anatomy in the preliminary image, for example possessing cells in the pith large enough to be barely discernible individually. Although the slice thickness of the image (300 μm) is far too coarse to encompass only a single layer of pith cells, the longitudinal micrograph shows that they are frequently stacked upon one another in loose columns, and this enables us to see the boundaries between some of these columns. The epidermal layer forming the effective 'skin' of the stem, seen often breaking away from the cortex in the transverse micrograph, is not visible in any of the displayed images, although it was intact during the course of the experiments and merely became dislodged during microtoming. It is interesting to see that all four sides of the stem cross-section are not equal, and that there are two opposite concave and two opposite convex sides. There is noticeably less cortex on the concave sides, and the small dark patches appearing in the vicinity of the xylem tissue are always situated nearer to the convex sides. These patches appear to consist of fibres.

Beginning with the gradient echo image (Fig 5.4e), the anatomical features of the tissues would seem to be emphasised greatly by this method, especially in the pith where the boundaries are particularly prominent in comparison with the spin echo images. As gradient echoes are very sensitive to local fields, we might predict that the susceptibility-related artefacts which were so significant in our model systems are also going to be influential here. However more investigation of this assumption by analysis of the other relaxation phenomena is needed to confirm this. In the T_2 map (Fig 5.4c), the uniform

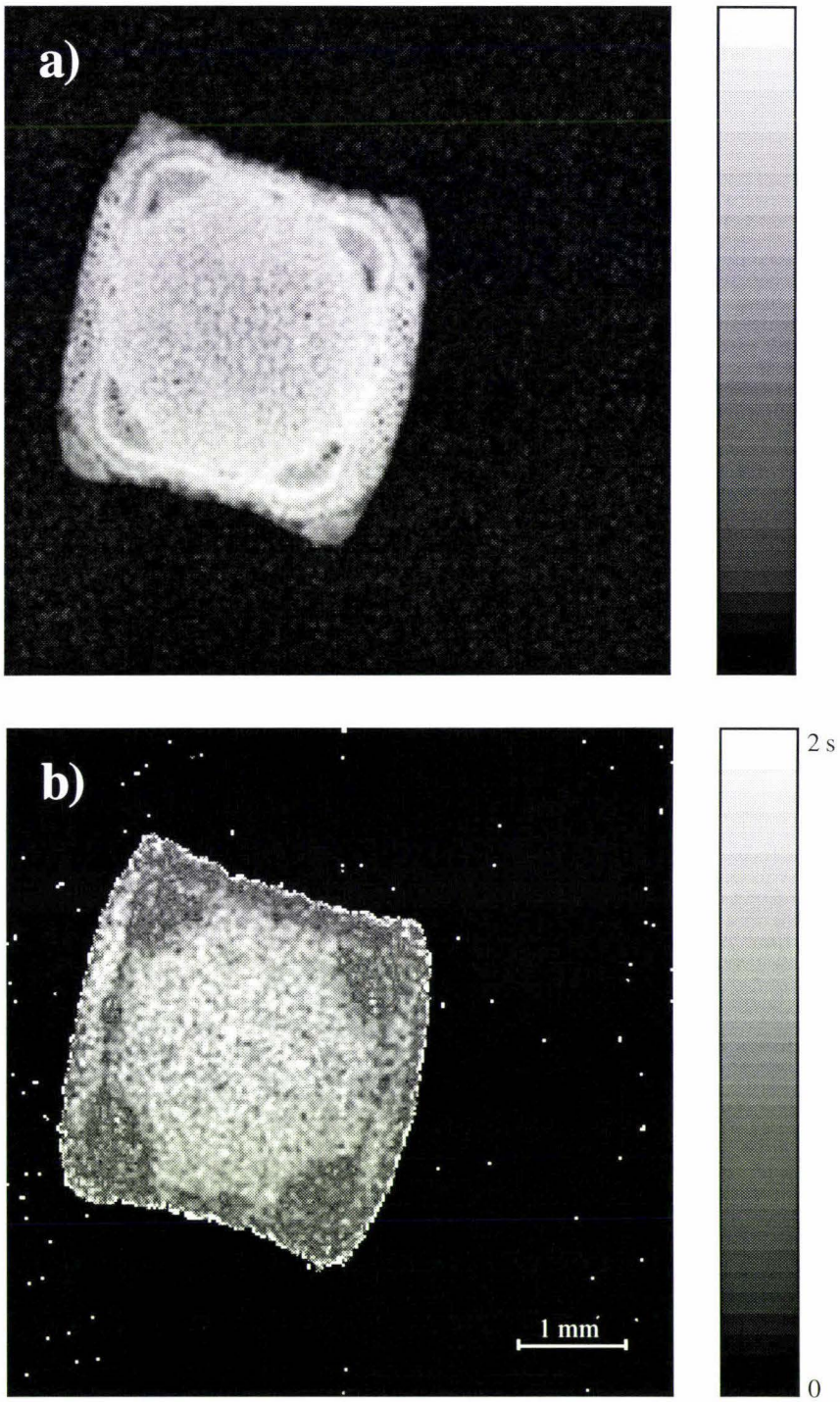

Figure 5.4. (a) Spin echo image of another *Stachys sylvatica* stem with long T_R (4 s) and minimum T_E (10 ms). (b) Map of T_1 relaxation time calculated from a series of images as in (a) at differing repetition times (ranging from 100 ms to 4 s). (c) Map of T_2 relaxation time calculated from a series of images at a range of echo times (from 10 ms to 40 ms). (d) Map of extrapolated proton density also calculated from images at a range of echo times as in (c). (e) Gradient echo image with long T_R (2 s) and minimumT_E (9 ms). (f) Map of T_2^* relaxation time calculated from a series of gradient echo images at a range of echo times (from 9 ms to 40 ms). Parameters: B_0 = 7 T, bandwidth = 40 kHz, Δx = 23 μm, N = 256, n_{acq} = 2, slice thickness = 500 μm.

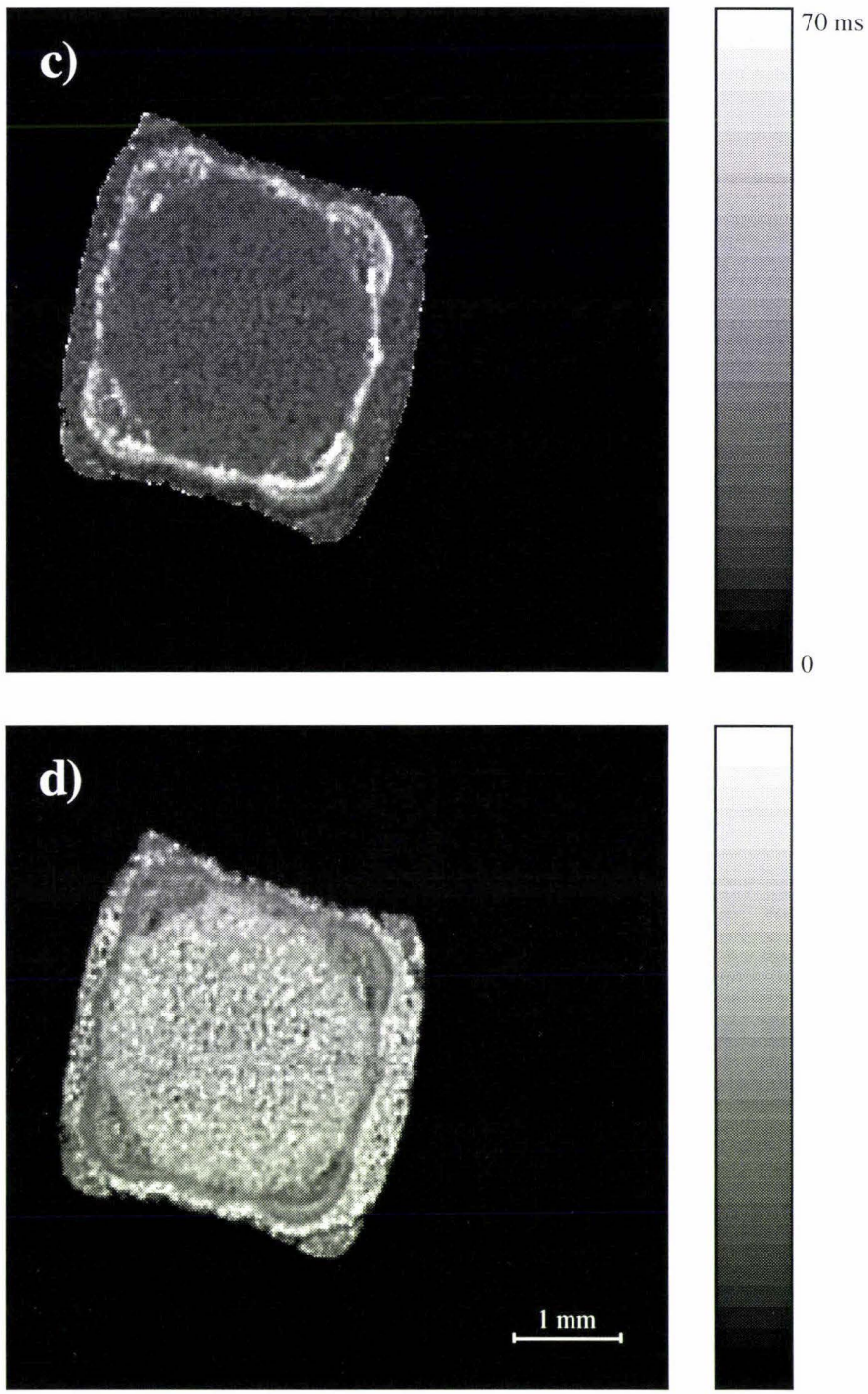

Figure 5.4 (c), (d)

large-celled pith and cortex have a relatively short T_2 ranging from about 11-18 ms, although the thin layer of cortex on the concave sides has a still lower T_2 of 7-11 ms. On the other hand the regions with small cell diameters, e.g. the cambial zone, have significantly longer T_2 values of 30-120 ms. In contrast, the T_1 map (Fig 5.4b) shows the same general areas, the cambial zone and the vascular bundles, to have relatively short

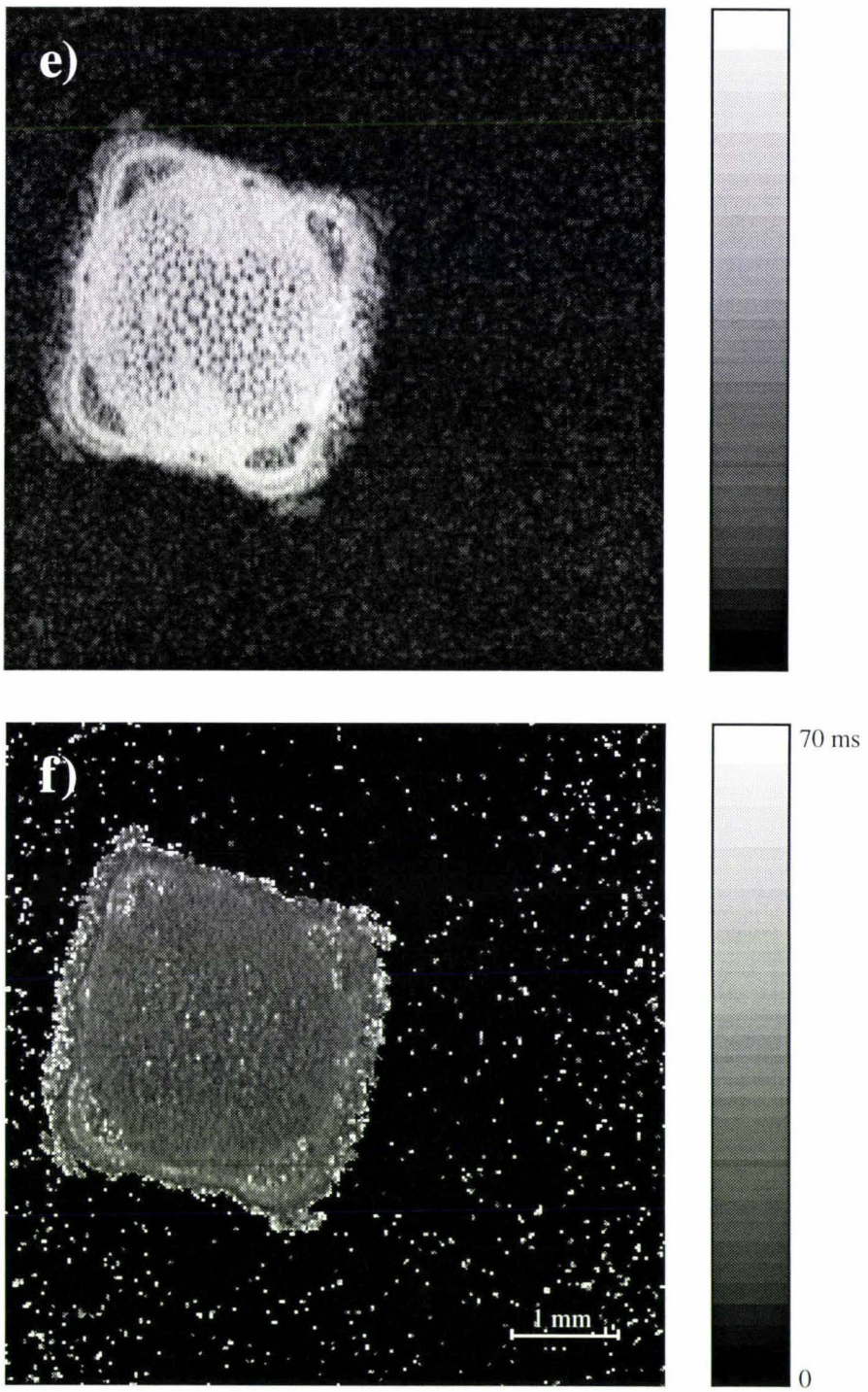

Figure 5.4 (e), (f)

T_1 (300-900 ms) when compared with the values of 1000-1800 ms for the pith and cortex. Before suggesting mechanisms to explain the contrasts seen in these maps, we shall focus on the overall T_1 values in comparison to the overall T_2 values.

a)

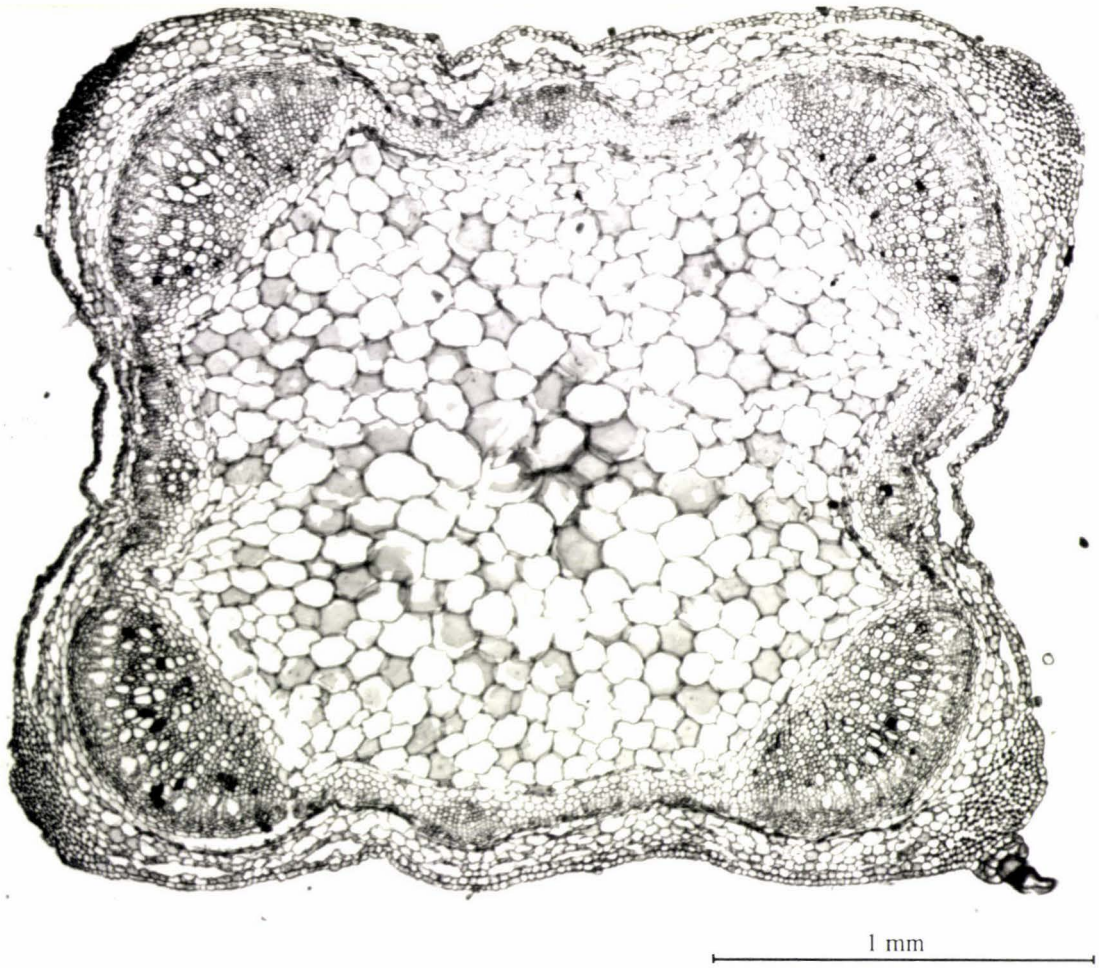

b)

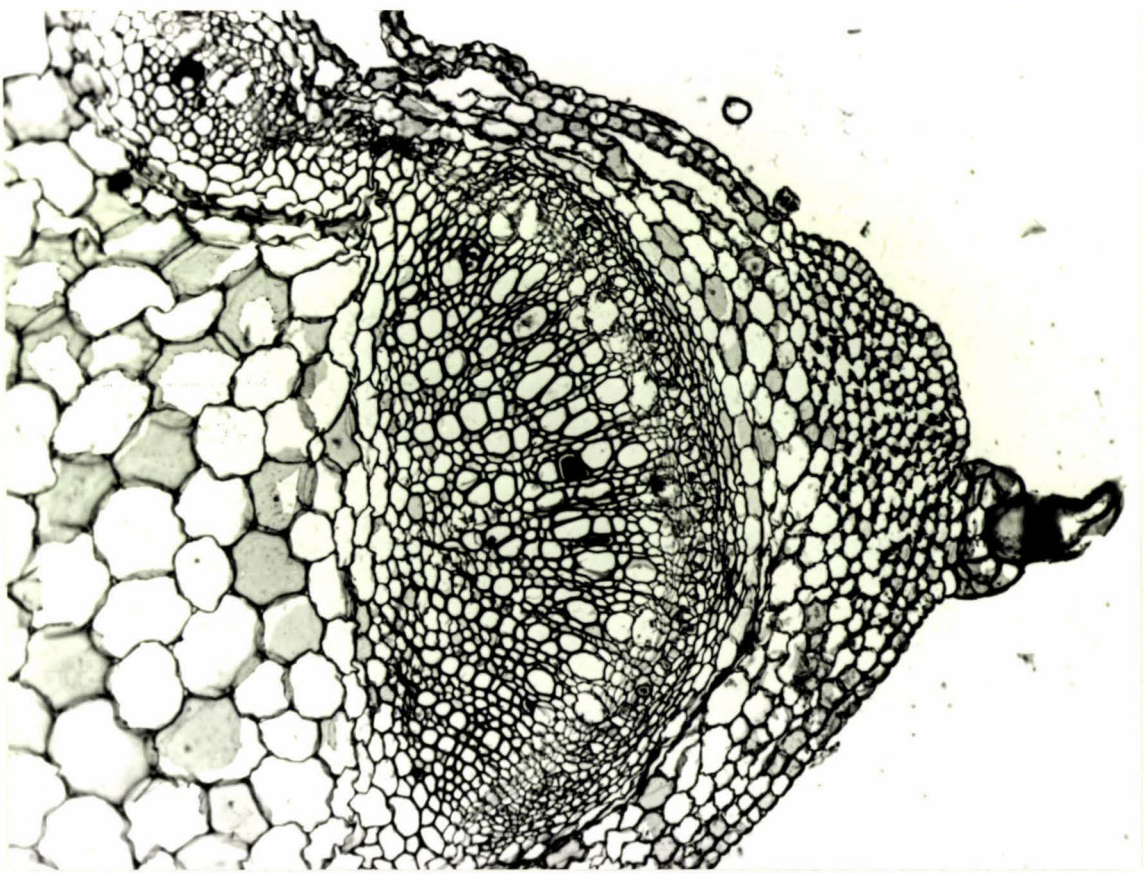

Figure 5.5 (a), (b)

c)

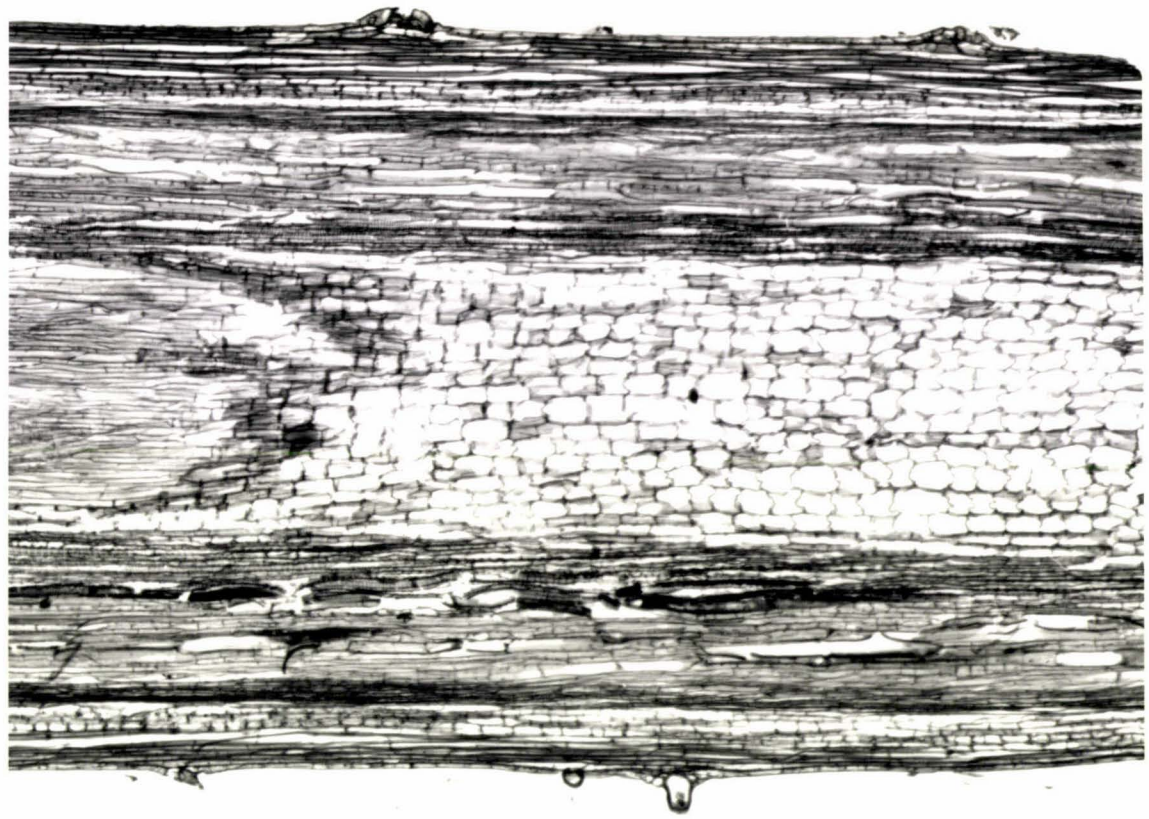

1 mm

d)

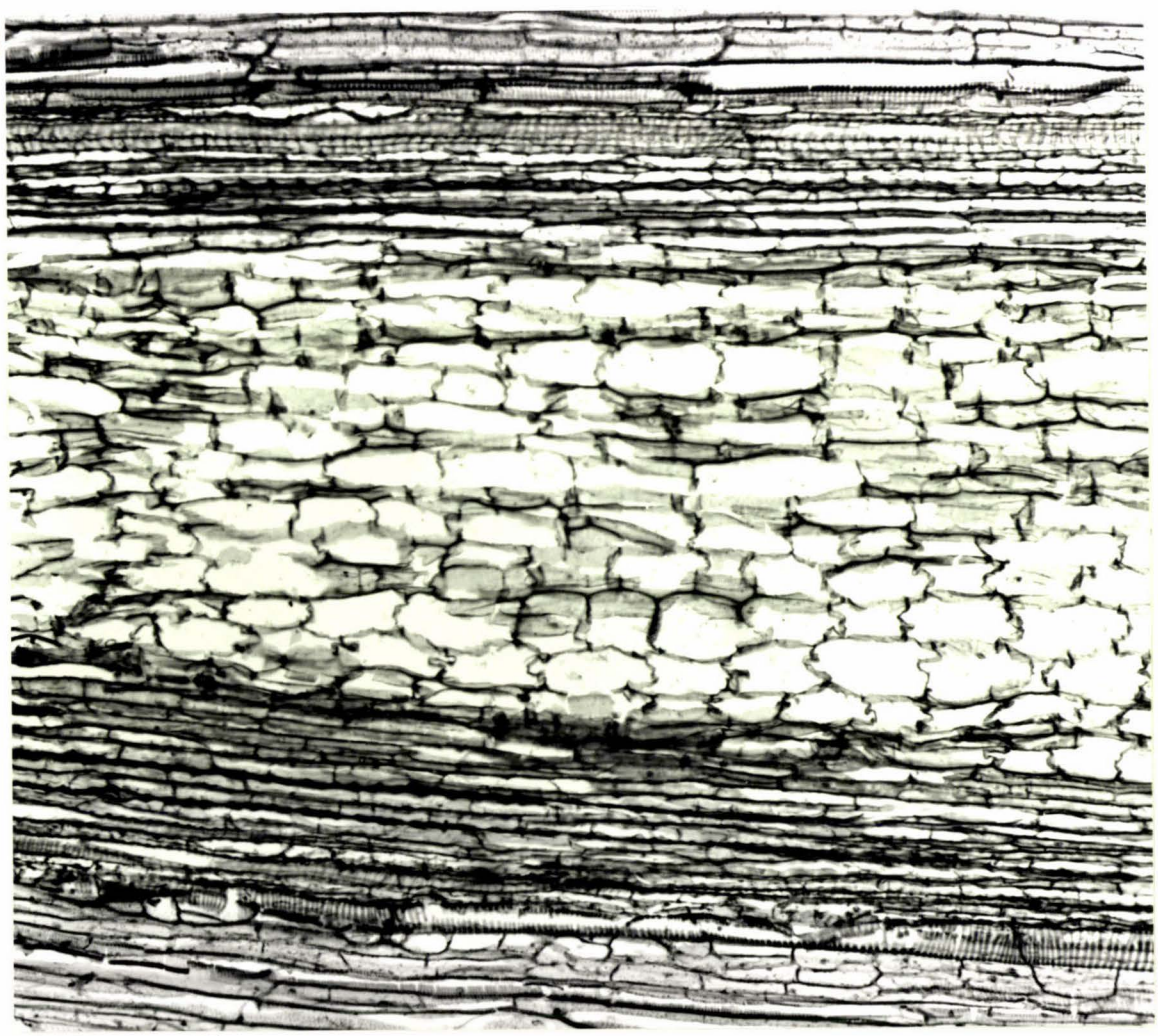

0.5 mm

Figure 5.5 (c), (d)

e)

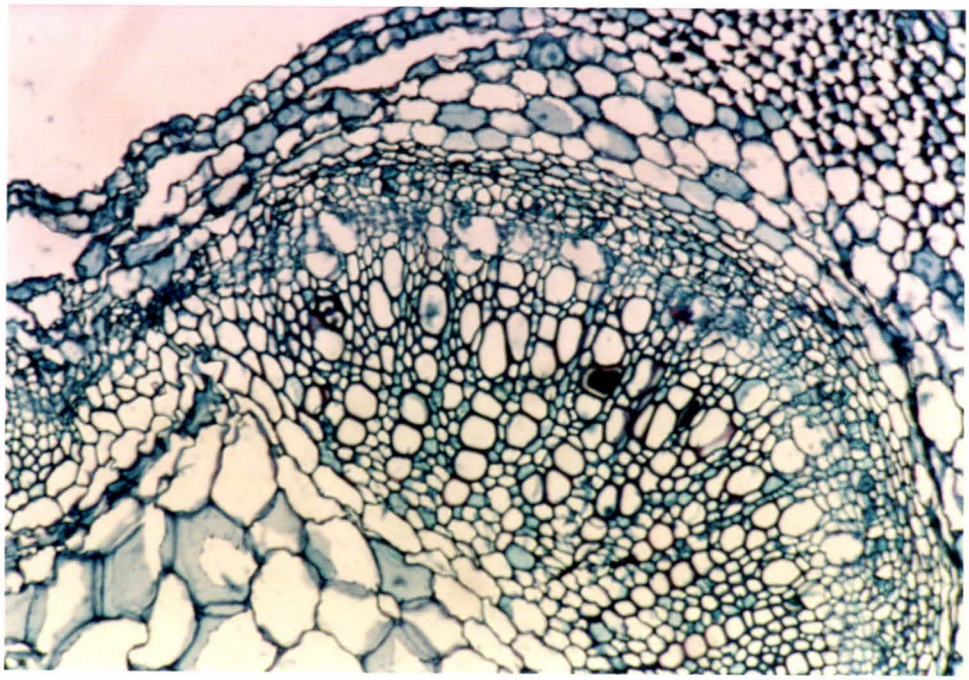

Figure 5.5 (e)

Figure 5.5. Optical micrographs of the same *Stachys sylvatica* stem as in Fig. 5.4. Unfortunately the stem tissues were not perfectly preserved during the fixing, embedding and microtoming processes and some have contracted a little, with the epidermis (skin) becoming detached in places. This contraction explains the concavity of the sides of the square stem cross-section. Also in the largest cells some of the adjoining walls have become rippled. (a) Large-scale transverse micrograph of the entire stem. (b) Enlargement of one corner of (a) showing a vascular bundle. (c) Large-scale longitudinal micrograph. (d) Enlargement of part of (c). The longitudinal views show that many cells are similar in shape to short cylinders, and that often they are stacked upon one another in columns. This is why it is possible to see individual cells in the pith in transverse spin echo images. (e) Colour enlargement of the corner of the stem depicted in (b). The section has been treated with phloroglucinol which stains lignin, the major component of thick cell walls, red. Lignin is especially found in mature vessels of xylem. One can see a band of immature xylem (without the thickened walls) in the photograph which does not stain red, and which appears as a bright band in Fig. 5.4 (a).

5.5 Mechanisms Which Reduce T_2

The T_1 values encountered in this plant stem are commonly an order of magnitude larger than the T_2 values, and therefore we should try to pinpoint the possibilities leading to a greatly increased transverse relaxation rate where there is little effect on T_1.

Firstly the standard BPP theory of relaxation (discussed in Section 2.4) which covers the motionally-narrowed state shows a well-defined case for large T_1 and small T_2. The characteristic graph of T_1 and T_2 from this theory for the range of motional

regimes (in Fig 2.1) exhibits a T_1 minimum with quite different T_1/T_2 relationships on either side. While T_1 is equal to T_2 for $\tau_c^{-1} >> \omega_0$, as for small molecules in the liquid state, in the slower motion converse (or $\tau_c^{-1} << \omega_0$) T_2 becomes much smaller than T_1. This is so for protons in a highly viscous liquid phase where the rotational tumbling is considerably slowed, such as concentrated polymer solutions. Yet the protons in liquid water typically have correlation times of 10^{-12} s and fall into the former extreme-narrowed case, unless they are slowed or bound to other molecules in a hydration shell. Via exchange phenomena these slowed molecules may reduce the overall spin-spin relaxation time into the region where it is in fact much less than T_1.

Since the water molecules are confined within an essentially porous structure, collisions with the cell boundaries should be considered. According to the Brownstein-Tarr model *(76)*, the boundaries act as strong relaxation sinks due to the momentary lack of tumbling by molecules adhering to the surface, or perhaps to other mechanisms such as the presence of paramagnetic impurities at the surface. In this fashion relaxation rates, usually both spin-spin and spin-lattice, would tend to increase as the size of cells decreases and the surface-to-volume ratio consequently rises. Yet we have observed the longer T_2 values to be typically in the vicinity of the smaller diameter cells (phloem, inner xylem, cambial zone, collenchyma), suggesting another factor at work.

The dephasing caused by diffusion through local magnetic field gradients, as may occur near susceptibility boundaries, is an ideal candidate to explain our T_1/T_2 disparity because only apparent T_2 will be altered in the process. T_1 relaxation requires fluctuations at the Larmor frequency, but the modulation of the through-space interactions associated with passage through susceptibility variations is much slower than that frequency. Furthermore T_1 processes only involve fluctuations capable of inducing transitions between Zeeman levels, namely ones in the transverse (with respect to $\mathbf{B}_0$) field components. Therefore T_1 is unaffected by susceptibility modulation (of B_0 magnitude), while T_2 may be dramatically reduced. Just how the transverse relaxation is affected is once again determined by the exchange regime present, and in this case there is the possibility of fast exchange as well as the slow exchange evident in the experiments with glass rods. For the slow exchange case attenuation decreases as cell dimension rises, because of an inverse dependence of the attenuation factor $\exp(-\frac{2}{3}\sqrt{\Delta\omega_0^2\,\tau_c^{-1}t^3})$ on the correlation time τ_c, itself dependent on the correlation length ξ. However the opposite is true in the fast exchange case, where the factor $\exp(-2\,\Delta\omega_0^2\,\tau_c t)$ is dependent on τ_c. Therefore we might expect to see predominantly the latter which fits with our observation of long T_2 in the small-celled tissues.

The other influence which must not be overlooked is diffusion in the presence of the read gradient itself, conspicuous in the high-resolution water images of our glass rods. If this plays an important part in the stem images then the smaller cells could suffer less attenuation due to a lower effective diffusion coefficient D, and the observed relation between cell size and apparent T_2 could result. But are the pixels small enough and the acquisition times NT long enough for this to be noticeable here? Once again we may apply the analysis as before, using our read gradient attenuation factor $\exp[-\gamma^2 G_x^2(\frac{1}{2}NT)^2 D(T_E-\frac{2}{3}NT)]$ which allows for the adjustable echo time necessary for T_2 mapping, and calculating G_x from $\frac{2\pi\Delta f}{\gamma N\Delta x}$ (T is $1/\Delta f$). The bandwidth is 40 kHz, the FOV 6 mm and the number of pixels N is 256, giving an A_f of 0.77 for our minimum T_E of 10 ms. The attenuation is even more dramatic for the longer T_E values, with 0.62 for 15 ms, 0.49 for 20 ms and 0.39 for 25 ms! Clearly read gradient attenuation must be considered seriously in the determination of T_2 for the stem tissues.

5.6 Isolation of Susceptibility and Read Gradient Effects by B_0 Dependence and CPMG Sequences

Thus in order to interpret the previous images these issues must be cleared up by new tests carried out on a new stem. We need to distinguish between the alternatives which fit the observations of T_2 which is much less than T_1 but is also longest for the smallest cells. The choice seems to be between simple attenuation due to the read gradient, and attenuation arising from susceptibility boundary-caused gradients, or of course a component of both. Should the latter alternative prove significant, then we should probe the exchange regimes in the different tissues further.

A tool for the elimination of imaging gradient attenuation has already been utilised in Section 4.6, and this was the CPMG sequence with the refocusing pulse train before the read precursor gradient. Thus we have the ability to lengthen echo times while suffering only extra 'true' T_2 relaxation and that from residual gradients in field offsets present at all times (while inside the magnet). In fact for T_2 mapping even one 180° pulse before the read precursor will allow us to insert our echo-prolonging delays before the read precursor and consequently 'out of harm's way'. This and the conventional form of T_2 map can be compared and any changes attributed to the read gradient.

Regardless of fast or slow exchange, a positive marker for susceptibility at work is a relationship between the effects and the size of B_0, the polarising field. The field offsets and therefore gradient offsets are directly proportional to B_0. For this reason the same

stem should be imaged at more than one B_0 value, and all this done within the same time limit of plant freshness, so some resolution will be sacrificed to reduce the overall experiment times. However, information gained by this will subsequently be applied to the better-resolved original images anyway for more detailed discussion of tissue contrast.

5.7 T_2-mapping Using CPMG

As proposed another *Stachys sylvatica* seedling similar to the last was prepared in the same way, and T_2 maps were obtained using the two methods mentioned above in Section 5.6. The 128^2 maps are shown in Fig 5.6 (in colour for easy comparison of magnitudes) along with a 256^2 gradient echo image to give a good reference with clear structure. Normal tap water encircles the stem in the NMR tube, and serves as a useful standard. This plant is older and the cambial zone has developed further, giving a darker ring of differentiated xylem inside the bright one. The external water allows us to visualise the epidermal ('skin') layer and outer cortex for the first time, as a region of little or no intensity. The conventional T_2 map (Fig 5.6b) is very similar to that of the previous stem in Fig 5.4c, with the ring of smaller cells appearing brighter than the cortex or pith. In this map the free water has a T_2 of around 35 ms, which is very low and adds to our suspicions about this form of T_2 mapping.

On the other hand the new T_2 map from our CPMG sequence (Fig 5.6c) is startlingly different from the conventional map, exhibiting a near reverse contrast pattern. The large pith cells filling the central space of the stem have the longest T_2. Furthermore, the T_2 of the free tap water is ten times longer in this map than in the last, meaning that the read gradient effect must surely have been overwhelming the intrinsic T_2/cell size relationships. The conventional T_2 maps could indeed be likened to maps of diffusion in the read direction, increasing with compartment diameter. However this complicating factor does not yet rule out susceptibility effects as a significant player too.

The very same stem was also imaged in a 1.4 T electromagnet, as shown in Fig 5.7. Unfortunately it was necessary to reduce the number of pixels even further to 64^2 to achieve a satisfactory signal-to-noise ratio, and the images may only be used for approximate magnitudes rather than detailed structure analysis. The relaxation factor for our susceptibility-linked attenuation (Section 5.5) contained a $\overline{\Delta\omega_0^2}$ term in the exponential, in both exchange conditions, and since we have reduced B_0 by a factor of

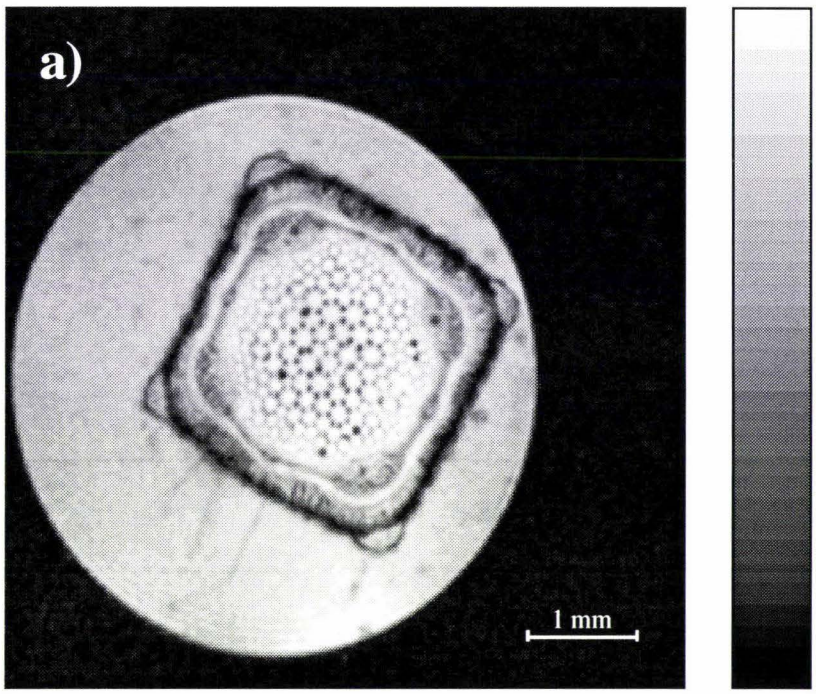

Figure 5.6. (a) Gradient echo image of a third *Stachys sylvatica* stem (in a tube of water) with long T_R (2 s) and minimum T_E (8 ms). (b) Map of T_2 relaxation time calculated from a series of spin echo images at a range of echo times (from 9 ms to 60 ms). (c) Map of T_2 relaxation time calculated from a series of CPMG images at a range of echo times (from 11 ms to 89 ms). Here the echo times are lengthened by placing an extra delay before the read precursor (unlike the usual spin echo case) which contains a single CPMG pulse. The 'CPMG-obtained' T_2 is significantly longer than obtained by the standard spin echo and is also in a near reverse pattern of contrast (e.g. the central pith T_2 is greater than that of the vascular tissue in the former, and less than it in the latter). The spin echo case also has an anomalously low T_2 value for the free water. The number of pixels N in (a) is 256 and the pixel size Δx is 23 μm, whereas there are 128 pixels in (b) and (c) giving a larger pixel size of 47 μm. Parameters: B_0 = 7 T, bandwidth = 40 kHz, n_{acq} = 2, slice thickness = 1 mm, T_R = 2 s.

five in the electromagnet this term should decrease by 25, leading to a massive reduction in apparent transverse relaxation up to the limit of 'true' T_2. This is not seen in either the CPMG-obtained or conventional T_2 maps, with T_2 seeming remarkably similar in the former and roughly doubled in the latter case (not surprisingly given the increase in pixel size) for this field strength.

In reality we would not expect to observe the full effect of lower field strength on T_2 because the plant stem is necessarily transversely oriented to the polarising field in the electromagnet, and so the field offsets ΔB_0 caused by the cells should be moderately stronger in this case. In Chapter 3 it was shown that offsets were significant for the transverse orientation (of the glass rods) only and not for the longitudinal orientation. However our cells cannot generally be considered to be long cylinders like the glass rods, but more like short cylinders (or even spheres in some cases) as is evident in the

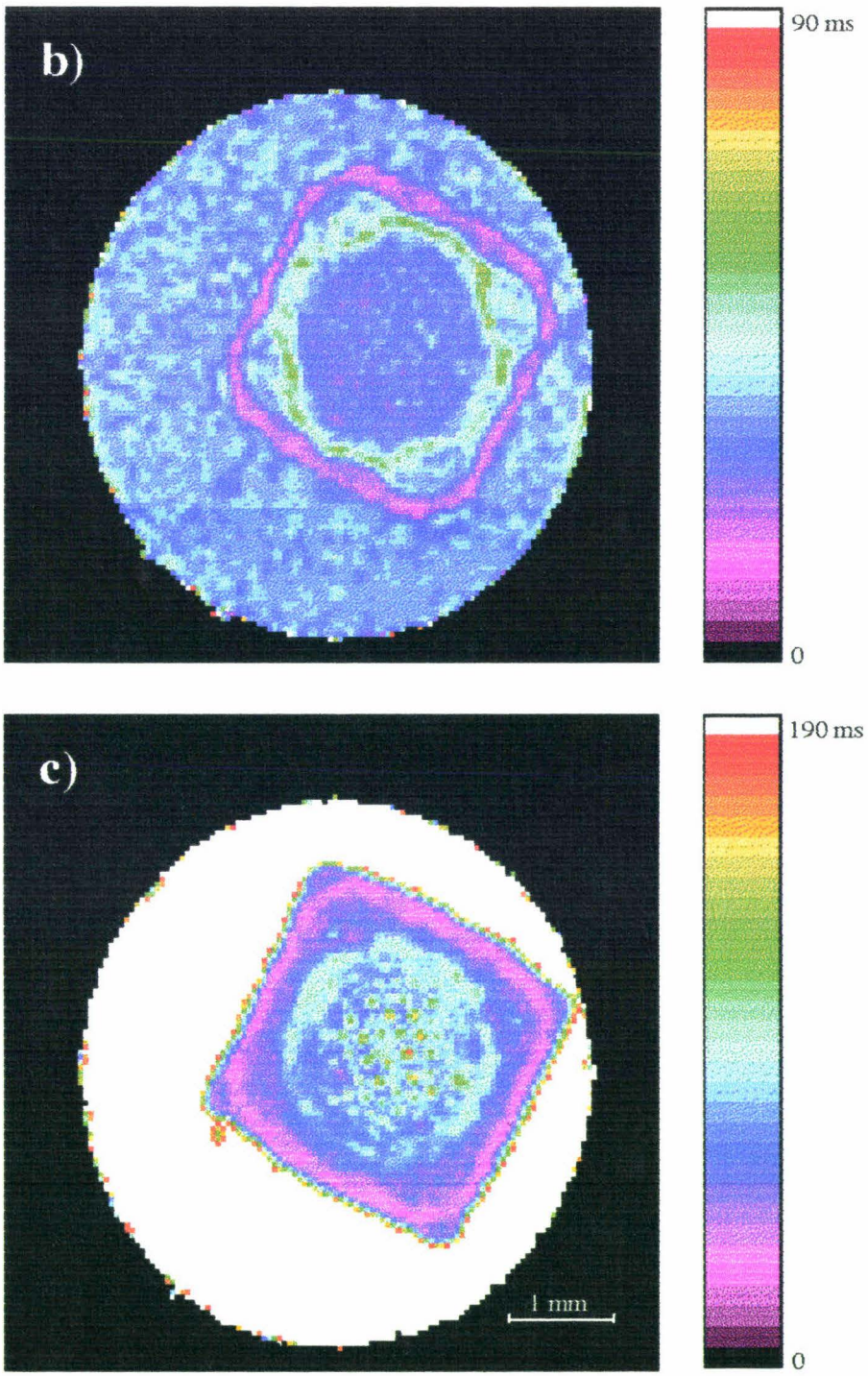

Figure 5.6 (b), (c)

longitudinal micrographs shown earlier (Fig 5.5). Hence we would expect the end walls themselves to generate field offsets when in longitudinal orientation, and this was the basis for assuming susceptibility modulation of signal in our longitudinally-arranged plant (in the superconducting magnet) in the first place. Returning to the measured T_2 at different B_0 values, it would be fairly remarkable for the orientational effects to perfectly cancel the supposedly-massive field strength effects without overshoot, and the

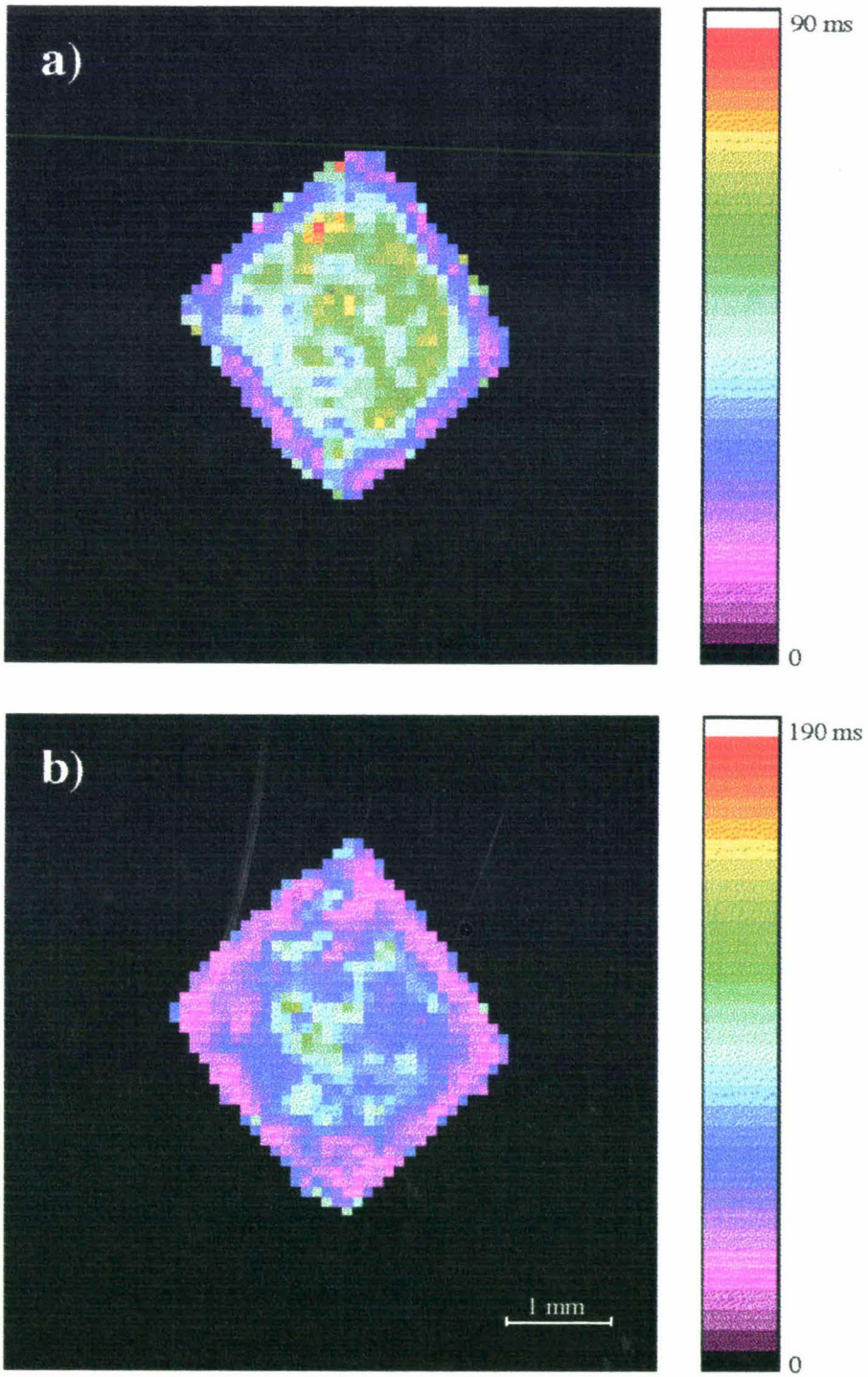

Figure 5.7. T_2 maps acquired in the same way as Fig. 5.6 (b) and (c) on the same stem, except that the experiments were performed in a 1.4 T electromagnet. The pixel size was increased again to provide adequate signal-to-noise ratio in the lower polarising field. (a) Map of T_2 relaxation time calculated from a series of spin echo images at a range of echo times (from 10 ms to 40 ms). (b) Map of T_2 relaxation time calculated from a series of CPMG (n=1) images at a range of echo times (from 11 ms to 89 ms). Surprisingly the CPMG-obtained T_2 map is very similar in magnitude to the same map at 7 T, exhibiting very little B_0 dependence. The standard T_2 map is roughly doubled in magnitude over that at 7 T, probably because of reduced diffusive attenuation due to the larger pixels. Parameters: B_0 = 1.4 T, bandwidth = 20 kHz, Δx = 94 μm, N = 64, n_{acq} = 8, slice thickness = 2 mm, T_R = 1 s.

conclusion is surely that susceptibility effects are not the dominant influence on relaxation in our plant tissue as was first considered. Before we move on to contemplate the remaining alternatives capable of explaining the observed T_2 contrast, it is interesting and reassuring to note that the T_1 values at 7 T, displayed in Fig 5.8, are approximately twice those at 1.4 T. We would predict this according to the BPP theory mentioned in Section 2.4 and illustrated graphically in Fig 2.1 because T_1 will become longer as the Larmor frequency ω_0 is increased. The T_1 of the free tap water is about 2 s in the map, which is a reasonable value.

5.8 Brownstein-Tarr Model Revisited

Thus the problem remains to resolve the general reduction of T_2 on T_1 (roughly by ten) still evident in the stems, even in CPMG-obtained maps. Since we have solved the puzzle of apparently longer T_2 in smaller cells by eliminating read gradient diffusion effects, we may once again consider the Brownstein-Tarr model of relaxation at boundaries and surfaces in more detail. The model (Section 5.5) specifically addresses the question of short relaxation times in biological cellular systems, and does not rely upon the presence of altered water states due to interactions with membranes or macromolecules. It does however depend on the geometry and size of the cells. As before the cell boundary is seen as an 'active surface' with a relaxation sink strength density of μ.

If we consider a two site system consisting of firstly, a boundary layer of thickness δx possessing reduced T_2 (T_{2B}) near the wall of a spherical cell and secondly, a much larger reservoir of 'bulk' water in the centre with effectively infinite T_2 (T_{2A}), then μ may be equated with $\delta x/T_{2B}$ by examination of the governing equations. M is the average value of μ over the surface. For clarity we are only considering the case where the relaxation rate is increased in the boundary layer due to momentary 'adherence' to the surface, without needing to include dephasing from gradients (although this can still be incorporated into the general theory as another sink factor if desired). It could be likened somewhat to the reduced apparent diffusion constant seen in Section 4.4 which resulted in white crescents on the inside of the glass tube wall, except that a read gradient was used for visualisation there. In this model the average dwell times of molecules in the layer and in the bulk are termed τ_B and τ_A respectively, and there will be exchange between the two populations. It should be noted that there is no frequency difference between the two populations and thus the system is strictly in fast exchange at all times by the familiar criterion $\overline{\Delta\omega_0^2}\,\tau^2 << 1$ (as $(\overline{\Delta\omega_0^2})^{1/2}$ is zero). τ is the exchange time (and

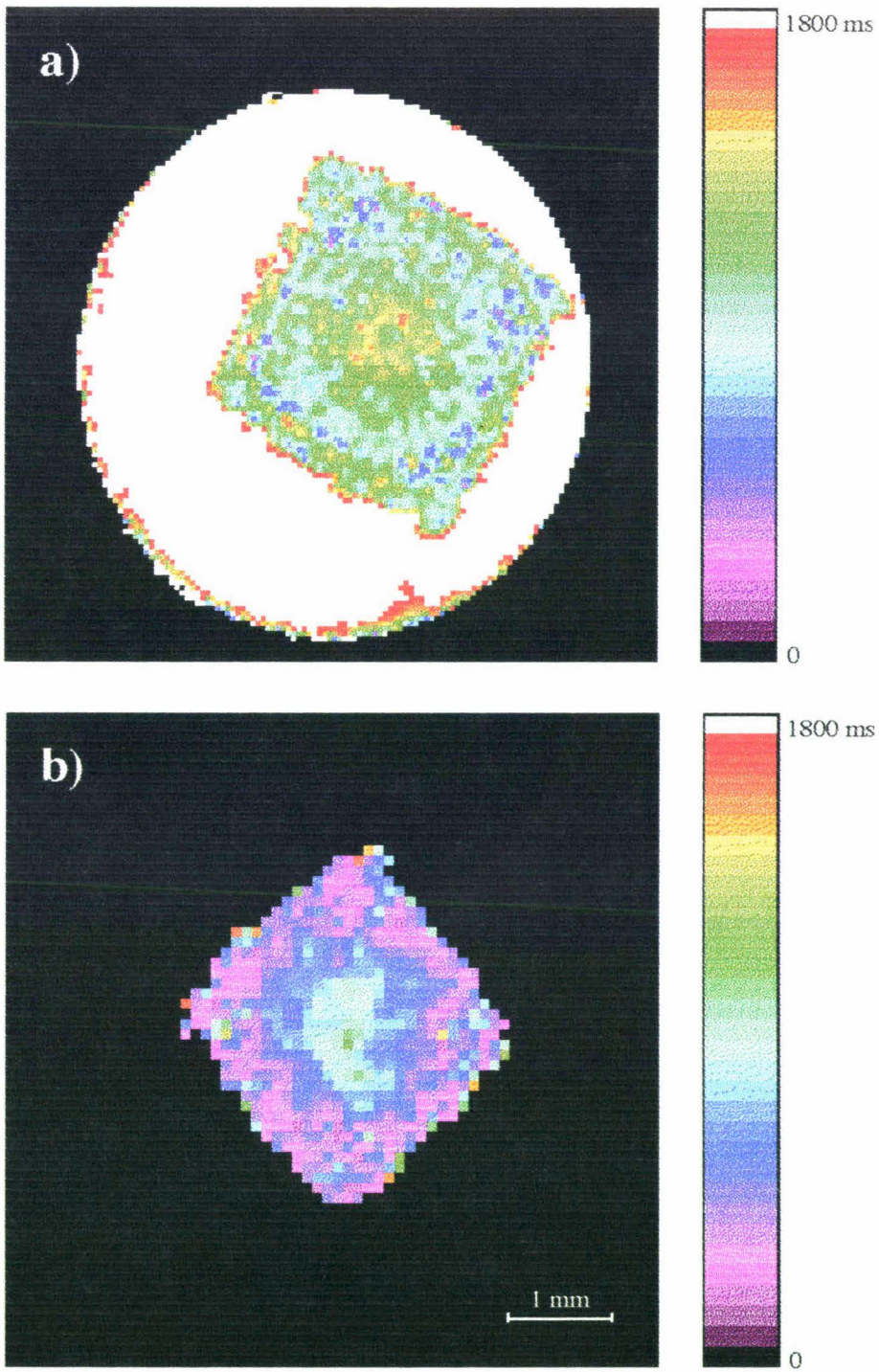

Figure 5.8. T_1 relaxation time maps calculated from a series of spin echo images at a range of repetition times T_R (from 150 ms to 4 s), acquired at (a) 7 T and (b) 1.4 T. T_1 values in (a) are approximately twice those in (b), as might be expected in Bloembergen, Purcell and Pound theory where T_1 increases with Larmor frequency. Parameters: for B_0 = 7 T, bandwidth = 40 kHz, Δx = 47 µm, N = 128, n_{acq} = 2, slice thickness = 1 mm, T_E = 9 ms; for B_0 = 1.4 T, bandwidth = 20 kHz, Δx = 94 µm, N = 64, n_{acq} = 8, slice thickness = 2 mm, T_E = 10 ms.

$1/\tau$ the exchange rate) between the 'sites'. There are however other characteristic regimes of behaviour known as 'fast' and 'slow' diffusion, represented by $\tau_B << T_{2B}$ and $\tau_B >> T_{2B}$ respectively. To relate this to our geometry the criteria may be restated as

$Ma/D << 1$ and $Ma/D >> 1$, where a is the radius of the sphere or cell, and so the regime is governed by the diffusion of water from the cell centre to the cell surface.

For slow diffusion the total attenuation of the echo at time t (over the bulk T_2 relaxation) is $\exp(-\frac{Dt}{a^2} - \frac{1}{5}\gamma^2\delta^2 G_x^2 a^2)$ and for fast diffusion it is $\exp(-\frac{Mt}{a} - \frac{1}{5}\gamma^2\delta^2 G_x^2 a^2)$, translating to additional T_2 components of a^2/D and a/M respectively *(119)*. G_x is our read gradient and δ is the length of the read gradient pulse $NT/2$. Of course one must add relaxation rates rather than times (which are added reciprocal form), and if a^2/D or a/M is on the order of or less than the bulk T_2 then it will contribute to the contrast. Both alternatives lead to more severe effects (short T_2) as the cell diameter decreases, as we found in the T_2 map from CPMG. Incidentally the second part of the expression, $\frac{1}{5}\gamma^2\delta^2 G_x^2 a^2$, is many orders smaller than the T_2-like parts.

5.9 CPMG Pulse-Spacing Dependence

Can we learn anything by varying the pulse spacing in a long-echo CPMG experiment as we did in Section 4.6 (distinguishing between fast and slow exchange attenuation)? Pulse-spacing dependence is not so intuitive for the Brownstein-Tarr model, and it is necessary to refer to a general analysis of pulse spacing by Carver and Richards *(71)*. This analysis is done for chemical exchange, but can be meaningfully extended to our own two site system. When the fast and slow diffusion cases are considered for very small CPMG interpulse delay τ_{cp} ($\tau_{cp} << T_B$) the Carver-Richards theory results in the same additional T_2 components of a/M and a^2/D as before. For long τ_{cp} the outcome is also the same, unless two criteria are fulfilled: $\Delta\omega^2 T_{2B}\tau_B > 1$ and $T_{2B} >> 1/\Delta\omega >> \tau_B$. $\Delta\omega$ is the frequency difference between populations. Checking these inequalities, $1/\Delta\omega >> \tau_B$ is the hallmark of fast exchange and $T_{2B} >> \tau_B$ means fast diffusion, both possible, but the constraint that $\Delta\omega$ be zero rules out both of the original criteria anyway. The conclusion is that for the simple model we have studied with no $\Delta\omega$ between the two sites there can be no pulse-spacing dependence. This seems sensible since 180° pulses can only refocus dephasing, which requires a frequency difference.

In order to further validate the Brownstein-Tarr influence in the plant stem the relevant CPMG experiments were performed again as in Chapter 4, i.e. with control of the interpulse delay by holding the echo time constant and varying the number of 180° pulses. Fig 5.9 shows the resulting images at both field strengths, including the previous T_2 maps (from CPMG) for comparison. After the T_2 maps are shown: b) a short echo

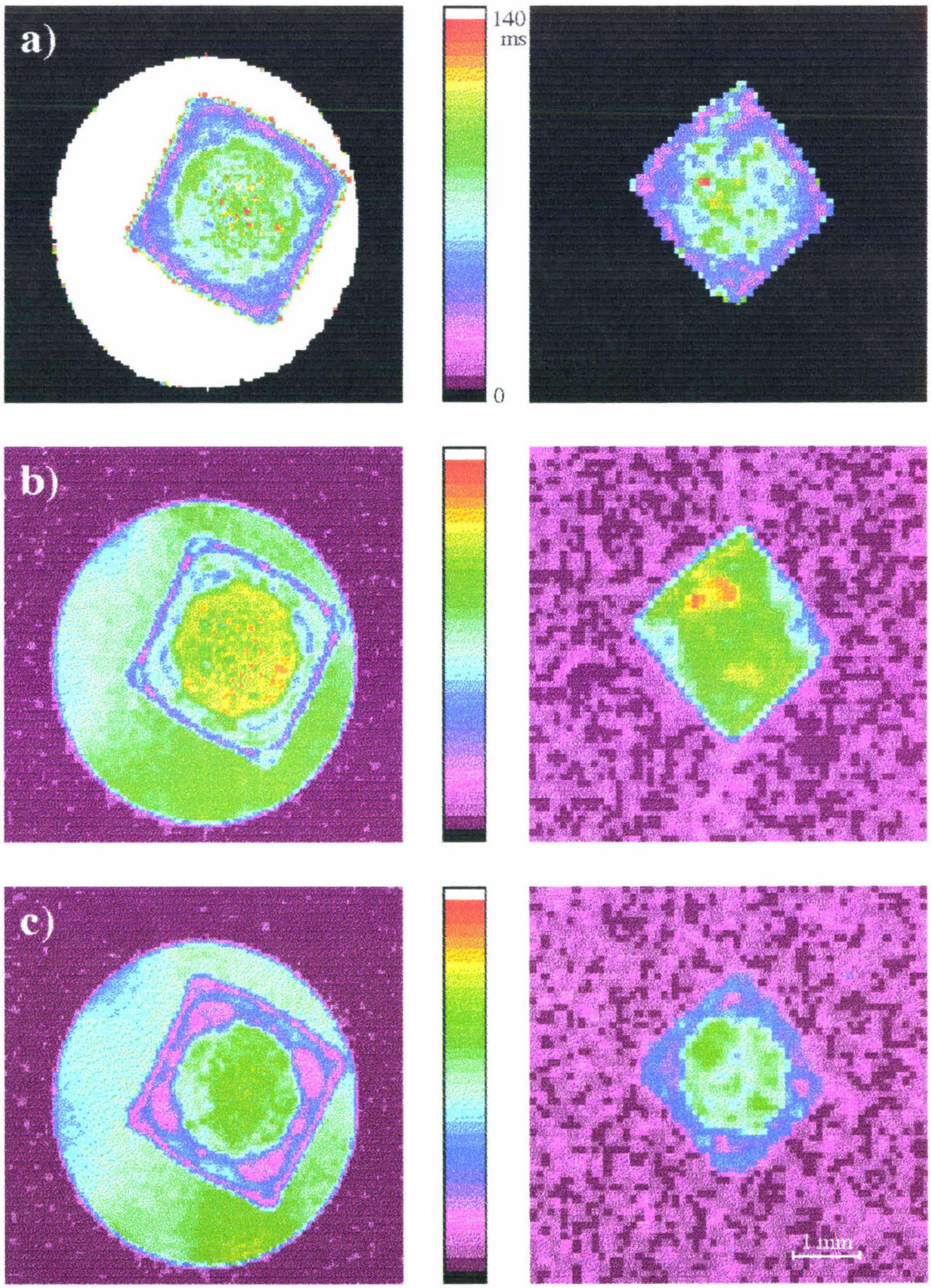

Figure 5.9. A series of CPMG images probing the dependence of image intensity on pulse spacing. Each treatment was carried out at both 7 T (the images on the right) and 1.4 T (the images on the left). The CPMG-obtainedT_2 maps from Fig.s 4.6 and 4.7 are shown again in (a) for comparison. (b) Images acquired with a short T_E (11 ms) and one CPMG loop only (n = 1), giving a short half interpulse delay τ_{cp} of 1.25 ms. (c) Images acquired with a long T_E (89 ms) and 32 CPMG loops (n = 32), giving the same τ_{cp} of 1.25 ms. (d) Images acquired with a long T_E (89 ms) and one CPMG loop only (n = 1), giving a very long τ_{cp} of 40 ms. Comparison of (b) with (c) shows T_2 relaxation without pulse-spacing

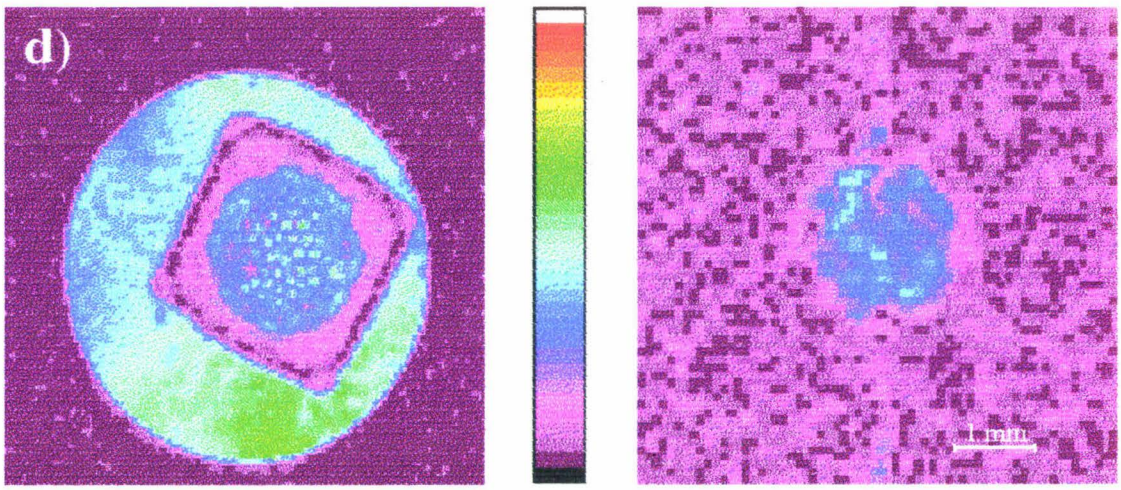

Figure 5.9 (d)

Figure 5.9. (cont.) effects, and (c) with (d) displays any pulse spacing dependence as τ_{cp} is controlled by holding the echo time constant and varying the number of 180_y pulses. Parameters: for B_0 = 7 T, bandwidth = 40 kHz, Δx = 47 μm, N = 128, n_{acq} = 2, slice thickness = 1 mm, T_R = 2 s; for B_0 = 1.4 T, bandwidth = 20 kHz, Δx = 94 μm, N = 64, n_{acq} = 8, slice thickness = 2 mm, T_R = 1 s.

and short τ_{cp} image, c) a long echo time image with the same short τ_{cp} (32 CPMG loops) and d) a long echo image with a very long τ_{cp} (1 loop). Comparing b) with c) gives an idea of the relative T_2 times of the different tissues without any pulse-spacing alterations, and one can see that the ring of vascular tissue has been attenuated more than the larger cortex and pith cells, which suits our model well. Comparing c) with d) shows an unexpected pulse-spacing dependence in the parenchymatous pith and cortex but not elsewhere. The values for the two field strengths follow each other closely, reinforcing the earlier conclusion that the interactions present are not affected by the magnitude of B_0.

Thus we have a yet another puzzle, namely the attenuation effect in the parenchyma cells of the stem which depends on τ_{cp} and therefore must involve a phenomenon connected with a frequency difference $\Delta\omega$, but which is not at all dependent on B_0. This rules out chemical shift exchange and any susceptibility-related phenomena, and since the extra delays are added before any imaging gradients the read gradient will have the same effect regardless of τ_{cp}. Furthermore the application of Carver-Richards theory to the Brownstein-Tarr model suggests that the τ_{cp} dependence should not change with cell radius. The parenchyma relaxation curves appear to be single exponentials and so don't appear to yield multiple T_2 components which might together cause anomalous behaviour. The difference image in Fig 5.10 taken between the two long echo time images (32 loops and 1 loop) confirms that it is the parenchyma tissue affected, and implies some special attribute of these cells. We know that parenchyma cells are metabolically-active, unlike either phloem or xylem transport tissues (which lack nuclei

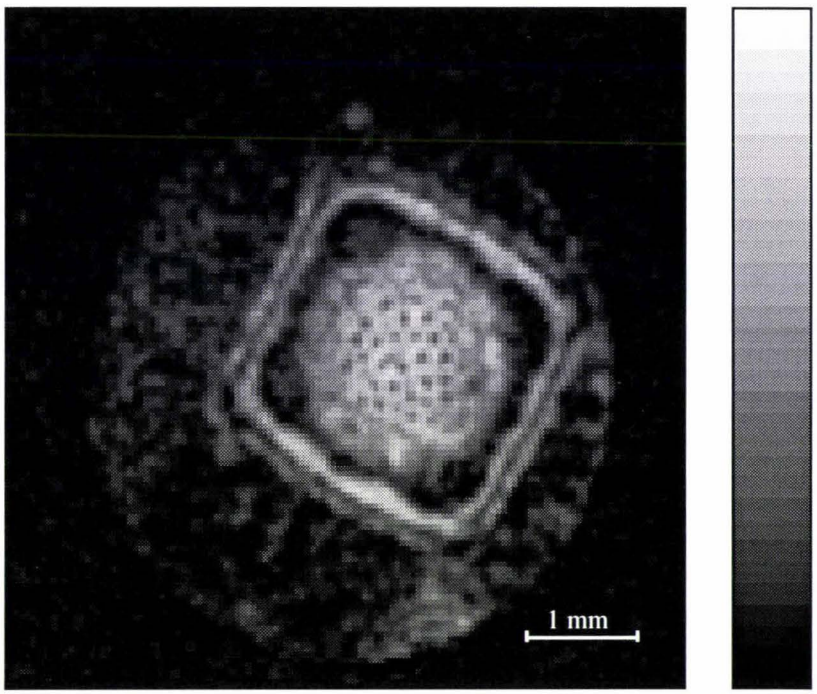

Figure 5.10. A difference image between Fig.s 5.9 (c) and (d), the two long echo CPMG images. Only the 7 T images were used as the resolution of the 1.4 T images was not sufficient to differentiate between tissues with certainty. The two contributing images had τ_{cp} values of 1.25 ms and 40 ms. Therefore the regions which are bright, the pith and cortex (parenchymatous) tissues, have a marked pulse spacing dependence. Parameters: B_0 = 7 T, bandwidth = 40 kHz, Δx = 47 μm, N = 128.

and even cell membranes respectively), or collenchyma cells (essentially terminally-differentiated and incapable of normal metabolism). Therefore they contain the complete range of metabolic apparatus such as organelles like mitochondria and chloroplasts, as well as rough and smooth endoplasmic reticulum and golgi bodies (membrane networks associated with enzyme production and function) and also macromolecules other than proteins like polysaccharides, nucleic acids and microtubules. It would seem that the only alternative left to us for explanation of the mysterious effect is very short-range magnetic dipole interactions (single spin to spin) of the water protons with protons of slow-moving or stationary macromolecules. These would involve a $\Delta\omega$ which is not B_0 dependent. Protons in hydration water are candidates for these interactions, and Hazlewood *et al (11)* proposed this scheme in their analysis of T_2 in rat skeletal muscle.

5.10 Interpretation of Intensity in the Original Stem Images

Armed with a bewildering tangle of T_2 relaxation mechanisms, each with their own criteria and behaviour, we may return to the thorough dissection of the original series of images and maps and attempt to explain the apparent contrasts in more detail. The tissues may be divided, with exceptions, into the two broad groups distinguished by cell diameter. The parenchyma cells in the pith and cortex may be considered 'large', while

all other types are small in comparison. These two groups are most easily seen in the conventional T_2 map in Fig 5.4c. Using the model justified above (Section 5.7) of additional transverse relaxation due to simple attenuation in the read gradient, the 'small' cells are expected to have relatively long apparent T_2, and they do appear relatively bright in the map. For example, the tiniest cells as seen in the light micrograph (Fig 5.5) are in the phloem and the fibres near the xylem, and these certainly exhibit the longest T_2, while the ring of the cambial zone also looks bright. The xylem consists of a range of cell sizes, and has an intermediate T_2, as does the collenchyma in the outer ribs. The pith and cortex have uniformly short T_2.

Having identified the areas of long T_2 and observed them to be quite bright in the image which has solely a weak T_2 contrast, it is disconcerting to see these same areas as relatively dark parts of the calculated 'amplitude' map (Fig 5.4d). The amplitude map is extrapolated from T_2 data back to zero echo time, and should ideally mirror the water content in the tissues. The darker regions (the phloem, fibres, xylem and collenchyma) point us to some kind of underlying intensity variation which is capable of modulating the contrast further. Two possibilities explain this phenomenon, namely either that the extrapolation in these places is not appropriate or accurate, or that there is simply less water present in these tissues. The narrow bright band between the phloem and the xylem, most visible in the short echo image and identified in the micrograph as the cambium and early secondary xylem, gives a clue to a possible explanation.

This band does not at first seem different to the adjacent xylem, until it is stained with phloroglucinol, in which case the walls do not stain red. This indicates that lignin thickening has not yet been deposited on the incipient xylem, and since lignin is the predominant material in characteristically-thick xylem walls, it could be inferred that the cell walls are in fact much thinner than in the mature xylem. In tissues containing cells with very thick walls a larger proportion of the water would presumably be found in the hydration shell of the wall macromolecules, and this proportion would have a much shorter T_2 *(11)* due to the diminished rotational motion as discussed earlier (Section 2.4). In this situation, the relaxation curve would be a bi-exponential, but the fast-relaxing component could well be invisible if the minimum echo time is comparatively long. Fig 5.11 shows a typical relaxation curve for just this case (not real data), and illustrates how an inaccurate extrapolated amplitude can result. The T_2 of hydration water has been estimated in the literature to be less than 5 ms, which is indeed less than our minimum echo time of about 10 ms.

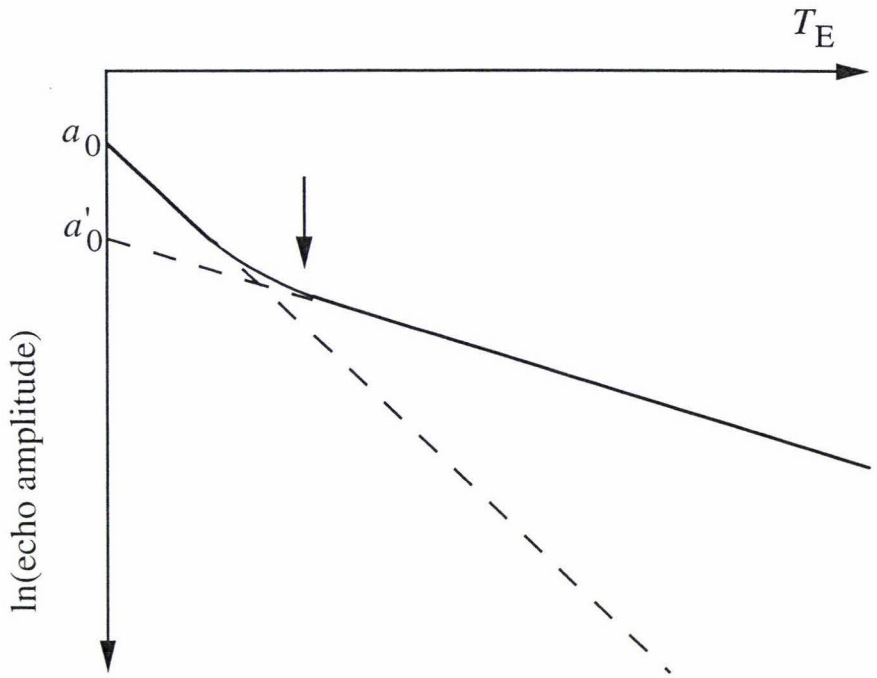

Figure 5.11. A typical bi-exponential T_2 relaxation curve which might result from a sample with two populations of spins with differing dynamics. For this situation the minimum echo time T_E attainable is crucial to the recognition of the faster-relaxing component. If the minimum echo time used is at or above that shown by the arrow, not only will only one T_2 component be measured but the extrapolated proton density will be underestimated as well, as a'_0 instead of a_0.

The tissues known for thick walls are xylem and collenchyma, neither of which appear bright in the 'amplitude' map, but the other tissues which also appear dark are not specially known for this trait. However they all consist of fairly small cells, and thus will still have a large surface-to-volume ratio, again elevating the proportion of water which is located in the walls rather than in the cytoplasm. In this way we observe the curiosity of long T_2 in small-celled areas and yet low intensity in the very same places for apparent water proton density. The increased volume proportion of wall and accompanying small cell size renders one fraction of the water invisible by short T_2 while protecting the remaining fraction from read gradient attenuation and bestowing on it an extended apparent T_2.

The T_1 (Fig 5.4b) map follows the trends of the CPMG-T_2 map distribution (Fig 5.6c), longest in the cortex and pith, and shorter in the vascular and other tissues. The most probable contender to reduce T_1 is the same Brownstein-Tarr effects, and the least is an increase in the concentration of paramagnetic impurities in these areas, namely ions. The phloem is known for high nutrient and ion concentration as its primary purpose is for transport of these. However xylem normally contains a very dilute solution. T_1 has also been known to reflect actual water density, and this may support the hypothesis

of variation of water concentration in the amplitude map rather than the two T_2 component explanation.

5.11 The Original Gradient Echo Images

Lastly we may once more contemplate the images obtained using a gradient echo pulse scheme rather than a spin echo. The promised susceptibility effects did not emerge from our prolonged analysis, and the stark evidence is a consistent absence of any dependence on polarising field strength. Inspecting the T_2^* map together with the conventional T_2 map (Fig 5.4f and 5.4c) we see that the majority of the tissues are in close agreement for the two, supporting this finding, because in the absence of any extra inhomogeneous broadening T_2^* should equal T_2. Both sequences are prone to the same read gradient attenuation. Yet there is a visible difference between the image types in Fig 5.4a and 5.4e (even if not so much in the relaxation maps) and so perhaps the highlighted cell junctions are not reflected in the average transverse relaxation parameters, at least without greater resolution in the maps. Even a slight movement or wilting of the stem during the hours of the T_2^* mapping process would smear the fine structure into a mean value, and indeed the centre of the T_2^* map has a speckled appearance.

The last and most perplexing paradox in our search for susceptibility effects in *Stachys sylvatica* is the difference between T_2 and T_2^* of the complete ring of vascular tissue. This must surely arise from magnetisation dephasing in the presence of field offsets, yet in none of our experiments so far have we seen any evidence of the required B_0 dependence. Oddly the susceptibility effects seem to act as though they are entirely static, i.e. as though there is no movement of molecules through the offsets, so that they are entirely refocused by a spin echo, and we see no indication except in the gradient echo image. It is true that the cells in question are very small, and thus the water molecules are not free to move 'far' easily. If the extra transverse relaxation component is given by $\exp(-2\,\Delta\omega_0^2\,t^2)$, and an echo time t of approximately 10 ms is used, then we need a minimum $(\,\Delta\omega_0^2\,)^{1/2}$ of 40 rad s^{-1} to see significant attenuation (by 10%) for the static case. With motion, presuming the xylem cells etc. are small enough (as most appear to be in the optical micrograph) to be in fast exchange (Section 3.4), the expression is $\exp(-2\,\Delta\omega_0^2\,\tau_c t)$, and for echo time $2t$ of 10 ms an rms frequency spread of 40 rad s^{-1} has little effect. Hence there is a region of frequencies which might show an outcome in the static condition only. Presumably the frequency range falls within this region for the vascular tissue in our stem.

5.12 Translational Motion of Water Within the Stem - Diffusion and Flow

Finally we can make use of our ability to measure translational motion in order to observe the transport of water within our stem while it is actually in the apparatus. As well as indicating the continued health of the plant in experimental conditions, we will be able to see which tissues are actually participating in the transport (probably due to transpiration). Not all of the xylem may be involved, depending upon factors such as the maturation stage of the vessels (considering the point at which the immature xylem becomes functional and that where the old xylem drops from use) and possible uneven requirements of water from different leaves (which are arranged in pairs, alternating by 90^{o} in orientation, for each internode). The direction of flow in the phloem for a typical stem should be in the opposite direction, although it will be much more delicate than in the xylem, especially since photosynthetic activity will be low inside the long dark bore of the superconducting magnet.

The dynamic imaging pulse sequence, explained in Section 2.9, was used to obtain maps of velocity and diffusion in the vertical or z-direction, shown in Fig 5.12 above the standard spin echo image. The velocity map has a relatively large component of noise which does not quite mask the actual regions of flow in the xylem (near the corners of the square cross-section). As predicted there is no major flow component apparent in the 'negative' direction (blue) to indicate significant phloem transport. Pixel to pixel comparison with the standard image shows that the flow does not occur uniformly throughout each xylem bundle (seen as darker areas near the corners), but is fragmented and localised to the outer, older regions. It is never seen in the dark spots which were presumed to be fibres. Also the four xylem bundles do not appear to support the same total amount of water transport, but with the level of noise this is not certain.

The diffusion map (Fig 5.12c) shows remarkably little detail considering the contrast we saw earlier due to diffusion in the presence of the read gradient. This is however not so strange when one considers that the earlier contrast arose from diffusion in the read direction whereas the map represents instead the z-component of diffusion (normal to the slice plane). Because the lengths of the cells down the stem are not necessarily related to their cross-sectional diameters, the diffusion map does not mirror our conventional T_2 map which was dominated by read gradient attenuation. It would be possible to measure the x-component of diffusion too if desired, but in an experiment separate from one measuring velocity in the z-direction. Our map appears to conclude

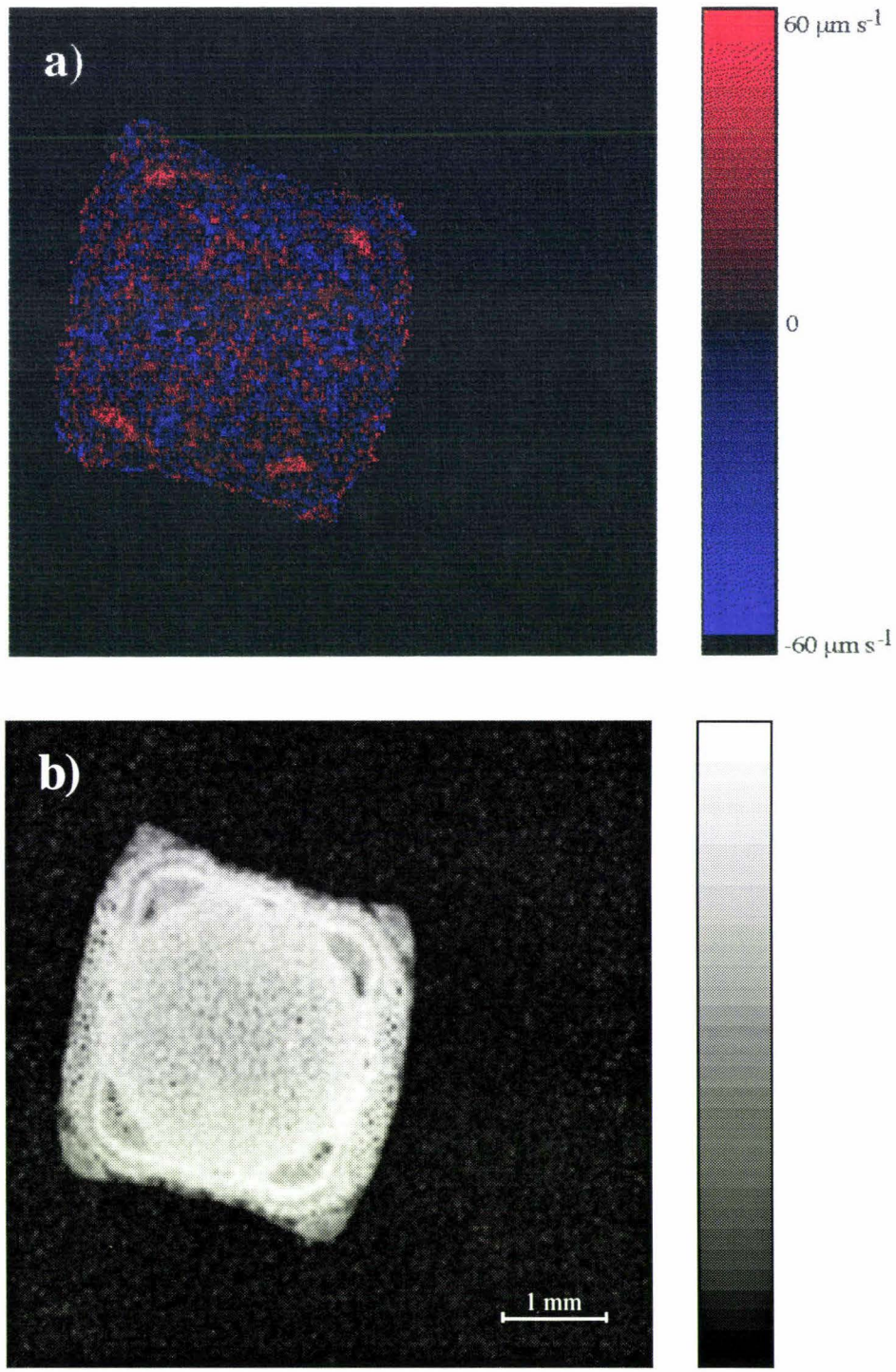

Figure 5.12. (a) Velocity map acquired with the dynamic imaging sequence in Fig. 2.7, along with a standard spin echo image in (b) to distinguish the tissues. A net positive (upward) flow can be seen in the older xylem tissue (in red), although it is fragmented and not far above the noise level. As expected any flow in the phloem, which would be blue and outside the xylem, is too delicate to be measured here. (c) Self-diffusion coefficient map acquired with the same sequence as in (a). The parameters for (b) are listed already in Fig. 5.4. Parameters: B_0 = 7 T, bandwidth = 40 kHz, Δx = 23 μm, N = 256, n_{acq} = 2, slice thickness = 500 μm, δ = 0.7 ms, Δ = 203 ms, T_E = 212 ms, T_R = 1 s.

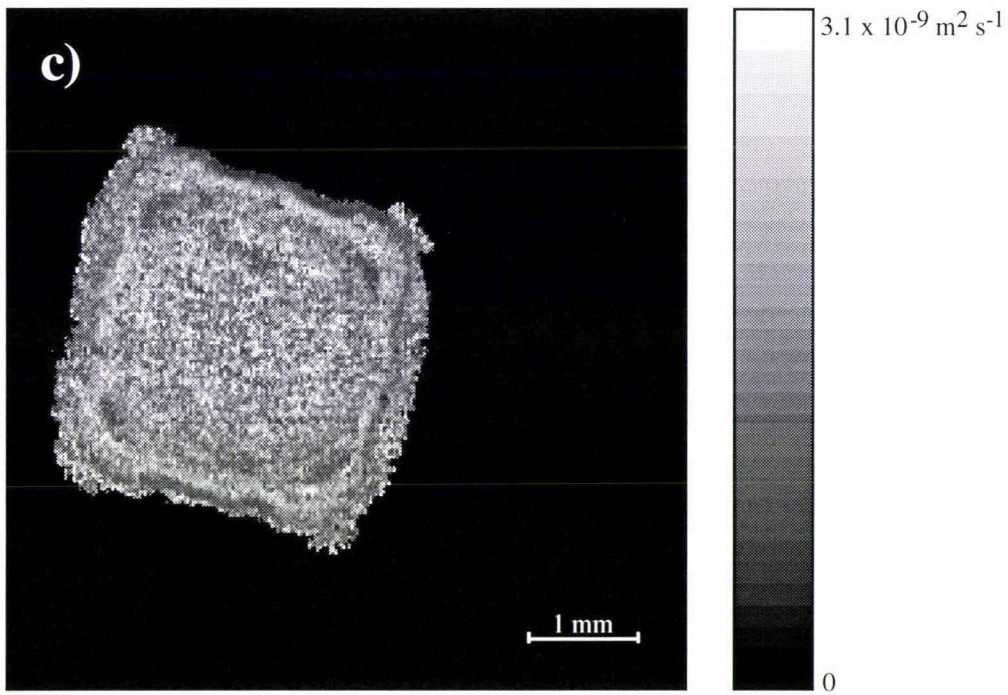

Figure 5.12 (c)

that the cells are sufficiently long so that diffusion is not hampered significantly and the diffusion coefficient is fairly uniform, although it is slightly less in the xylem, especially in the dark spots.

The maximum flow seen in our stem is on the order of 30 $\mu m\ s^{-1}$, close to the limit of our sensitivity as one can see in the map where it is barely visible above the noise level. It seemed worthwhile to repeat the experiment (for flow only) on another plant in order to see if the transpiration could be increased with more care of the plant. The results, shown in Fig 5.13, were significantly better with a maximum velocity of around 70 $\mu m\ s^{-1}$. Visualisation of the flow was improved by setting the colour scale such that any large positive values appear red while smaller values arising from noise, positive or negative, will fall below the positive cut-off and appear blue. This improvement in the second plant may mean that the original was not as healthy as it might have been, due to factors such as the fraction of roots excised while fitting them into the apparatus, or due to less leaf area for transpiration. On the other hand it may simply be the inevitable variation amongst any collection of biological samples.

It was not the main intention of this thesis to pursue the accurate measurement of flow, although some more possibilities and applications will be discussed in Chapter 6. The main drive of this research, which is the analysis of the meaning of individual

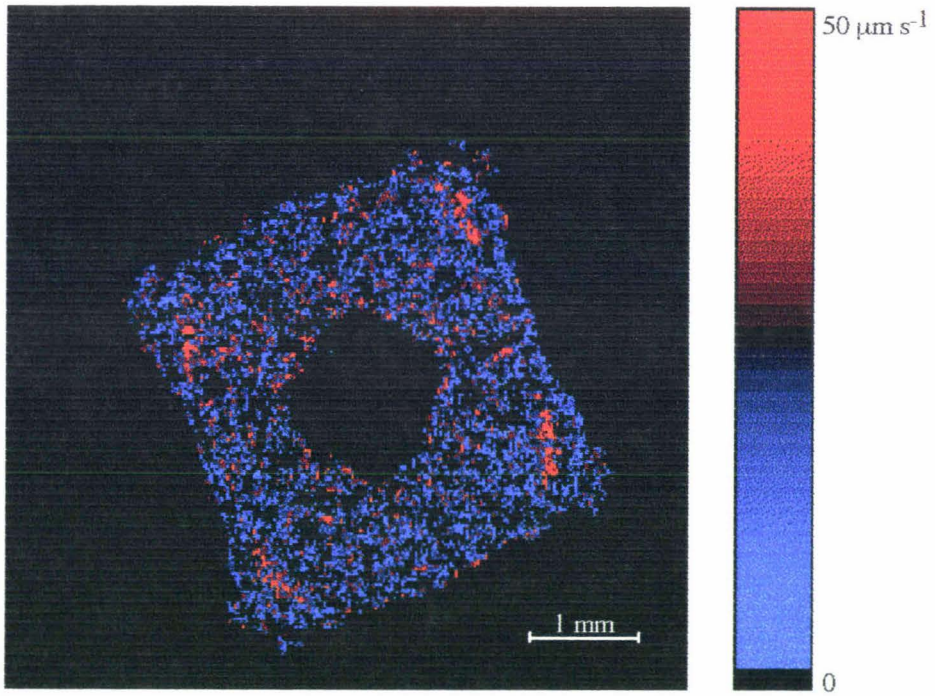

Figure 5.13. Velocity map of another stem acquired with the dynamic imaging sequence. The hole in the centre of the stem is common in more mature plants. Parameters: B_0 = 7 T, bandwidth = 40 kHz, Δx = 23 μm, N = 256, n_{acq} = 2, slice thickness = 500 μm, δ = 0.7 ms, Δ = 203 ms, T_E = 212 ms, T_R = 1 s.

contrast effects, has on the whole been reasonably encouraging about the general value of combining a complete range of pre- and mid-imaging treatments in order to further microscopic understanding.

Chapter 6
Concluding Remarks

It is not surprising that the results in this thesis offer as many new questions as they do solutions about high-resolution NMR imaging. We have been reminded how much more stimulating it can be to receive experimental outcomes opposite to those predicted. In particular the investigation of plant microscopy in Chapter 5 evolved along channels quite unforeseen at the beginning, because the expected dominant effects were ruled out one-by-one in the series of diagnostic pulse sequences. Although susceptibility inhomogeneity was originally evident in gradient echo images, further experiments at different B_0 strengths revealed that it did not contribute significantly to the spin echo image contrast. A strong alternative linking cell size to relaxation rate was provided by the Brownstein-Tarr model of relaxation at boundaries and surfaces, but again a pulse-spacing dependence (in the cortex and pith) could not be explained by this theory (although it is possible in the other tissues). This left a mystery as to which phenomenon, involving exchange with a non-B_0-dependent Larmor frequency difference, might be responsible for the variation in T_2 between the stem tissues. We could only suggest short-range dipole interactions between water protons and protons of more slowly-moving molecules, but it is still very uncertain and difficult to examine this further without detailed information of cell contents.

Part of the trouble with biological samples is the difficulty in constructing relevant model systems. The glass cylinders used in Chapter 4 allowed easy simulation via analytical solutions but they did not mirror stem cells very well. Where the cells are arranged in columns, as in the xylem, the end walls introduce further susceptibility boundaries, meaning that short cylinders would be a more appropriate model. Unfortunately the simulation for short cylinders is not so simple and requires numerical methods to evaluate the solution. Nevertheless it was rewarding to clarify the relationships between susceptibility inhomogeneity and diffusion in determining image distortion and attenuation with glass tubes and rods. This experience did prove fruitful later in the recognition of a flaw in our measurement procedure of T_2 which concerned read gradient attenuation. The problem was resolved by the use of a train of CPMG refocusing 180° pulses, and careful thought led to the development of an appropriate pulse sequence allowing the freedom to manipulate echo times without incurring such misleading attenuation.

However the work with *Stachys sylvatica* evoked a healthy respect for the intricacies of high-resolution imaging, and highlighted the limits imposed upon the

advance of its understanding without close contact with suitable anatomical experts and also severe invasive microscopy like transmission electron microscopy to expose all cell constituents. In addition it is really necessary to carry out proper multicomponent T_2 analysis (e.g. to explain anomalies in extrapolated 'amplitude' or proton density maps), although multiple exponential functions are notoriously difficult to dissect (especially if the number of components is not known) and even more so in conjunction with imaging. At the least, rapid scan techniques would be necessary to inspect the early parts of the relaxation curves.

Nonetheless some new avenues of research which use the simple regimes in these chapters are apparent, including the use of our diagnostic methods on other plants or organisms which could yield very dissimilar results. It is probable that some other botanical specimens would show more pronounced susceptibility effects, while yet other samples such as animal tissue should show very little due to a lack of air between cells. Possibilities concerning plant stem imaging are on the whole dependent on the construction of improved apparatus to keep the plant in good condition, for example providing ample space and aeration for the roots, as well as careful control of environmental parameters like light and temperature. Transpiration itself could be monitored by dynamic imaging in individual plants with different treatments, while also knowing the area of leaves and the rate of disappearance of water from around the roots. The removal of certain leaves (or other injuries) could lead to interesting observations as the transpirational load on nearby vascular tissues is reduced. Photosynthesis may also be examined if sufficient flow is generated in the phloem, and related to light intensity.

Turning to diffusion, a map taken in the read direction should support the observation of unequal read gradient attenuation in cells of varying diameter. The indirect detection of cell (or any compartmentation) sizes is not straightforward and requires further progress, mainly because there may be more correspondence of relaxation behaviour with tissue type than with simple size. Although our relaxation results showed the stem cells as belonging to two broad size groups, the pith cells for example all seemed to share similar characteristics even though the sizes in the centre were more than those near the cambium. Also there may be much more still to be gleaned from T_1 data regarding water density, concentration of ions and so on, and it would be good to clarify its exact role in the Brownstein-Tarr theory.

One final consequence of this study has been to emphasise the strengths and pitfalls of the various pulse sequences available. The main conclusion here has been the usefulness of CPMG trains to counter unwanted interference from diffusive attenuation.

However the train's point of insertion into the sequence is crucial to the outcome, as was discovered in the case of the standard spin echo. Small turn angle errors in the 180° rf pulses (arising probably from rf inhomogeneity across the sample space) accumulated to degrade the image when they were placed after the precursor read gradient, but this was solved by instead placing them just after the initial 90° excitation pulse and before the read precursor. Some methods for the alleviation or even elimination of susceptibility-related distortion and attenuation have also been indicated. The use of large bandwidths (limited by availability) and care with sample orientation are fairly obvious, but a more subtle solution is the double phase encoding sequence which removes the need for a read gradient altogether. Explored further in a recent paper *(108)*, double phase encoding would seem to overcome all or most of the susceptibility effects (again depending on the gradient size available), but it comes at the price of much longer experiment times (by a factor of the number of pixels N) and large three-dimensional data sets. However the longer experiments may be put into perspective when one considers that the use of an equivalent large bandwidth would require the same overall time to attain the same signal-to-noise ratio from signal averaging. It should also be noted that the data from double phase encoding has the bonus of chemical shift information. A logical extension to the work shown here would have to be imaging of the *Stachys sylvatica* stem using double phase encoding, in order to confirm the apparently unimportant role of susceptibility inhomogeneity. Regardless of the approach (spin warp or double phase encoding) it would be helpful to have access to gradient strengths greater than those attainable in the Bruker microimaging probehead, and a recently developed quadrupolar gradient set *(C. J. Rofe, unpublished)* could be suitable for work of this kind with some thought as to how the plant stems might be mounted inside.

References

1. Lauterbur, P. C. (1973). *Nature* **242**, 190.

2. Mansfield, P. and Grannell, P. K. (1973). *J. Phys. C* **6**, L422.

3. Mansfield, P. and Morris, P. G. (1982). *NMR Imaging in Biomedicine*, Academic Press, New York.

4. Moonen, C. T. W., van Zijl, P. C. M., Frank, J. A., LeBihan, D. and Becker, E. D. (1990). *Science* **250**, 53.

5. Mansfield, P. and Pykett, I. L. (1978). *J. Magn. Reson.* **29**, 355.

6. Attard, J. J., Carpenter, T. A., de Crespigny, A., Duce, S. L., Hall, L. D., Hawkes, R. C., Herrod, N. J. and Hodgson, R. J. (1990). *Phil. Trans. R. Soc. Lond. A* **333**, 477.

7. King, G. F., York, M. J., Chapman, B. E. and Kuchel, P. W. (1983). *Biochem. Biophys. Res. Commun.* **110**, 305.

8. Endre, Z. H., Kuchel, P. W. and Chapman, B. E. (1984). *Biochim. Biophys. Acta* **803**, 137.

9. Packer, K. J. (1973). *J. Magn. Reson.* **9**, 438.

10. Burnell, E. E., Clark, M. E., Chapman, N. R. and Hinke, J. A. M. (1981). *Biophys. J.* **33**, 1.

11. Hazlewood, C. F., Chang, D. C., Nichols, B. L. and Woessner, D. E. (1974). *Biophys. J.* **14**, 583.

12. Foster, K. R., Resing, H. A. and Garroway, A. N. (1976). *Science* **194**, 324.

13. Johnson, G. A., Thompson, M. B., Gewalt, S. L. and Hayes, C. E. (1986). *J. Magn. Reson.* **68**, 129.

14. Kurland, R. J. and Ngo, F. Q. H. (1986). *Magn. Reson. Med.* **3**, 425.

15. Cameron, I. L., Ord, V. A. and Fullerton, G. D. (1984). *Magn. Reson. Imaging* **2**, 97.

16. Chen, P., McCarthy, M. J. and Kauten, R. (1989). *Trans. Am. Soc. Agr. Eng.* **32**(5), 1747.

17. Duce, S. L., Carpenter, T. A., Hall, L., Hawkes, R., Herrod, N. and Tyszka, M. (1990). *Chem. and Ind.* **19**, 94.

18. Wang, S. Y., Wang, P. C. and Faust, M. (1988). *Scientia Horticulturae* **35**, 227.

19. Goodman, B. A., Williamson, B. and Chudek, J. A. (1992). *Protoplasma* **166**, 107.

20. Pope, J. M. (1992) in *Magnetic Resonance Microscopy: Methods and Application in Materials Science, Agriculture and Biomedicine*, eds Blümich, B. and Kuhn, W., VCH, Weinheim.

21. Pech, J. C., Latche, A., Andrieu, M. H. and Pradere, J. (1990). *Proc. Int. Hort. Cong.* 635.

22. Williamson, B., Goodman, B. A. and Chudek, J. A. (1992). *New Phytol.* **120**, 21.

23. Wang, C. Y. and Wang, P. C. (1989). *HortScience* **24**(1), 106.

24. Song, H. P. and Litchfield, J. B. (1990). *Cereal Chemistry* **67**(6), 580.

25. Wang, C. Y. (1991). *HortScience* **26**(6), 697.

26. Duce, S. L., Carpenter, T. A. and Hall, L. D. (1992). *J. Food Eng.* **16**, 165.

27. Ruan, R. and Litchfield, J. B. (1992). *Cereal Chem.* **69**(1), 13.

28. Duce, S. L., Carpenter, T. A., Hall, L. D. and Hills, B. P. (1992). *Magn. Reson. Imaging* **10**(2), 289.

29. Lauterbur, P. C. (1974). *Pure Appl. Chem.* **40**, 149.

30. Schaafsma, T. J., Van As, H., Palstra, W. D., Snaar, J. E. M. and de Jager, P. A. (1992). *Magn. Reson. Imaging* **10**, 827.

31. Ishida, N., Kobayashi, T., Koizumi, M. and Kano, H. (1989). *Agric. Biol. Chem.* **53**(9), 2363.

32. German, J. B. and McCarthy, M. J. (1989). *J. Agric. Food Chem.* **37**, 1321.

33. Duce, S. L., Carpenter, T. A. and Hall, L. D. (1990). *Lebensm. Wiss. u. Technol.* **23**, 545.

34. Johnson, G. A., Brown, J. and Kramer, P. J. (1987). *Proc. Natl. Acad. Sci. USA* **84**, 2752.

35. Veres, J. S., Johnson, G. A. and Kramer, P. J. (1991). *Am. J. Bot.* **78**(1), 80.

36. Kuntz, I. D., Brassfield, T. S., Law, G. D. and Purcell, G. V. (1969). *Science* **163**, 1329.

37. Walters, J. A. and Hope, A. B. (1971). *Prog. Biophys. Molec. Biol.* **23**, 3.

38. Mathur-DeVre, R. (1979). *Prog. Biophys. Molec. Biol.* **35**, 103.

39. Glasel, J. A. and Lee, K. H. (1974). *J. Am. Chem. Soc.* **96**, 970.

40. Brown, J. M., Thomas, J. F., Cofer, G. P. and Johnson, G. A. (1988). *Botanical Gazzette* **149**(3), 253.

41. Connelly, A., Lohman, J. A. B., Loughman, B. C., Quiquampoix, H. and Ratcliffe, R. G. (1987). *J. Exp. Bot.* **38**(195), 1713.

42. Eccles, C. D. and Callaghan, P. T. (1986). *J. Magn. Reson.* **68**, 393.

43. Kamei, H. and Katayama, Y. (1986). *Proc. 8th Ann. Conf. IEEE Engin. in Med. and Biol. Soc.*, Fort Worth, p1159.

44. Xia, Y., Sarafis, V., Campbell, E. O. and Callaghan, P. T. (1993). *Protoplasma* **173**, 170.

45. Cofer, G. P., Brown, J. M. and Johnson, G. A. (1989). *J. Magn. Reson.* **83**, 608.

46. Wutscher, H. K. (1991). *HortScience* **26**(6), 745.

47. Kuhn, W. (1990). *Angewandte Chemie* **29**, 1.

48. Morris, P. G., Darceuil, H. E., Jasinski, A, Jha, A. K., McIntyre, D. J. O. and Northcote, D. H. (1990). *Phil. Trans. R. Soc. Lond. A* **333**, 487.

49. Stout, D. G., Steponkus, P. L. and Cotts, R. M. (1978). *Plant Physiology* **62**, 636.

50. Faust, M. (1991). *HortScience* **26**(7), 818.

51. Faust, M., Liu, D., Millard, M. M. and Stutte, G. W. (1991). *HortScience* **26**(7), 887.

52. Rogers, H. H. and Bottomley, P. A. (1987). *Agronomy J.* **79**, 957.

53. Bottomley, P. A., Rogers, H. H. and Foster, T. H. (1986). *Proc. Natl. Acad. Sci. USA* **83**, 87.

54. Bacic, G. and Ratkovic, S. (1984). *Biophys. J.* **45**, 767.

55. Warmund, M., Brown, J., Schaffer, K. and Barritt, B. (1990). *Proc. Int. Hort. Cong.* **xxx**, 186.

56. Hall, L. D., Rajanayagam, V., Stewart, W. A. and Steiner, P. R. (1986). *Can. J. For. Res.* **16**(2), 423.

57. Harrison, L. G., Luck, S. D., Munasinghe, B. D. J. P. and Hall, L. D. (1988). *J. Cell Sci.* **91**, 379.

58. Brown, J. M., Johnson, G. A. and Kramer, P. J. (1986). *Plant Physiology* **82**, 1158.

59. Eccles, C. D., Callaghan, P. T. and Jenner, C. F. (1988). *Biophys. J.* **53**, 77.

60. Jenner, C. F., Xia, Y., Eccles, C. D. and Callaghan, P. T. (1988). *Nature* **336**, 399.

61. Hills, B. P. and Duce, S. L. (1990). *Magn. Reson. Imaging* **8**, 321.

62. Abetsedarskaya, L. A., Miftakhutdinova, F. G. and Fedotov, V. D. (1969). *Biofizika* **14**, 873.

63. Snaar, J. E. M. and Van As, H. (1992). *Biophys. J.* **63**, 1654.

64. Anderson, P. W. and Weiss, P. R. (1953). *Rev. Mod. Phys.* **25**(1), 269.

65. Daszkiewicz, O. K., Hennel, J. W., Lubas, B. and Szczepkowski, T. W. (1963). *Nature* **200**, 1006.

66. Koenig, S. H. and Schillinger, W. E. (1969). *J. Biol. Chem.* **244**(12), 3283.

67. Packer, K. J. (1977). *Phil. Trans. R. Soc. Lond. B* **278**, 59.

68. Belton, P. S. and Hills, B. P. (1987). *Molec. Phys.* **61**, 999.

69. Belton, P. S., Hills, B. P. and Raimaud, E. R. (1988). *Molec. Phys.* **63**, 825.

70. Hills, B. P., Wright, K. M. and Belton, P. S. (1989). *Molec. Phys.* **67**, 1309.

71. Carver, J. P. and Richards, R. E. (1972). *J. Magn. Reson.* **6**, 89.

72. Eisenstadt, M. (1980). *J. Magn. Reson.* **39**, 275.

73. Menon, R. S., MacKay, A. L., Flibotte, S. and Hailey, J. R. T. (1989). *J. Magn. Reson.* **82**, 205.

74. Araujo, C. D., MacKay, A. L., Whittall, K. P. and Hailey, J. R. T. (1993). *J. Magn. Reson.* **B101**, 248.

75. Belton, P. S. and Ratcliffe, R. G. (1985). *Prog. NMR Spectro.* **17**, 241.

76. Brownstein, K. R. and Tarr, C. E. (1979). *Phys. Rev. A* **19**(6), 2446.

77. Whittall, K. P. (1991). *J. Magn. Reson.* **94**, 486.

78. Sharp, J. C., Bowtell, R. W. and Mansfield, P. (1993). *MRM* **29**, 407.

79. Aguayo, J. B., Blackband, S. J., Schoeniger, J., Mattingly, M. A. and Hintermann, M. (1986). *Nature* **322**, 190.

80. Frahm, J., Merboldt, K. D. and Hänicke, W. (1993). *Magn. Reson. Med.* **29**(1), 139.

81. Kwong, K. K., Belliveau, J. W., Chesler, D. A., et al (1992). *Proc. Natl. Acad. Sci. USA* **89**, 5675.

82. Ogawa, S., Tank, D. W., Menon, R., Ellermann, J. M., Kim, S., Merkle, H. and Ugurbil, K. (1992). *Proc. Natl. Acad. Sci. USA* **89**, 5951.

83. Frahm, J., Bruhn, H., Merboldt, K. D. and Hänicke, W. (1992). *Magn. Reson. Imaging* **12**, 501.

84. Merboldt, K. D., Bruhn, H., Hänicke, W., Michaelis, T. and Frahm, J. (1992). *Magn. Reson. Med.* **25**, 187.

85. Bandettini, P. A., Wong, E. C., Hinks, R. S., Tikofsky, R. S. and Hyde, J. H. (1992). *Magn. Reson. Med.* **25**, 390.

86. Ogawa, S., Lee, T. M., Nayak, A. S. and Glynn, P. (1990). *Magn. Reson. Med.* **14**, 68.

87. Ogawa, S., Lee, T. M. (1990). *Magn. Reson. Med.* **16**, 9.

88. Turner, R., LeBihan, D., Moonen, C. T. W., DesPres, D. and Frank, J. (1991). *Magn. Reson. Med.* **22**, 159.

89. Guilfoyle, D. N. and Mansfield, P. (1992). *J. Magn. Reson.* **97**, 342.

90. Thulborn, K. R., Waterton, Matthews, P. M. and Radda, G. K. (1982). *Biochim. Biophys. Acta* **714**, 265.

91. Van As, H. (1992). *Acta Horticulturae* **304**, 103.

92. Purcell, E. M., Torrey, H. C. and Pound, R.V. (1946). *Phys. Review* **69**, 37.

93. Bloch, F., Hansen, W. W. and Packard, M. (1946). *Phys. Review* **70**, 474.

94. Callaghan, P. T. (1991). *Principles of Nuclear Magnetic Resonance Microscopy*, Oxford University Press, Oxford.

95. Eccles, C. D. (1987). *Microscopic NMR Imaging*, PhD thesis, Massey University.

96. Xia, Y. (1988). *Static and Dynamic Imaging Using Magnetic Field Gradients*, MSc thesis, Massey University.

97. Xia, Y. (1992). *Dynamic NMR Microscopy*, PhD thesis, Massey University.

98. Bloch, F. (1946). *Phys. Review* **70**, 460.

99. Bloembergen, N., Purcell, E. M. and Pound, R. V. (1948). *Phys. Review* **73**, 679.

100. Eccles, C. D. and Callaghan, P. T. (1987). *JEOL News* **23A**(1), 10.

101. Carr, H. Y. and Purcell, E. M. (1954). *Phys. Review* **94**, 630.

102. Meiboom, S. and Gill, D. (1959). *Rev. Sci. Instr.* **29**, 688.

103. Stejskal, E. O. and Tanner, J. E. (1965). *J. Chem. Phys.* **42**, 288.

104. Callaghan, P. T., Eccles, C. D. and Xia, Y. (1988). *J. Phys. E* **21**, 820.

105. Kärger, J. and Heink, W. (1983). *J. Magn. Reson.* **51**, 1.

106. Callaghan, P. T. and Eccles, C. D. (1987). *J. Magn. Reson.* **71**, 426.

107. Callaghan, P. T. (1990). *J. Magn. Reson.* **87**, 304.

108. Callaghan, P. T., Forde, L. C. and Rofe, C. J. (1994). *J. Magn. Reson.* **B103**, in press.

109. Edmonds, D. T. and Wormald M. R. (1988). *J. Magn. Reson.* **77**, 23.

110. Ludecke, K. M., Roschmann, P. and Tischler, R. (1985). *Magn. Reson. Imaging* **3**, 329.

111. Posse, S., Aue, W. P. (1990). *J. Magn. Reson.* **88**, 473.

112. Torrey, H. C. (1956). *Phys. Rev.* **104**, 563.

113. Callaghan, P. T. and Eccles, C. D. (1988). *J. Magn. Reson.* **78**, 1.

114. Abragam, A. (1961). *Principles of Nuclear Magnetism*, Clarendon Press, Oxford.

115. Hyslop, W. B. and Lauterbur, P. C. (1991). *J. Magn. Reson.* **94**, 501.

116. Pütz, B., Barsky, D. and Schulten, K. (1992). *J. Magn. Reson.* **97**, 27.

117. Barsky, D., Pütz, B., Schulten, K., Schoeniger, J., Hsu, E. W. and Blackband, S. (1992). *Chem. Phys. Letters* **200**, 88.

118. Callaghan, P. T., Coy, A., Forde, L. C. and Rofe, C. J. (1993). *J. Magn. Reson.* **A101**, 347.

119. Lipsicas, M., Banavar, J. R. and Willemsen, J. (1986). *Appl. Phys. Lett.* **48**, 1544.